VILNIUS UNIVERSITY

CENTER FOR PHYSICAL SCIENCES AND TECHNOLOGY

OLGA OPUCHOVIČ

SUSTAINABLE CHEMISTRY APPROACH TO OBTAIN
MULTIFUNCTIONAL IRON-BASED INORGANIC COMPOUNDS

Doctoral Dissertation

Physical Sciences, Chemistry (03 P)

Vilnius, 2018

The dissertation was carried out from 2014 to 2018 at Vilnius University.

Scientific supervisor: Prof. Habil. Dr. Aivaras Kareiva (Vilnius University, Physical Sciences, Chemistry – 03P)

VILNIAUS UNIVERSITETAS

FIZINIŲ IR TECHNOLOGIJOS MOKSLŲ CENTRAS

OLGA OPUCHOVIČ

DARNIOSIOS CHEMIJOS VYSTYMAS DAUGIAFUNKCINIAMS
GELEŽIES NEORGANINIAMS JUNGINIAMS GAUTI

Daktaro disertacija
Fiziniai mokslai, Chemija (03 P)

Vilnius, 2018

Disertacija rengta 2014–2018 metais Vilniaus universitete.

Mokslinis vadovas: prof. habil. dr. Aivaras Kareiva (Vilniaus universitetas, Fiziniai mokslai, Chemija – 03P)

Contents

List of Abbreviations

CIE	Commission Internationale de l'Eclairage
DLS	Dynamic Light Scattering
DSC	Differential Scanning Calorimetry
DTG	Derivative Thermogravimetric
DyIG	Dysprosium Iron Garnet, $Dy_3Fe_5O_{12}$
EG	Ethylene glycol
ErIG	Erbium Iron Garnet, $Er_3Fe_5O_{12}$
EuIG	Europium Iron Garnet, $Eu_3Fe_5O_{12}$
FTIR	Fourier Transform Infrared
GC	Gas Chromatography
GdIG	Gadolinium Iron Garnet, $Gd_3Fe_5O_{12}$
GL	Glycerol
HoIG	Holmium Iron Garnet, $Ho_3Fe_5O_{12}$
LuIG	Lutetium Iron Garnet, $Lu_3Fe_5O_{12}$
MRI	Magnetic Resonance Imaging
MS	Mass Spectrometry
NIR	Near Infrared
PLD	Pulsed Laser Deposition
SEM	Scanning Electron Microscopy
SmIG	Samarium Iron Garnet, $Sm_3Fe_5O_{12}$
TbIG	Terbium Iron Garnet, $Tb_3Fe_5O_{12}$
TG	Thermogravimetry
TmIG	Thulium Iron Garnet, $Tm_3Fe_5O_{12}$
UV/VIS	Ultraviolet/Visible
XRD	X-ray Diffraction
YAIG	Yttrium Aluminium Iron Garnet, $Y_3Al_{5-x}Fe_xO_{12}$
YbIG	Ytterbium Iron Garnet, $Yb_3Fe_5O_{12}$
YIG	Yttrium Iron Garnet, $Y_3Fe_5O_{12}$

Chapter 1. Introduction

Iron-based inorganic compounds have an important role in our modern life. Different iron oxide pigments have been used from ancient times [1, 2] and have not been replaced nowadays. For example, hematite is the oldest iron oxide mineral and very important pigment. Moreover, iron-based compounds are relevant not only in art, but they are also used in optics, magneto-optics and microwave devices [3]. The colour of the inorganic pigment depends on the chromophores, which are usually metal ions with a different oxidation state [4, 5]. Despite the fact that there are a lot of coloured materials of inorganic origin, pigment producers are still interested in pigments that present intense tonalities and which are in agreement with the technological and environmental requirements and are new non-toxic ceramic pigments with high temperature stability [6]. Due to the low toxicity, chemical stability, durability, and low costs iron oxide pigments offer a potential in modern pigment industry and technologies [7, 8]. A huge variety of inorganic pigments for mass colouration of glasses, glazes and ceramic bodies contain toxic elements such as cadmium, cobalt, lead and chromium [9-12]. In order to avoid these elements, lanthanide oxide pigments are used. Among these pigments there are $LaFeO_3$ [13], $LnFeO_3$ (where Ln = Gd, La, Yb, Tm, Lu) [14], $HoFeO_3$ [15], $ErFeO_3$, $NdFeO_3$ and $SmFeO_3$ [16]. Interestingly, to the best of our knowledge, lanthanide iron garnets have not been used as ceramic pigments. The characteristics of pigments, such as colour, particle size distribution, resistance to acids, alkalis or abrasives are highly sensitive not only to the changes in dopant composition or host stoichiometry, but also to the processing conditions, which are very much responsible for the crystallinity, crystal shape, crystal size, crystal size distribution and phase purity of the resulting powders [17-19]. In order to prepare these iron-containing mixed oxides, the solid-state reaction between the component metal oxides or carbonates, is still utilized because of its lower manufacturing cost and more simple preparation process [10, 11, 14, 16, 20]. However, this method, in general, requires the annealing temperature to be higher than 1000 °C to eliminate the unreacted starting compounds and to obtain

the final product of a single phase. In order to overcome these inevitable disadvantages, soft chemical methods including sol-gel [7, 13, 21] can be used.

In recent years magnetic materials have been in the focus of interest, with much attention paid to their potential usage in modern technologies. Main components of audiovisual equipment, telephones, kitchen machines and the microwave ovens are magnetic. Magnetic disks are used to read and write information, hard disk drives are used for storage of information [22].

Iron containing garnets and spinels with non-equivalent and antiferromagnetically coupled spin sublattices represent two important classes of soft magnetic materials [23, 24]. The ferrimagnetic rare earth iron garnets, $Ln_3Fe_5O_{12}$, are unique group of materials, which have been long studied for their novel magnetic and magneto-optical properties. The previously mentioned properties have made these materials attractive and useful for practical purposes [25, 26]. However, it is well-known, that in order to obtain desirable combination of properties it is necessary to control the preparation process. A deeper understanding of synthesis process lets us precisely control the size, composition, and crystallinity of the prepared compounds. These parameters are important for magnetic properties such as coercivity, saturation magnetization and other [27].

The main aim of this doctoral thesis was to prepare different multifunctional iron-based inorganic compounds and investigate their suitability for usage as ceramic pigments and magnetic materials. For this reason, the tasks of the present thesis were formulated as follows:

1. Synthesis, characterization and preparation of pigments and glazes of historical hematite.
2. Synthesis, characterization and preparation of pigments and glazes of $Ln_3Fe_5O_{12}$ and $LnFeO_3$ (Ln = Ce, Pr, Nd, Tb).
3. Synthesis, characterization and investigation of magnetic properties of $Ln_3Fe_5O_{12}$ (Ln = Sm–Lu).
4. Synthesis and characterization of bulk $Y_3Al_{5-x}Fe_xO_{12}$ and $Y_3Al_{5-x}Fe_xO_{12}$ thin films.

Chapter 2. Iron Pigments

Natural iron oxide pigments termed *ochres* have been used since pre-historic times and have never been fully replaced by synthetic ones [1]. From the 19th century, when chemical industry was intensively developed, synthetic iron oxide pigments appeared [1, 2, 28]. They took an important place in industry and art, because of the ability to control their synthesis process and obtain colourants with desirable properties [29, 30].

2.1. Historical Iron Pigments

Earth pigments called *ochres* are among the oldest and most common pigments used in the painting of caves [31-33], decoration of ceramic ware [34, 35] and creation of frescoes [36]. *Ochre* is a term that describes natural iron oxide rich mineral, rock, clay, or soil and refers to pigments whose colours vary from yellow to red and brown, depending on the iron oxide in the composition [37, 38]. Red colour indicates that hematite (α-Fe_2O_3) is in the composition, while yellow colour appears due to the hydrated iron oxide, goethite ($Fe_2O_3 \cdot H_2O$ or $FeOOH$) [28]. Variation in colour tones also comes from alumosilicates, quartz, calcium compounds [28] or small amount of other oxides that can be found in the composition of the mineral [39].

2.1.1. Hematite

Hematite is the oldest known iron oxide mineral and a very important pigment [40]. Pigments, which have iron(III) oxide as the main colourant in their composition, have different names. Among them there are the so called red ochre, which most likely contains some alumosilicates [41], umber and burnt sienna, which additionally contains manganese dioxide [1, 29]. Iron(III) oxide rich pigments are found on archaeological artifacts such as wall paintings [42] or on fragments of various archaeological findings from different times [34, 35] showing their importance in the past. Nowadays, developing industry pays attention to the creation of iron oxide based pigments with the ability to control all the process and properties such as colour.

11

The colour of the pigment depends not only on the mineralogical and chemical composition [28, 37], but also on the particle size [37] and shape [40]. What is more, these properties are known to be influenced by the synthesis method. A lot of different methods have been used for the preparation of hematite. One of the oldest ways is by heating the so called yellow earth, which is mainly composed of goethite [40]. The pigment obtained by this way can be named as burnt yellow earth, burnt ochre, burnt sienna or light red [43]. Other methods include precipitation using $FeSO_4 \cdot 7H_2O$ [44] or $Fe(NO_3)_3 \cdot 9H_2O$ [45, 46], thermal treatment route using modified precursors [47], microwave-assisted synthesis [48], Pechini sol-gel method [49], etc. Different synthesis routes lead to the different properties of the final product. For example, hematite, prepared by hydrothermal synthesis route was composed of polyhedron-like particles about 0.2 μm in size and of platelet particles 3 μm in size [50]. The hematite plates, obtained by alcohol-thermal reaction method were around 0.2 μm in width, and the thickness was around 0.01 μm [51]. The changes in the optical reflectance and absorption spectra by changing the particle morphology can be observed. Absorption bands are shifting to the shorter wavelength in the region from 400 to 600 nm with the reduced size of hematite particles in the optical absorption spectra. Moreover, the relative intensities also could be changed by changing the particle size: for larger particles the intensities are higher than for the smaller ones [52]. The colour of the hematite is mainly explained by three types of electronic transitions that occur in the optical absorption spectra: strong magnetic coupled Fe^{3+} ligand field transitions, pair excitations resulting from simultaneous excitation of two adjacent Fe^{3+} ions that are magnetically coupled, and ligand-to-metal charge transfer transition [52, 53]. Hematite possesses hexagonal unit cell and belongs to the space group $R\bar{3}c$ (167) [54]. The arrangement of cations in hematite produces pairs of $Fe(O)_6$ octahedra, where Fe^{3+} is in the high-spin state [40]. In octahedral coordination, the Fe $3d$ atomic orbitals are split into two sets of orbitals labelled as t_{2g} and e_g as shown in Figure 2.1a. The best way to explain ligand field (or d-d) transitions in octahedral coordinated Fe^{3+} is by showing the energies of the Fe^{3+} ligand field states as a

function of crystal field splitting (10Dq) in the well-known Tanabe-Sugano diagram (Figure 2.1b).
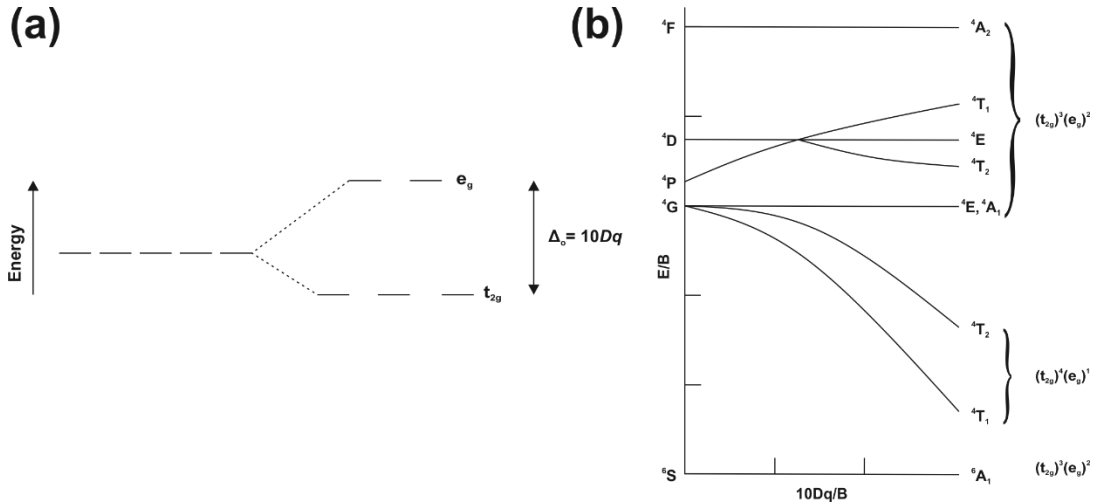
Figure 2.1. Energy splitting of d orbitals in octahedral field (a) and Tanabe-Sugano diagram for high-spin Fe^{3+} in either octahedral or tetrahedral coordination (b).

As can be seen from Figure 2.1b, the ground state $^6A_1$ (^6S) arises from the ground state $(t^\alpha_{2g})^3(e^\alpha_g)^2$ configuration of high-spin Fe^{3+}, where α refers to spin-up and β to spin-down. Ligand field (or d-d) transitions involve excitation from ground state $^6A_1$ to the excited ligand field states. The first possible excited states $^4T_1$ (^4G) and $^4T_2$ (^4G) arises from configuration $(t^\alpha_{2g})^3(e^\alpha_g)^1(t^\beta_{2g})^1$. Other states shown in Figure 2.1 result from "spin-flip" configurations $(t^\alpha_{2g})^2(t^\beta_{2g})^1(e^\alpha_g)^2$ and $(t^\alpha_{2g})^3(e^\alpha_g)^1(e^\beta_g)^1$. All mentioned transitions are, in principle, both spin and parity forbidden. However, they become allowed due to the magnetic coupling of electron spins of adjacent Fe^{3+} cations. Additionally, this coupling is responsible for the simultaneous excitation of two Fe^{3+} ions. Ligand-to-metal charge transfer transitions occur at energies higher than those of ligand field transitions [40, 53, 55]. Other factors significantly affecting colour are related to crystal defects, adsorbed impurities, and the degree of particle packing [55]. The colour of the hematite pigment changes from strong maroon for particles of around 0.3 μm to the purple for particles of around 3 μm [50]. This can be related to the differences in the scattering of visible light by changing particle size [37].

For the determination of pigment colour, few colour systems are used. One of them is defined according to the Commission Internationale de l'Eclairage (CIE) through $L*a*b*$ coordinates [56]. In this system $L*$ is the colour lightness ($L* = 0$ for black and $L* = 100$ for white), $a*$ is a green (-)/red (+) axis, and $b*$ is the blue (-)/yellow (+) axis (see Figure 2.2). The high value of $a*$ presents that hematite is in the composition of red ochre pigment [28].

$L* = 100$

-a*   **+b***

-b*   **+a***

$L* = 0$
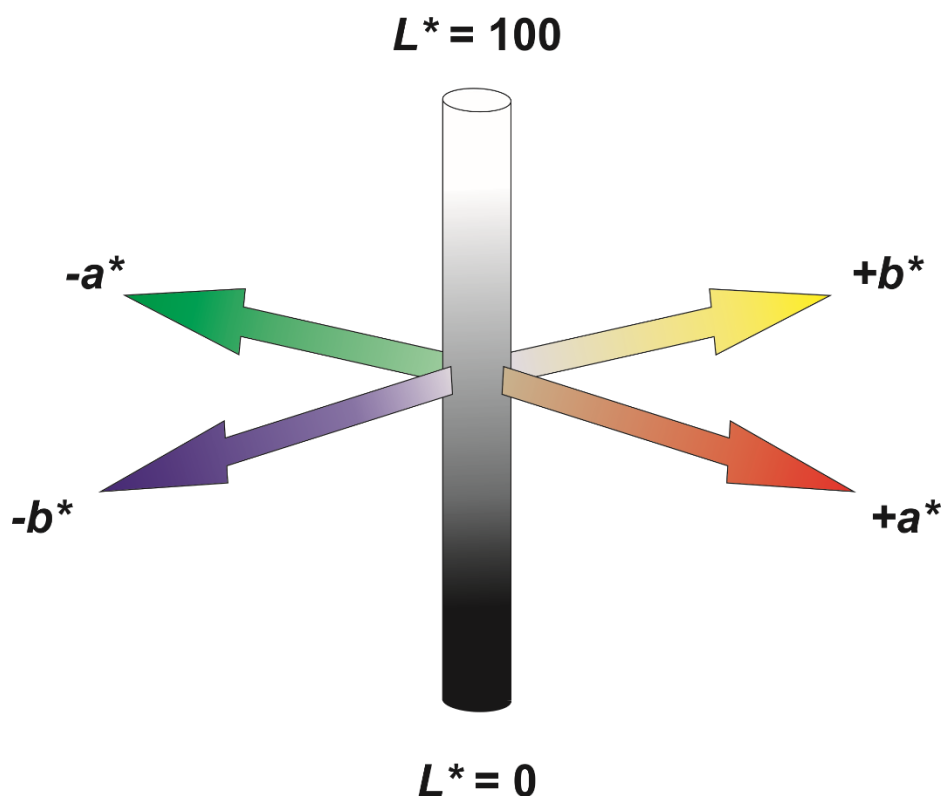
Figure 2.2. Graphical representation of the CIE $L*a*b*$ colour system.

2.1.2. Other Historical Pigments

Other well-known iron earthy pigment used since the prehistoric times is called yellow ochre. The word *ochre* comes from Greek word *Ochros*, meaning pale yellow [2]. In this pigment goethite (α-FeOOH) dominates and gives its yellow colour [28]. This pigment was used in various fields from rock art [57] pottery [58], to the paintings [59]. The hue of pigment depends on the other components as well as its crystallinity. Only few percent of hematite in the composition can change colour of goethite to brownish or reddish [1]. Very often, samples from the same discovery place contain various iron earthy

pigments [32, 34]. It is claimed, that ochres containing hematite or goethite can be distinguished from diffuse reflectance spectra [32]. It was shown, that ochres can be differentiated by determining the inflexion point, which is associated to the sharp slope of diffuse reflectance spectra. Very clear differences can be seen, as this point is said to be 550 nm for pure goethite and 580 nm for pure hematite. Mixture of both pigments gives orange colour and spectra with the features between the spectra of hematite and goethite [28]. Other factor, which can influence the colour of goethite, is change of various preparation conditions during the synthesis [60]. Brown ochre is composed of around 50% of Fe_2O_3 and 6–14% of FeO, and some alumosilicates. Brown ochre is obtained by burning yellow, red ochre, red sienna, green earth and other earthy pigments [5].

Vivianite is a phosphate mineral ($Fe_3(PO_4)_2 \cdot 8H_2O$), which has also been used as a pigment. The colour of earthy vivianite ranges from light greyish green to saturated blue, frequently being light blue. It was even used in polychrome on wood or stone and wall paintings [61], although it was not very common because of its dim colour and low hiding power [5].

Naturally occurring magnetite (Fe_3O_4) has poor tinting strength as a black pigment [29], therefore it was not used so often in the past, even there is an example, that it was found in the pottery of Neolithic period [62]. Nevertheless, synthetic pigment can be obtained with very high tinting strength by controlling synthesis conditions [29]. This pigment belongs to the class of magnetic pigments and is used in inks and toners in photocopying, facsimile machines [40] and in security inks [40, 63].

Green earth is another type of iron containing pigment. There are a few types of minerals that are responsible for the green colour in green earth pigments, among them are minerals celadonite and glauconite are the most common [1, 64]. Other minerals that can act as pigments are smectite, chlorite, serpentines and pyroxenes [64, 65]. The chemical composition of celadonite and glauconite is very similar, but they are formed under different geological conditions. Green earth pigments containing these two minerals were the most common pigments in Byzantine wall painting [42] and were also found in the

wall painting fragments in Pompeii area showing, that they were used even in the Roman age [66].

2.2. Modern Iron Pigments

In the history of pigments Prussian blue is the first modern pigment, because it was the first chemically synthesized pigment prepared in 1704 [2]. Synthetic iron oxide pigments, called Mars colours were prepared in the 19th century [1]. Nowadays in developing stable new pigments, lanthanide oxides are used instead of toxic elements such as cadmium, cobalt, lead and chromium [9, 10, 67].

2.2.1. Iron Pigments with Lanthanides in the Composition

During the last few decades, many investigators turned to environmental-friendly pigments with low toxicity rating. Among these pigments there are lanthanide containing oxides [10]. The change of the colour is possible just by variation of lanthanide ion in the composition of the pigment. One group of modern inorganic iron pigments is orthoferrite. Rare earth containing orthoferrites $LnFeO_3$ (Ln = Gd, La, Yb, Tm, Lu, Er, Sm, Nd, Ho, Pr) were synthesized by different methods showing variation in colours [13-16, 68]. The orthoferrite pigments synthesized by solid-state reaction method and containing bigger lanthanide ions (Gd^{3+} and La^{3+}) were indicated by more orange colour, while pigments with smaller lanthanide ions (Lu^{3+}, Tm^{3+} and Yb^{3+}) were shown to be dark reddish brown colour [14]. Interestingly, $LaFeO_3$ synthesized from polymeric precursor was also predominantly orange [13]. The substitution of iron ion by aluminium in $LaFeO_3$ changes the colour of the pigment from brown to yellow. The colour coordinates $a*$ and $b*$ decrease presenting the loss of red hue and weakness in the intensity of yellowness [69]. Substituted pigments showed appropriate properties to be used in ceramic and polymer colouring, because of their intense shade and low toxicity [70]. Synthesis of $LnFeO_3$ (Ln = Er, Nd, Sm) by precursor method revealed reddish dark colour of obtained compounds [16]. $PrFeO_3$ prepared by solid-state reaction method with the

increasing calcination temperature showed various hues of brown colour – from light chocolate brown to dark brown [68].

The colour of the pigment can also be changed by the addition of different amount of chromophore as dopant. Ceramic pigments with the composition of $Fe_2O_3 \cdot CeO_2$ doped with praseodymium showed that a higher amount of Ce and Pr led to a light brown colour [7]. Similar composition pigments obtained by solid-state reaction and sol-gel method presented shades ranging from light to dark-brown, also showing differences depending on the synthesis method [11]. Other examples of doped pigments can be metal oxide-doped $LuFeO_3$ [20], $MgFe_{2-x}Er_xO_4$, presenting deep brick red to brown colours and showing good resistance to sunlight [71], $Bi_{1-x}MFeO_3$ (M = Y, La), showing the potential application in the colouring of various plastic materials [12] or $Y_{2-x}Tb_xZr_{2-y}Fe_yO_{7-y/2}$, which is suitable for ceramic colouring application [72].

All the examples mentioned above demonstrate that the investigation and development of new, environmental-friendly and low-toxicity pigments are relevant nowadays.

2.2.2. Other Iron Pigments

Prussian blue pigment, hydrated iron(III) hexacyanoferrate(II), became popular because of its low cost and intense colour [73]. There is the so-called "insoluble" $Fe_4^{III}[Fe^{II}(CN)_6]_3 \cdot xH_2O$ (x = 14–16) and the "soluble" $M^I Fe_4^{III}[Fe^{II}(CN)_6]_3 \cdot yH_2O$ (y = 1–5, M is monovalent cation such as K^+ or NH_4^+) Prussian blue [74]. This pigment was found among other blue pigments in the painting of an Italian artist from the 19th century [75] and even in the wallpaper from the same period [76].

Spinel type materials are an important class of ceramic pigments and are widely used in the decoration of ceramic products [77, 78]. Some iron-rich modern pigments such as $MgFe_2O_4$ and $ZnFe_2O_4$ provide reddish colour [46]. $MgFe_2O_4$ prepared by polymeric precursor method showed the increase in reflectance up to 700 nm, leading to a yellow-orange colour, whereas the maximum reflectance for $ZnFe_2O_4$ occurred between 650–700 nm, leading to the

17

red-brick colour [79]. Ceramic pigments prepared by the complex polymerization method with the structure of $CoFe_2O_4$ revealed dark shades, from black to grey [78]. The spinel type $CoFe_2O_4$, $NiFe_2O_4$, $ZnFe_2O_4$, perovskite type $YFeO_3$, and garnet type pigments $Y_3Fe_5O_{12}$ were successfully used for the preparation of black ceramic glazes [80]. Series of different Co–Cr–Fe–Mn spinel type pigments were prepared and have been used for ceramic glazes as well. All pigments showed deep black colour except few pigments that were bluish green or dark brown [81]. Whereas, the substitution of Fe^{3+} for Al^{3+} in $Co_{0.5}Mg_{0.5}Al_{2-x}Fe_xO_4$ demonstrated the colour change from blue to black. Colour coordinate $a*$ increased from -15.67 to 2.61 showing the loss of green hue, while $b*$ increased from -38.84 to 6.35 demonstrating the loss of blue hue. The obtained pigments showed a good thermal and chemical stability [82]. These properties of pigments are especially important for the application in ceramic colouring.
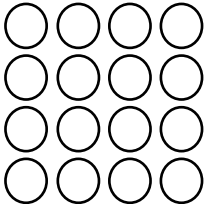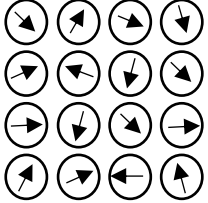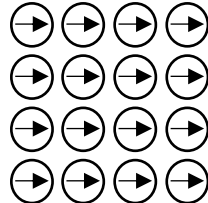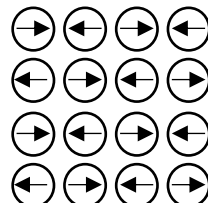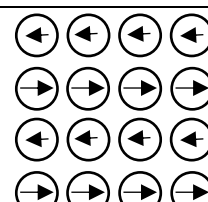
Chapter 3. Magnetic Materials

Over the past few decades, magnetic materials have been in focus of interest due to the fact that they are widely used in modern technology [24]. The demand for new magnetic materials is growing, because of the developing technologies and application of magnetic materials in such areas as energy conversion devices, field generation, sensors, actuators, data storage and memory devices [83]. Suitable magnetic properties have a huge impact on the usage of the materials and even in the miniaturization of machines and devices for which they are used [84].

3.1. Classification of Magnetic Materials

Materials can be classified into the following five groups: diamagnetic, paramagnetic, antiferromagnetic, ferromagnetic and ferrimagnetic (Table 3.1).

Table 3.1. Types of magnetic materials [85].

Type of Magnetism	Magnetic moment orientation	
Diamagnetism		No magnetic moment
Paramagnetism		Randomly oriented magnetic moments
Ferromagnetism		Parallel aligned magnetic moments
Antiferromagnetism		Antiparallel aligned magnetic moments
Ferrimagnetism		Different magnitude magnetic moments

In diamagnetic materials all atoms have paired electrons. In fact, all materials show some diamagnetism, as all materials have paired electrons. The net magnetic moment is zero under no applied magnetic field. However, under applied magnetic field these materials are magnetized opposite to the direction of an applied magnetic field. In paramagnetic materials the atoms or ions have unpaired electrons. Their spins and magnetic dipoles are oriented randomly and sum magnetic moment is zero. However, in the presence of magnetic field and there is a partial alignment of magnetic moments in the direction of magnetic field, which also depends on temperature. In antiferromagnetic materials,

magnetic moments of the atoms are aligned antiparallel and the net magnetic moment is zero. Ferromagnetic materials have the parallel alignment of unpaired electron spins and magnetic dipoles thus creating the sum magnetic moment. Compounds with complex crystal structure usually show ferrimagnetic behaviour. In these materials some crystal sites are characterized with parallel and some with an antiparallel alignment of magnetic dipoles. As the number of moments can be different, the sum magnetic moment depends on the number of dipoles oriented in the opposite directions [85, 86].

The most important and practical magnetic materials belong to the ferromagnetic and ferrimagnetic type. On the basis of their hysteresis characteristics these materials are also classified as either soft or hard [87]. Hysteresis characteristics are obtained from hysteresis loop, which shows the response of magnetization (M) to an applied magnetic field (H) [22]. Soft magnetic materials are easily magnetized and demagnetized, while hard materials are difficult to demagnetize. This is the reason why soft magnetic materials are used for temporary magnets and hard ones – for permanent magnets. Materials between soft and hard are usually excluded as magnetic recording media [85].

3.2. Magnetic Properties of Materials

The magnetic properties of solid materials occur mainly from magnetic moments associated with their electrons. Magnetic moment of the material is related to the orbital motion of the electron around the nucleus and electron spinning around its axis (Figure 3.1). The total magnetic moment for an atom is the sum of magnetic moments of an individual electrons, including cancelation of opposite magnetic moments [22, 87].

The development of magnetic materials that can be used for practical applications requires optimization of intrinsic and extrinsic magnetic properties [88]. Intrinsic properties do not depend on the microstructure of the materials, while extrinsic magnetic properties can be controlled by the microstructure. Intrinsic magnetic properties include saturation magnetization (M_s), Curie

temperature (T_c), magnetocrystalline anisotropy and magnetostriction. The magnetic permeability (μ), coercive force (or coercivity, H_c) and remanent magnetization (or remanence, B_r) are extrinsic magnetic properties [22, 88, 89].
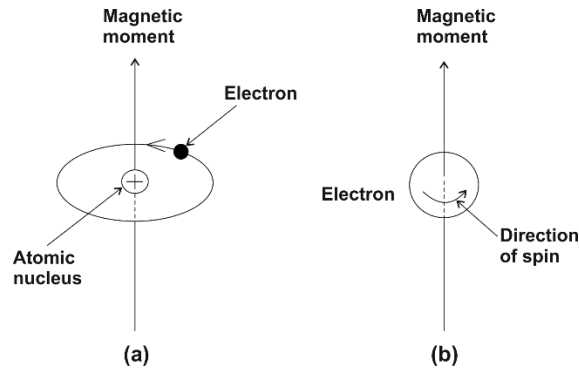
Figure 3.1. Magnetic moment associated with an orbiting electron (a) and spinning electron (b) [87].

Saturation magnetization is the maximum magnetization value that can be reached in the magnetic field. This property is characteristic for ferromagnetic and ferrimagnetic materials. Saturation magnetization sometimes is called spontaneous magnetization even though this term is usually used to describe the magnetization with a single domain [85]. Magnetic domain is a small volume region where all magnetic moments are aligned in the same direction. When saturation magnetization is reached, all the magnetic dipoles are aligned with the magnetic field. Saturation magnetization is temperature dependent and decreases with the increasing temperature and reaches zero at Curie temperature [87, 90]. Temperature influences the magnetic behaviour, as raising the temperature thermal movement of the atoms increases and the alignment of magnetic moments decreases.

Curie temperature, or Curie point, is the temperature at which ferromagnetic or ferrimagnetic material becomes paramagnetic. Above this point, thermal energy overrides any interactions between magnetic moments, whereas below this temperature interactions of magnetic moments take place and the moments are aligned [85, 87]. Another intrinsic magnetic property is magnetocrystalline anisotropy which means, that magnetization is different under the applied magnetic field and depends on crystallographic orientation

[22, 91]. A polycrystalline sample with randomly oriented grains has no net crystal anisotropy [91-93]. Magnetostriction is the property of ferromagnetic or ferrimagnetic materials, which undergoes the shape change under the magnetic field [94].

The magnetic materials are also characterized by the way the magnetization (M) or magnetic induction (B) range with the applied magnetic field. Susceptibility (χ) and permeability (μ) are properties that describe this relation. The susceptibility shows how magnetic material acts in the magnetic field. Magnetic susceptibility indicates whether the material is attracted or repelled by the influence of the magnetic field [93]. In the case of paramagnetic materials, magnetic susceptibility is positive and the material is attracted by the magnetic field, whereas in the diamagnetic materials the value of susceptibility is negative and materials are repelled by the magnetic field. Ferromagnetic, ferrimagnetic and antiferromagnetic materials have positive susceptibility [86]. Permeability measures how permeable the material is to the applied magnetic field [93].

Other extrinsic magnetic properties such as coercive force and remanent magnetization are also characteristic for the ferromagnetic and ferrimagnetic materials. Coercive force is a parameter which shows how the material sustains an external magnetic field without being demagnetized. Remanent magnetization determines the magnetization that is left after removal of the magnetizing field [95]. These parameters can be obtained from the magnetization curve of the material. Magnetization curve shows the relationship between M or B and H. The magnetization curves of diamagnetic, paramagnetic and antiferromagnetic materials are linear. In the case of ferromagnetic and ferrimagnetic materials, magnetization curves are called hysteresis loops [93]. Hysteresis loop with indicated remanent magnetization, coercivity and saturation magnetization is shown in Figure 3.2. The shape of the hysteresis curve depends on the crystallinity of material, preferred orientation of the grains in the polycrystalline sample, phase purity, porosity of the material, on temperature and mechanical stress. The characteristic shape of hysteresis loop

for soft magnetic materials is thin and narrow and for hard ones is wide and square [87].
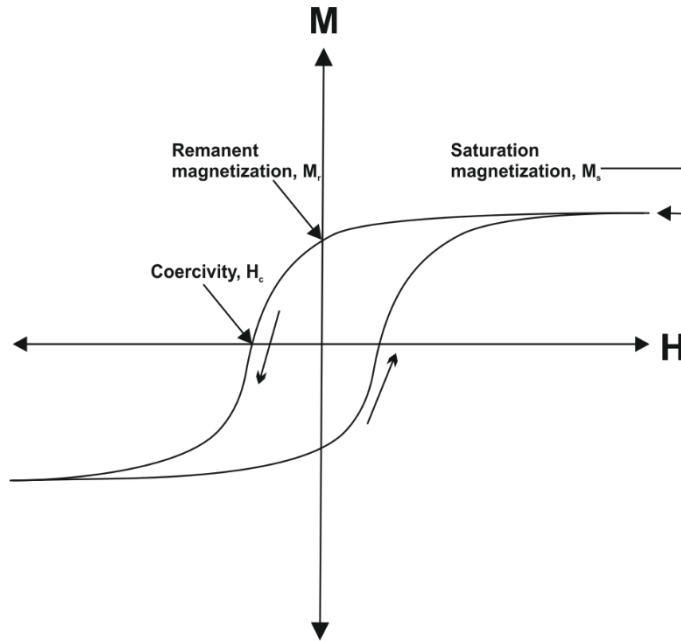
Figure 3.2. Magnetic hysteresis loop with indicated important parameters [92].

The remanence, coercive force and Curie temperature are important properties for the classification of magnetic materials, either soft or hard. Soft magnetic materials require the value of coercive force to be low (best equal to zero). In this way, the material will be demagnetized after the removal of the external field. In the case of hard magnetic material, the material will stay magnetized after removing the magnetic field, meaning that coercive force [84] and remanence are high [87]. According to *Coey*, the hard and soft magnets have $H_c > 400$ kA/m (~5 kOe) and $H_c < 10$ kA/m (~125 Oe), respectively [22].

3.3. *Application of Magnetic Materials*

The application area of magnetic materials can be based on their properties. Diamagnetic and paramagnetic materials do not have permanent net magnetic moment, therefore they featuring a smaller application. However, the most important diamagnetic materials are high-temperature superconductors [93]. These superconductors have a number of potential applications such as energy-storage flywheels, the production of sensitive magnetometers based on SQUIDs,

powerful superconducting electromagnets, low-loss power cables and magnetic levitation trains [22].

On the other hand, ferromagnetic and ferrimagnetic materials are widely used. These materials are inseparable part of our everyday life. Soft magnetic materials are used in cores of transformers, generators, and motors, also in cores of special transformers and inductors, which are used in electronics, also in different components of microwave systems [91, 96, 97]. Meanwhile, hard magnets are used in different sound systems such as loudspeaker magnets, in automobiles for cooling and heating fans, seat and window adjusters, in small motors of computers, printers, scanners and so on. For example, such devices as transformers are used to increase or decrease the altering voltages and they are the part of electrical power grids [91]. The main material used for magnet cores in transformers and electrical machines is Fe-Si alloy [22, 91, 97].

Magnetic materials are important in the data storage industry. Magnetic data storage has been used in such applications as audio tapes, video cassette recorders, computer hard disks, credit cards, etc. [93, 96]. For example, a hard disc drive is an inexpensive data storage device, which is able to manage huge amount of information. As can be seen from Figure 3.3, the magnetic materials are an inseparable part of this device [98].

The main components containing magnetic materials are the magnetic head and the magnetic recording media. The write and read heads must be of high-permeability, low-coercivity magnetic materials able to work at reasonably high frequencies. Meanwhile, magnetic recording media must have coercivity not too high to write on and not too low to resist demagnetization and hold the recorded pattern, and at the same time the magnetization has to be not too low to provide a readable signal to the read head [91]. Co-based materials are used for magnetic recording layer even in new high density recording technologies [99].
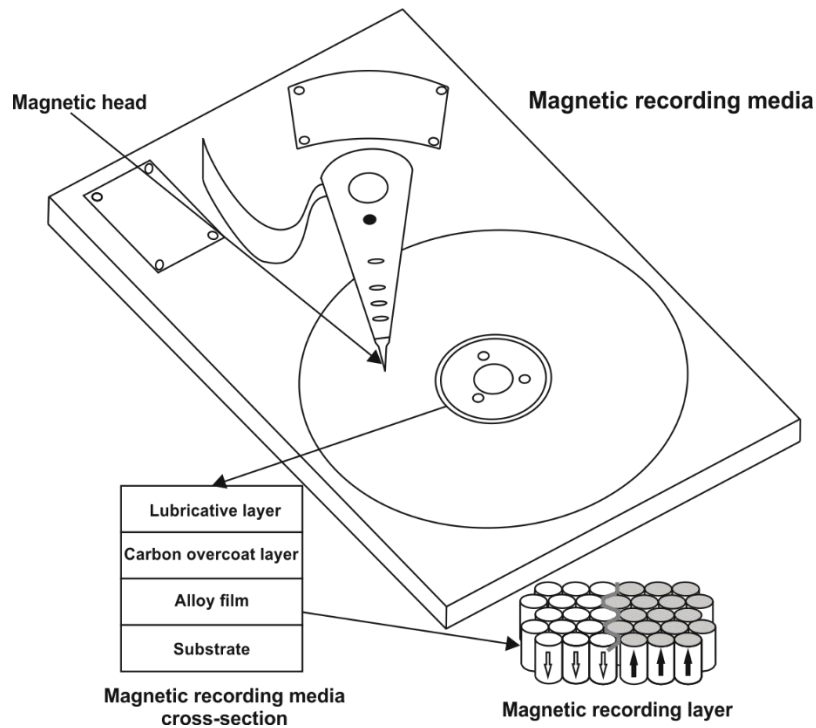
Figure 3.3. Hard disc drive and magnetic recording media structure [98].

Magnetic materials are used in the biotechnology and medicine for the cell separation, magnetic resonance imaging (MRI), drug and gene delivery, minimally invasive surgery, radionuclide therapy, hyperthermia and artificial muscle applications [100-103]. Iron oxide coated with dextran is an example of the magnetic materials used for cell separation [100]. Magnetic nanoparticles such as superparamagnetic iron oxides or ultrasmall superparamagnetic iron oxides are used in MRI as contracting agents in order to obtain better signal from the scanner [101]. Drug delivery process is useful for the regional therapy and may improve the effectiveness of the treatment. Magnetic particles are able to export the drugs in the desired place [102]. Materials used for drug targeting and magnetic separation should show high magnetization and high susceptibility [100]. Usually, coated magnetite particles are used for drug delivery [100, 104]. Magnetic nanoparticles are used as heat sources for magnetic hyperthermia to rise tissue temperature to around 43 °C in order to make a tumour cell more sensitive compared to the healthy cells [105]. For hyperthermia applications Curie temperature is an important parameter, as the exchange from ferromagnetic to paramagnetic state of the material is used as an on-off switch

[100, 105]. Such material as γ-Fe_2O_3 showed good properties for application for hyperthermia treatment [106].

All the mentioned applications show, that magnetic materials are very important in our everyday life, modern technology and medicine. Understanding the formation of these materials can be useful for the improvement of their properties as well as for the finding the right application field where they can be most useful.

Chapter 4. Lanthanide Iron Garnets

Lanthanide iron garnets belong to the unique group of ferrite materials having important practical applications because of their novel magnetic and magneto-optical properties. Ferrimagnets have found the application in passive microwave components such as isolators, circulators, phase shifters, miniature antennas operating at a wide range of frequencies (1–100 GHz), magnetic recording media and other [25, 107, 108].

4.1. Crystal Structure

The prototype of the lanthanide iron garnets is a well-known yttrium iron garnet ($Y_3Fe_5O_{12}$ or YIG). First magnetic garnets were prepared by F. Bertaut and F. Forrat (1956) [109] and analysed by S. Geller and M. A. Gilleo (1957) [110]. Garnet type compounds crystallize in the cubic lattice with the space group $Ia\overline{3}d$ (230) [111]. General formula for lanthanide iron garnets is $R_3Fe_5O_{12}$, where R is rare-earth trivalent cation [112]. Cubic unit cell is composed of eight formula units, $Y_3Fe_3Fe_2O_{12}$, where Y^{3+} ions are in 24(c) dodecahedral site, three Fe^{3+} ions are in 24(d) tetrahedral site, and two Fe^{3+} ions are in 16(a) octahedral site [25, 113]. The crystal structure of YIG is presented in Figure 4.1. Some lanthanide iron garnets are rhombohedral with the space group $R\overline{3}c$ at low temperatures (4.2 K) [114].

26
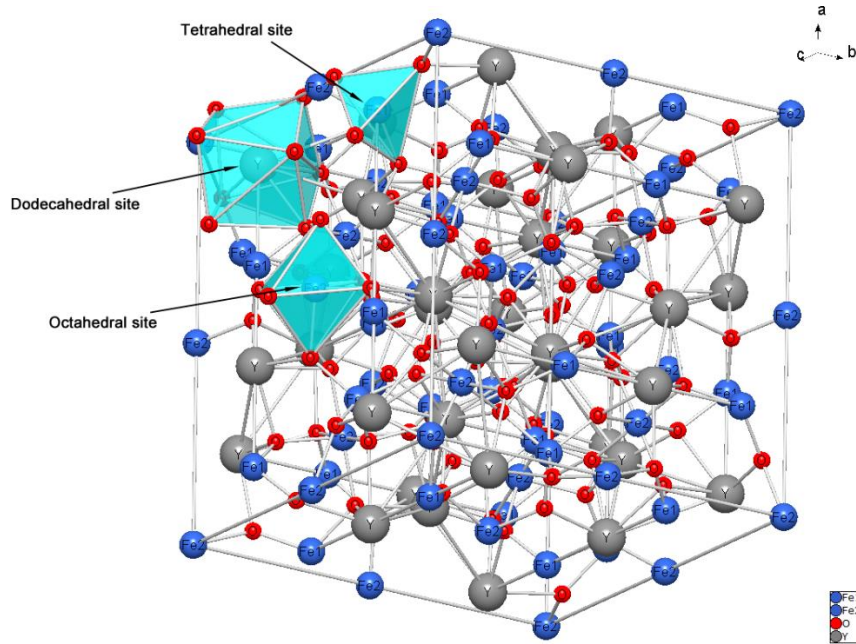
Figure 4.1. Crystal structure of YIG.

In rare-earth iron garnets magnetic moments of Fe^{3+} ions on 24(d) sites and Fe^{3+} ions on 16(a) sites are antiparallel to the magnetic moments of rare earth ions on 24(c) site [114, 115]. Net magnetic moment of Fe^{3+} ions is 5 μ_B per formula unit (40 μ_B per unit cell) at 0 K. The net magnetization of garnet is the magnetization of rare earth c sublattice minus the net magnetization of a–d sublattice [116]. The nature of magnetic superexchange interaction depends on the magnetic ion as well as bond length and bonding angle. Magnetic interaction between a–d sublattices is stronger than between c–a, because the angle Fe^{3+}(a)–O^{2-}–Fe^{3+} (d) is 126.6° and the angle Ln^{3+}(c)–O^{2-}–Fe^{3+} (a) is 100°. The interaction of a–d sublattices is dominant for all magnetic garnets.

At low temperatures, magnetic moments of Ln^{3+} ions are large and saturation magnetization is parallel to the magnetic moment of Ln^{3+} ion. With the increasing temperature sublattice moment of the Ln^{3+} ions decreases sharply, while the moment of iron sublattices decreases slower, because of the larger a–d coupling [116]. However, the interaction can be changed by the substitution of different ions [25].

It is well-known, that iron ion substitution by nonmagnetic ions in YIG has an influence on magnetic and other physical properties. Usually, smaller ions like Al^{3+} and Ga^{3+} preferentially occupy smaller tetrahedral sites, while larger ions like In^{3+} and Sc^{3+} occupy octahedral sites [113]. In the case of iron ion replacement by aluminium, magnetic moments for both octahedral and tetrahedral sites decrease with the higher amount of aluminium in the composition. This change can be related to the frustration of the lattice, as the cubic lattice constant decreases with the increasing aluminium concentration [117]. The Curie temperature also decreases because the number of Fe^{3+}–O^{2-}–Fe^{3+} interactions decreases [113, 118].

4.2. Magnetic Properties

Ferrimagnetic rare-earth iron garnets belong to the class of soft magnetic materials [23]. As was mentioned earlier, these materials are easily magnetized and demagnetized [84, 85]. The magnetic properties for specific applications can be controlled by controlling the preparation conditions or by substituting some elements in the garnets [119]. Such properties as saturation magnetization (M_s) and coercivity (H_c) are very important for practical applications [120, 121]. Lanthanide iron garnets have been produced using solid-state reactions [122-124], co-precipitation [125-127], hydrothermal synthesis [108, 128], sol-gel synthesis [129-133], low temperature liquid phase epitaxy (LPE) [134, 135], and pulsed laser deposition (PLD) [136]. As can be seen from the Table 4.1, different synthesis methods lead to different magnetic properties.

In $Y_{3-x-y}Ce_xDy_yFe_5O_{12}$ (x = 0–0.1, y = 0–1.0) nanoparticles saturation magnetization increased with the higher amount of Ce and decreased with the higher amount of Dy [121]. Saturation magnetization and remanence increased, while coercivity decreased with the enhanced amount of Ho^{3+} in $Y_{3-x}Ho_xFe_5O_{12}$ (x = 0.1, 0.3, 0.6, 0.9, 1.5) polycrystalline samples [137]. On the other hand, the opposite effect was observed when Y^{3+} was substituted by Gd^{3+} ion in $Y_{3-x}Gd_xFe_5O_{12}$ (x = 0, 0.25, 0.5, 0.75, 1.0). The saturation magnetization decreased and coercivity increased by increasing Gd^{3+} concentration [138].

Table 4.1. Magnetic properties of lanthanide (or yttrium) iron garnets.

$R_3Fe_5O_{12}$	Synthesis method	Crystallite size (nm)	M_s (emu/g)	M_r (emu/g)	H_c (Oe)	T_c (K)	Ref.
$Y_3Fe_5O_{12}$	Sol-gel	34.1	25.1	-	-	-	[131]
		53.3	26.7	-	-	-	
		62.3	27.6	-	-	-	
$Y_3Fe_5O_{12}$	Mechanical alloying and calcination	128	26.9	2.5	10.4	553	[139]
$Gd_3Fe_5O_{12}$		167	1.6	0.9	65.3	564	
$Lu_3Fe_5O_{12}$	Solid-state	-	14	-	-	539	[140]
$Sm_3Fe_5O_{12}$	Hydrothermal	-	13.3	-	-	562	[128]
$Eu_3Fe_5O_{12}$		-	5.7	-	-	550	
$Gd_3Fe_5O_{12}$	Solid-state	-	0.3	0.25	170	-	[124]
$Tb_3Fe_5O_{12}$		-	2.5	0.79	25	-	
$Y_3Fe_5O_{12}$		-	17.5	1.0	13	-	
$Dy_3Fe_5O_{12}$	Combustion	97	8.29	2.64	151	-	[141]

The Al^{3+} substituted garnet with the composition of $Y_3Fe_{5-x}Al_xO_{12}$ showed diminished saturation magnetization and coercivity with the higher concentration of aluminium [142-145]. Substitution at the tetrahedral site by Ga^{3+} ion lowered the magnetization, while substitution at the octahedral site by Sc^{3+} ion increased the magnetization [146].

4.3. Application of Lanthanide Iron Garnets

$Y_3Fe_5O_{12}$ is one of the most widely known ferrimagnetic material due to its application potential in optics, magneto-optics and microwave devices. As microwave ferrite, YIG is used in the form of bulk and films. Microwave devices include different circulators, isolators, phase shifters, etc. [23]. Moreover, development of wireless infrastructure will continue to use magnetic materials

based on yttrium iron garnet. Ferrite based isolators are used in amplifier chains in base station transceivers [147].

Another important area of application is optical fibre communication systems. Optical isolators are generally needed to eliminate the influence of reflected light. Faraday rotators made of magneto-optical garnet crystals can be used for optical isolators [148-150]. $Y_3Fe_5O_{12}$, $Tb_3Fe_5O_{12}$, $Dy_3Fe_5O_{12}$, $Ho_3Fe_5O_{12}$, $Er_3Fe_5O_{12}$, $Gd_3Fe_5O_{12}$, $Yb_3Fe_5O_{12}$ were used in the fabrication of magneto-optic switches, isolators, modulators and deflectors. According to the results obtained from the wavelength and temperature dependence of the Faraday rotation and optical loss it was shown that $Y_3Fe_5O_{12}$ and $Ho_3Fe_5O_{12}$ are the best for devices which operate at a single wavelength, while $Yb_3Fe_5O_{12}$ is the best for broadband operation [148]. Bismuth-substituted rare-earth iron garnets are also used as magneto-optical materials [149]. YIG-Bi_2O_3 nanocomposite materials were prepared for their potential use in optics, magneto-optics and microwave devices [151, 152]. Nanocrystalline gadolinium iron garnet demonstrated a high resistivity and low microwave losses, which are properties suitable for circulator and isolator applications and also appropriate for communication industry [108].

Evaluation of cytotoxicity of Al-substituted $Y_3Fe_5O_{12}$ was performed in order to investigate its potential usage in biotechnology and medicine. $Y_3Fe_{5-x}Al_xO_{12}$ was showed to be non-cytotoxic and possibly suitable for hyperthermia treatment [153]. In the fast changing life new solutions are required for improving magnetic data storage devices. Cobalt substituted yttrium iron garnet was used for ultrafast all-optical photo-magnetic recording [154], showing that iron containing garnets are extremely important in nowadays modern life.

Chapter 5. Experimental

5.1. Chemicals

These materials were used in the syntheses: $Fe(NO_3)_3 \cdot 9H_2O$ (98.0% Duro-Galvanit-Chemie), $Al(NO_3)_3 \cdot 9H_2O$ (98.0% Eurochemicals), Nd_2O_3 (99.9% Fluka Chemie), Tb_4O_7 (99.9% Merck), Pr_6O_{11} (99.9% Merck), Y_2O_3 (99.99% Aldrich), Sm_2O_3 (99.99% Aldrich), Eu_2O_3 (99.9% Alfa Aesar), Gd_2O_3 (99.9% Alfa Aesar), Dy_2O_3 (99.9% Aldrich), Ho_2O_3 (99.9% Aldrich), Er_2O_3 (99.9% Aldrich), Tm_2O_3 (99.99% Alfa Aesar), Yb_2O_3 (99.9% Aldrich), Lu_2O_3 (99.99% Treibacher), $(NH_4)_2Ce(NO_3)_6$ (99.5% Merck), HNO_3 (65 wt.% Eurochemicals), acetic acid CH_3COOH (99.5 wt.% Eurochemicals), 1,2-ethanediol $C_2H_6O_2$ (99.5 wt.% Aldrich), glycerol $C_3H_8O_3$ (99.0 wt.% Standard), polyvinyl alcohol (PVA, molecular weight 70000, Merck). Pb_3O_4 (96.0% Kremer Pigmente), SiO_2 (97.0% Kremer Pigmente)

Three commercial pigments named light red iron(III) oxide, dark red iron(III) oxide and burnt red iron(III) oxide from Kremer Pigmente were analysed.

5.2. Preparation of Samples

All powder samples were synthesized by an aqueous sol-gel method.

5.2.1. Synthesis of α-Fe₂O₃

Firstly, iron(III) nitrate was dissolved in 100 ml 0.2 M CH_3COOH and stirred at 65–70 °C for 1 h. In the following step, 1,2-ethanediol, a complexing agent, was added to this solution and the solution was stirred for an additional 1 h at the same temperature. After stirring for 1 h, the obtained solution was evaporated at 65–70 °C. The prepared Fe–O gel was dried in oven at 100–110 °C. Dried gel powders were ground in agate mortar and heated in air at 500, 600, 700, 800, 900 and 1000 °C for 5 h at a heating rate of 3 °C/min.

Ceramic glazes with iron pigments were prepared with Pb_3O_4, SiO_2 in molar ratio of 2.85:1.9 and using 5 wt.% of pigment. All components were mixed

with 2 ml of water and terracotta plates were covered with glaze mass [155]. The glaze samples were fired at 800, 900 and 1000 °C for 1 h.

5.2.2. Synthesis of $Ln_3Fe_5O_{12}$ and $LnFeO_3$ (Ln = Ce, Pr, Nd, Tb)

For the preparation of $LnFeO_3$ and $Ln_3Fe_5O_{12}$ (where Ln = Nd, Tb, Pr, Ce) stoichiometric amount of appropriate lanthanide oxide was dissolved in 10 ml of hot nitric acid, then mixed with $Fe(NO_3)_3 \cdot 9H_2O$ solution in 50 ml of water and stirred at 65–70 °C for 1 h. For the preparation of Ce–Fe–O gel, $(NH_4)_2Ce(NO_3)_3$ was dissolved in 10 ml of water and $Fe(NO_3)_3 \cdot 9H_2O$ solution in 50 ml of water. After stirring at 65–70 °C for 1 h 1,2-ethanediol, as complexing agent was added to this solution. After 1 h the solution was continuously stirred and concentrated by evaporation of solvent at 65–70 °C. Prepared gels were dried in oven at 100–110 °C. Dried gels were ground in agate mortar and heated in air at 800 °C for 2 h. After an intermediate grinding in an agate mortar the powders were additionally sintered at 1000 °C for 10 h. The heating rate was 10 °C/min.

Nd–Fe–O, 3Nd–5Fe–O, Tb–Fe–O, 3Tb–5Fe–O, Pr–Fe–O, 3Pr–5Fe–O, Ce–Fe–O and 3Ce–5Fe–O precursor gels sintered at 1000 °C for 10 h were used as pigments (5 wt.%) for the preparation of ceramic glazes. Ceramic glazes were prepared by the same way as with Fe_2O_3. The prepared terracotta samples were fired only at 1000 °C for 1 h.

5.2.3. Synthesis of $Y_3Fe_5O_{12}$ and $Ln_3Fe_5O_{12}$ (Ln = Sm–Lu)

The Tb–Fe–O precursor gel was prepared using stoichiometric amounts of $Fe(NO_3)_3 \cdot 9H_2O$ and Tb_4O_7 as starting materials. Firstly, Tb_4O_7 was dissolved in 5 ml of nitric acid under stirring and heating. When the clear solution was obtained, the excess of acid was removed by evaporation till the dry residue. In the following step, 20 ml of deionized water was added and clear solution was obtained. $Fe(NO_3)_3 \cdot 9H_2O$ was dissolved in 50 ml of deionized water and both solutions were mixed. After stirring at 55–65 °C for 1 h the complexing agent 1,2-ethanediol or glycerol was added to this solution in the molar ratios 1:1 and

3:1 to the total metal ions. After stirring for one additional hour obtained solutions were evaporated to form gels.

For the preparation of Y–Fe–O gel stoichiometric amount of yttrium oxide was first dissolved in 100 ml of 0.2 M acetic acid. Iron(III) nitrate nonahydrate was dissolved in 75 ml of deionized water and mixed with obtained yttrium acetate solution. The resulting mixture was stirred for 1 h at the same temperature. In the following step, 1,2-ethanediol or glycerol was added to this solution in the molar ratio of 1:1 to the total metal ions.

The synthesized Y–Fe–O and Tb–Fe–O gels were dried in the drying oven (120 °C) for about 24 h. The obtained dry gels were ground to fine powders in an agate mortar, and powders were preheated at 800 °C temperature for 2 h at a heating rate of 10 °C/min. After an intermediate grinding in an agate mortar the powders were additionally sintered at 800, 900 or 1000 °C temperature for 10 h.

Other lanthanide iron garnets were obtained in the same manner as terbium iron garnet using only 1,2-ethanediol as the complexing agent in the molar ratio of 1:1 to the total metal ions.

5.2.4. Synthesis of $Y_3Al_{5-x}Fe_xO_{12}$

$Y_3Al_{5-x}Fe_xO_{12}$ (x = 0, 1.0, 2.0, 2.5, 3.0, 4.0, 5.0) were prepared by the same way as lanthanide iron garnets using stoichiometric amounts of Y_2O_3, $Fe(NO_3)_3 \cdot 9H_2O$ and $Al(NO_3)_3 \cdot 9H_2O$.

For the fabrication of $Y_3Al_{5-x}Fe_xO_{12}$ (x = 0, 3.0, 4.0, 5.0) thin films an aqueous solution of 3% polyvinyl alcohol (PVA) as wetting agent was prepared and added to the precursor Y–Al–Fe–O sol [156]. The volume ratio of the precursor sol and PVA solution was 1:1. Thin $Y_3Al_{5-x}Fe_xO_{12}$ films were deposited on Si substrate (1 1 1) by dip-coating technique using a KSV Dip-coater. Before deposition, the Si substrate was cleaned with acetone and surface was activated with 0.3 mbar oxygen plasma with plasma cleaner (from Diener) for 10 min. The immersion rate used in the dip-coating procedure was 85 mm/min and withdrawal rate was 40 mm/min. These procedures were repeated 5, 15 and 30 times with drying at room temperature for 2–3 h and

heating each layer at 500 °C for 1 h using the heating rate of 1 °C/min. After the final dip-coating the films were heated at 1000 °C for 10 h using the heating rate of 1 °C/min.

5.3. Materials Characterization

5.3.1. Thermal Analysis Measurements

TG/DSC measurements of the precursor gels were carried out under flowing air at a heating rate of 10 °C/min using Simultaneous Thermal analyser STA6000 from PerkinElmer. Around 5–10 mg of powdered samples were analysed using alumina (Al_2O_3) crucible. Coupled TG–GC–MS analysis was used for the determination of the evolved gases at different temperatures. Thermogravimetric analysis (TG, DTG) was performed using Pyris 1 TGA thermal analyser from PerkinElmer and carried out under nitrogen and air flow at a heating rate of 10 °C/min. About 5–10 mg of samples were analysed using platinum crucible. Gas analyses were performed on a PerkinElmer Clarus 600 gas chromatograph using Elite-5MS capillary column (30 m, 0.25 mm) and He as a carrier gas with temperature program: 35 °C for 5 min followed by 10 °C/min heating up to 200 °C for 5 min. Injections of gas sample were done for temperatures corresponding to the most important mass losses on the DTG curve. Gas fractions were gas chromatographically eluted before mass spectroscopic detection. The evolved gases were determined on the basis on their mass spectra. Mass spectrometric analyses were recorded with a quadrupole mass spectrometer. Electron impact (70 eV) mass spectra were recorded from 35 to 350 m/z. A thermogravimetric device with the small magnet was adapted to determine Curie temperature of series of rare earth iron garnets. Measurements were performed from 200 °C to 360 °C with the heating rate of 5 °C/min under flowing nitrogen. Analysis was performed with 10–12 mg of sample using platinum crucible.

5.3.2. Powder X-ray Diffraction

X-ray diffraction (XRD) data were collected using Ni filtered CuK_{α} radiation on Rigaku MiniFlex II diffractometer working in the Bragg–Brentano ($\theta/2\theta$) geometry. The step size and speed was 0.01° and 5°/min, respectively. Some XRD measurements were performed on PANalytical X'Pert PRO diffractometer with secondary monochromator and PIXcel position-sensitive detector using CuK_{α} radiation. Measurements were taken at a step size of 0.026°.

5.3.3. DLS Analysis

Malvern Nano ZS from Malvern Instruments was used for the measurements of particle size distribution.

5.3.4. SEM Analysis

Scanning electron microscopy (SEM) micrographs were obtained by a FE-SEM Hitachi SU-70. Microstructural analysis of glazes was carried out by TM3000 scanning electron microscope.

5.3.5. UV/VIS Spectroscopic Investigations

UV/Vis diffuse reflectance spectra were recorded on a PerkinElmer Lambda 35 UV/Vis spectrophotometer equipped with an integrating sphere accessory and $BaSO_4$ reference.

5.3.6. Determination of Colour Coordinates

The colour of the pigments in powdered form and of the glazes were determined by PerkinElmer Lambda 950 UV/Vis/NIR spectrophotometer with integrating sphere and D_{65} illuminant, at an observer's angle of 10°. *L**, *a** and *b** values were obtained using the CIE *L*a*b** method.

5.3.7. FTIR Measurements

The infrared spectra in the range of 4000–500 cm^{-1} were recorded on PerkinElmer Frontier FT-IR spectrometer.

5.3.8. Mössbauer Spectroscopy

Mössbauer spectra were measured in transmission mode with ^{57}Co diffused into Rh matrix as the source moving with constant acceleration. The spectrometer was calibrated by means of a standard α–Fe foil and the isomer shift was expressed with respect to this standard at 293 K. The samples were measured at the temperature of 293 K. The fitting of the spectra was performed with the help of the NORMOS programme.

5.3.9. Magnetic Hysteresis

The vibrating sample magnetometer was applied for the magnetization measurements. Magnetic data were taken on powders of prepared garnet samples, which were encapsulated into a plastic straw in order to place into the magnetometer. Therein the lock-in amplifier SR510 (Stanford Research Systems) was applied to measure the signal from the sense coils generated by vibrating sample. The gauss/teslameter FH-54 (Magnet Physics) was used to measure the strength of magnetic field between the poles of the laboratory magnet supplied by the power source SM 330-AR-22 (Delta Elektronika).

Chapter 6. Synthesis and Characterization of Commercial and Synthesized Red Iron(III) Oxide Pigments and Glazes

6.1. Characterization of Commercial Red Iron(III) Oxide Pigments

Three different commercial iron(III) oxide pigments purchased from Kremer Pigmente (light red iron(III) oxide, dark red iron(III) oxide and burnt red iron(III) oxide) were initially investigated in this study. The powder XRD patterns of these pigments are shown in Figure 6.1.
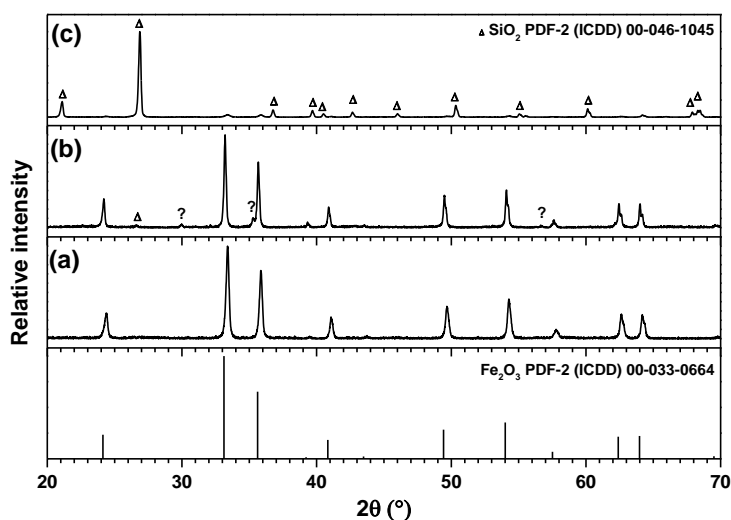
Figure 6.1. XRD patterns of commercial iron(III) oxide pigments: light red iron(III) oxide (a), dark red iron(III) oxide (b) and burnt red iron(III) oxide (c). The vertical lines represent the standard XRD pattern of synthetic hematite.

XRD patterns of light red iron(III) oxide (Figure 6.1a) and dark red iron(III) oxide (Figure 6.1b) match very well with the reference pattern of synthetic hematite. However, dark red iron(III) oxide has slight amount of quartz SiO_2 phase (PDF-2 (ICDD) 00-011-0252) and some unidentified phase. Obviously, the phase composition of the pigment named as burnt red iron(III) oxide differs substantially from previous ones. As seen from the XRD pattern presented in Figure 6.1c, the main peaks could be attributed to the hexagonal quartz SiO_2 phase (PDF-2 (ICDD) 00-011-0252).

The morphology of three commercial pigments was examined using scanning electron microscopy. The SEM micrographs are shown in Figure 6.2. It can be seen that light iron(III) oxide sample (Figure 6.2a) is composed of

37

spherical particles of about 0.1 µm in size. The dark red iron(III) oxide (Figure 6.2b) is composed of plate shape agglomerates with the surface covered by smaller (~0.3 µm) particles. Burnt iron(III) oxide consists of large volumetric particles with the size ranging from 20 to 50 µm. These large particles are constituted of smaller crystalline grains with the size of around 0.05–0.1 µm (Figure 6.2c).
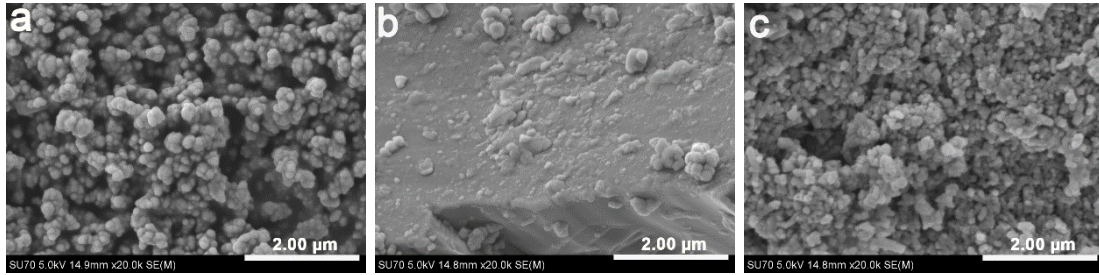
Figure 6.2. SEM micrographs of light red iron(III) oxide (a), dark red iron(III) oxide (b) and burnt red iron(III) oxide (c).

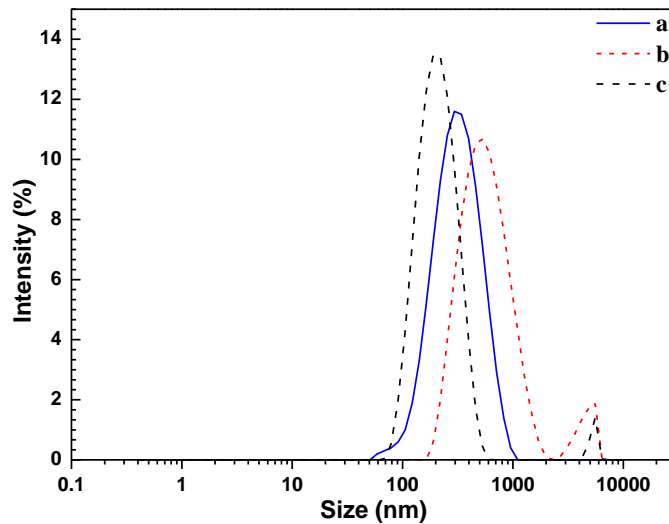Figure 6.3 shows hydrodynamic particle diameter distributions of commercial pigments.

Figure 6.3. Particle size distribution of light red iron(III) oxide (a), dark red iron(III) oxide (b) and burnt red iron(III) oxide (c).

Maximum intensity in the particle size distribution curve is at around 0.3 µm for the light red iron(III) oxide and about 0.6 µm for dark red iron(III)

oxide. Particle size distribution for the burnt red iron(III) oxide is ranging from 0.07 to 0.6 µm with the maximum intensity of 0.21 µm.

Thus, both SEM and DLS methods showed that all three commercial pigments have different particle size. The difference in particle size of light red iron(III) oxide and dark red iron(III) oxide could be the reason that these pigments have slightly different colour. Also, dark red iron(III) oxide has small amount of other phases, which can influence on the colour of the pigment. On the other hand, the different colour of the burnt red iron(III) oxide could be more associated with completely different chemical composition.

6.2. Preparation of Glazes with Commercial Pigment and Optimization of Glaze Preparation Parameters

Light red iron(III) oxide was chosen for the optimization of ceramic glaze preparation conditions. Glazes were fired at 800, 900 and 1000 °C temperatures for 30 or 60 min with the heating rate of 5 °C/min and were dried or not dried before firing. Glaze preparation conditions are given in Table 6.1.

Table 6.1. Preparation conditions of glazes with light red iron(III) oxide.

Glaze	Temperature, °C	Firing time, min	Pigment amount, %	Dried/not dried
a	800	60	5	dried
b	800	60	10	dried
c	800	60	5	not dried
d	800	60	10	not dried
e	900	60	5	not dried
f	900	30	5	dried
g	900	30	5	not dried
h	900	30	5	dried
i	1000	60	5	dried
j	1000	60	10	dried
k	1000	60	5	not dried
l	1000	60	10	not dried

A digital picture of the prepared glazes is presented in Figure 6.4. It could be seen that most important parameters in the preparation of light red iron(III)

oxide containing ceramic glaze are firing temperature of glaze and amount of pigment. All glazes which have been prepared with larger amount of pigment (10 wt.%) have blisters on the surface (see Figure 6.4b, d, j, l). Moreover, the glazes are not solid. Obviously, the quality of the glazes fired at 900 °C (see Figure 6.4e–h) is not the best. On the other hand, glazes prepared at 1000 °C temperature with the smaller amount of pigment (5 wt.%) have red/violet shade (see Figure 6.4i, k). Further obtained glazes were fired at 800, 900 and 1000 °C for 60 min with the 5 wt.% of the pigment.
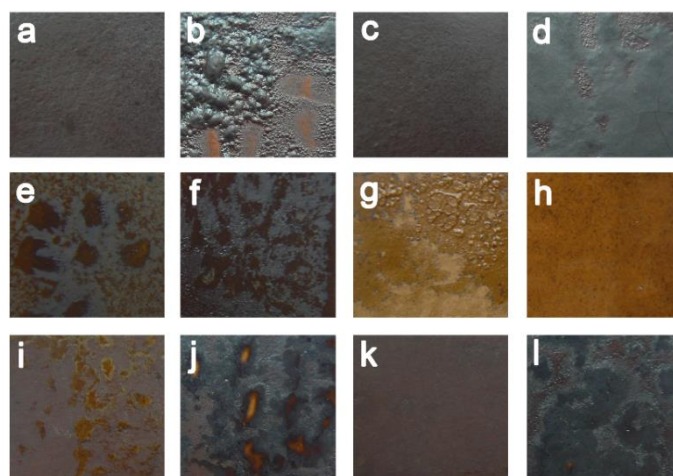
Figure 6.4. Images of the glazes prepared with light iron(III) oxide.

6.3. Synthesis and Characterization of Historical Hematite Pigment by an Aqueous Sol-Gel Method

The ceramic Fe_2O_3 pigments were synthesized by simple and environmentally benign aqueous sol-gel method. The thermal decomposition of Fe–O precursor gel was studied from room temperature up to 1000 °C. TG/DTG/DSC curves of the Fe–O precursor gel are shown in Figure 6.5.

From Figure 6.5 we can state that there are two stages of mass loss on the TG curve. The first step up to 150 °C (DTG peak at 78 °C) of mass loss of about 6% is related to the evolution of adsorbed water. This is in good agreement with DSC curve, which shows slight endothermic process in this temperature range. The second mass loss step (around 45%) is observed in the temperature range of 150–325 °C and can be assigned to the thermal decomposition of organic

40

complexes of iron and burning of organic residues. This step is accompanied by the strong exothermic signals in DSC curve peaked at 244 °C and 263 °C. No more mass losses are observed above 350 °C.
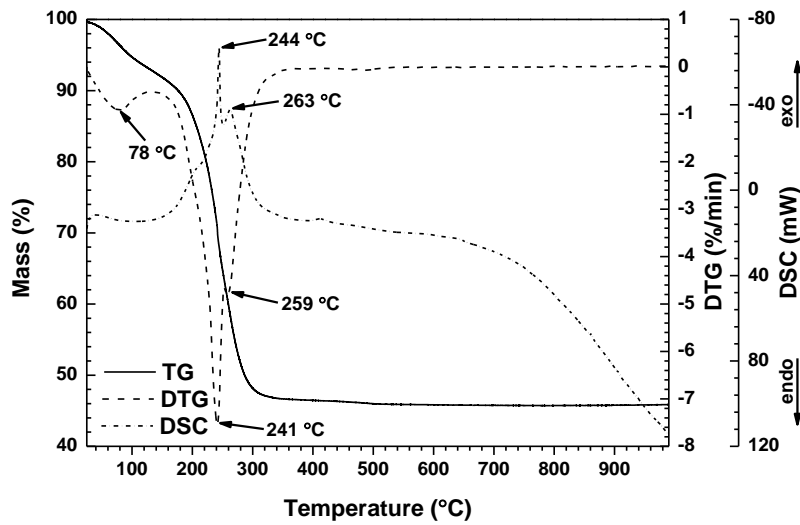
Figure 6.5. TG/DTG/DSC curves of the Fe–O precursor gel.

The powder XRD patterns of Fe–O gels heated at different temperatures are presented in Figure 6.6.
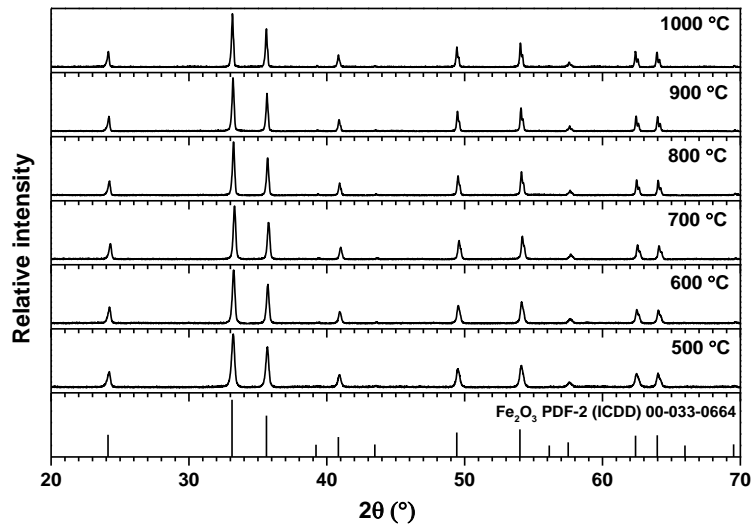

Figure 6.6. Powder XRD patterns of Fe–O gels, heat-treated at various temperatures for 10 h. Vertical lines represent standard XRD pattern of synthetic hematite.

The reference XRD pattern of Fe_2O_3 (PDF-2 (ICDD) 00-033-0664) was also added for comparison. Evidently, annealing the gels at different

41

temperatures in the range of 500–1000 °C yielded the same single phase synthetic hematite. Thus, the monophasic Fe_2O_3 powders using sol-gel chemistry approach could be obtained already at 500 °C, which is rather low temperature for the preparation of such type compounds.

The morphological features of sol-gel derived Fe_2O_3 pigments are shown in the SEM micrographs presented in Figure 6.7. It is obvious that particle size of synthesized Fe_2O_3 increases with increasing annealing temperature. Moreover, the particle shape changes from spherical to plate-like by increasing the temperature. The pigments synthesized at 500 and 600 °C are obtained with particle size of around 0.2 µm (Figure 6.7a, b). As shown in Figure 6.7c, d, the microstructure of pigments annealed at 700 and 800 °C has changed slightly. The particles are irregularly shaped with a particle size distribution ranging from 0.2 to 0.5 µm, while increasing annealing temperature to 900 °C causes the particle size distribution from 0.4 to 1 µm (Figure 6.7e). Figure 6.7f demonstrates that pigment obtained at 1000 °C has network microstructure with the plate-like crystals up to 3 µm in size.
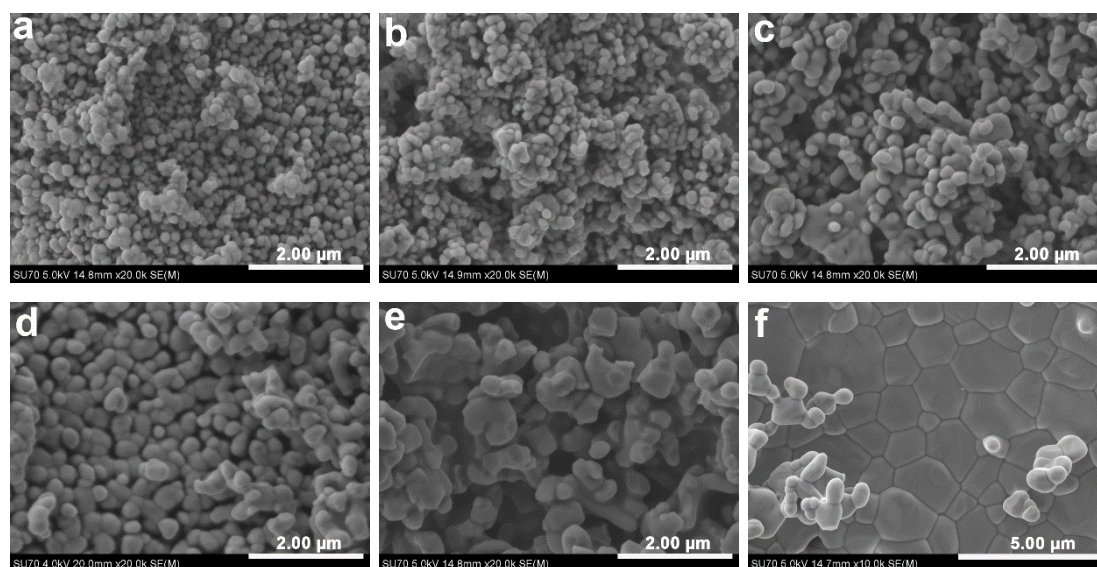

Figure 6.7. SEM micrographs of Fe_2O_3 obtained at different temperatures 500 °C (a), 600 °C (b), 700 °C (c), 800 °C (d), 900 °C (e) and 1000 °C (f).

Figure 6.8 illustrates diffuse reflectance spectra and colour of powdered Fe_2O_3 samples prepared at different temperatures. Synthesized pigments show

broad absorption band located between 400 and 600 nm (Figure 6.8, region 1). Absorption band in this region visibly shifts to the longer wavelength by increasing pigment annealing temperature. As was mentioned before, Fe^{3+} substances exhibit a colour that is mainly a function of the electronic transitions: ligand field (or *d-d*) transitions, $2p(O^{2-}) \rightarrow 3d(Fe^{3+})$ charge transfer, and pair excitations resulting from simultaneous excitation of two adjacent Fe^{3+} ions that are magnetically coupled [53, 55]. Absorption band in region 1 (400–600 nm) is assigned to the pair excitation process $^6A_1$ (^6S) + $^6A_1$ (^6S) to $^4T_1$ (^4G) + $^4T_1$ (^4G) at 485–550 nm of a Fe^{3+}–Fe^{3+} pair, probably overlapped by the contributions of $^6A_1$ (^6S) to ^4E, $^4A_1$ (^4G) *d-d* transitions at 430 nm and the charge transfer transition band tail. Region 2 (600–750 nm) in Figure 6.8 corresponds to the $^6A_1$ (^6S) to $^4T_2$ (^4G) *d-d* transitions at ~640 nm, while the region 3 (750–900 nm) is the $^6A_1$ (^6S) to $^4T_1$ *d-d* transitions at ~900 nm [52, 53]. On the other hand, some authors claim, that dark red coloration of hematite is mainly due to $2p(O^{2-}) \rightarrow 3d(Fe^{3+})$ charge transfer bands [46].
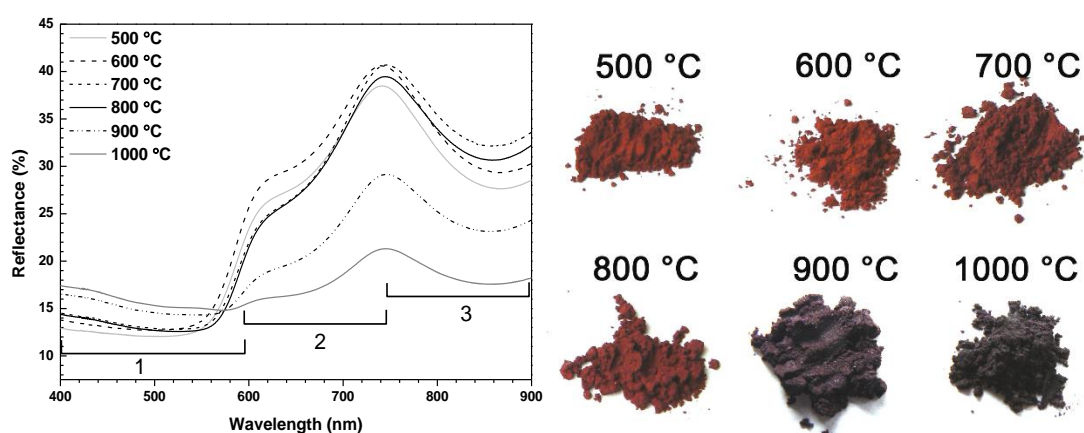
Figure 6.8. Diffuse reflectance spectra and colour of hematite pigments synthesized at different temperatures.

The synthesized pigments absorb in the green and yellow regions and as complementary they display visible from red to violet colour (Figure 6.8). The CIE *L**, *a** and *b** values of synthesized pigments are presented in Table 6.2. The table shows that colour lightness *L** parameter and red predominance *a** parameter decreases as synthesis temperature reaches 900 °C and 1000 °C.

Table 6.2. CIE *L**, *a**, *b** values of pigments heated at different temperatures.

Red ochre annealing temperature	*L**	*a**	*b**
500 °C	46.88	14.63	8.89
600 °C	47.78	15.85	9.51
700 °C	46.07	12.95	5.48
800 °C	46.10	13.87	5.53
900 °C	45.51	5.62	0.64
1000 °C	44.48	2.06	-1.10

Pigments prepared at lower temperatures demonstrate higher values of parameter *a**, characteristic for the red shade [9]. These results confirm, that choosing higher annealing temperature of the gel, we could get darker colour of pigment.

6.4. Preparation of Glazes with Synthesized Historical Hematite Pigment

Synthesized hematite pigments were used for the preparation of ceramic glazes. Table 6.3 presents glaze marking and pigment used for the preparation of ceramic glazes shown in Figures 6.9–6.11.

Table 6.3. Pigments used for the preparation of glazes (Figures 6.9–6.11).

Glaze	Pigment
a	Light red iron(III) oxide
b	Dark red iron(III) oxide
c	Burnt red iron(III) oxide
d	Red ochre annealed at 500 °C
e	Red ochre annealed at 600 °C
f	Red ochre annealed at 700 °C
g	Red ochre annealed at 800 °C
h	Red ochre annealed at 900 °C
i	Red ochre annealed at 1000 °C

Obviously, the surface of some glazes fired at 800 °C has blisters on the top (Figure 6.9a, f) and colour of most samples is dark violet. Contrary, ceramic glazes prepared at 900 °C reveal lighter colours (Figure 6.10). The surfaces of all samples are heterogeneous. The best quality glazes were obtained at 1000 °C

temperature showing uniform glaze top and red/violet shade. All samples with the burnt red iron(III) oxide are characterized by yellow colour (Figure 6.9c, Figure 6.10c, Figure 6.11c). From X-ray diffraction it is obvious that hexagonal quartz SiO_2 phase dominate in the composition of this pigment. It is evident that this phase is responsible for different colour of glaze.

Moreover, the glazed terracotta samples without pigment do not show red shade (Figure 6.12). Thus, it can be concluded that the starting pigment is very important parameter for the preparation of high quality ceramic glaze. Additionally, the quality of red iron(III) oxide glazes also depends very much on firing temperature.
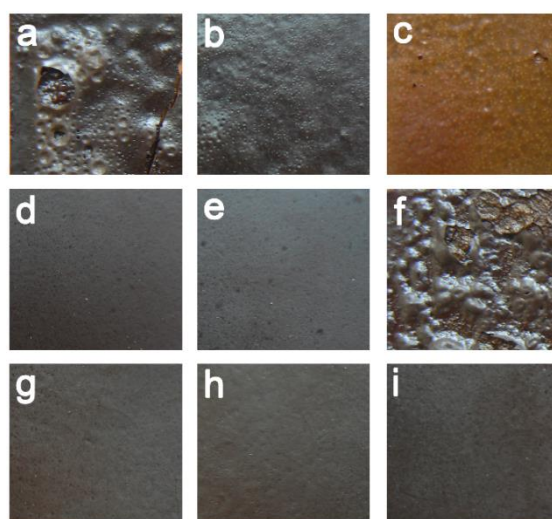
Figure 6.9. Images of glazes fired at 800 °C with different pigments.
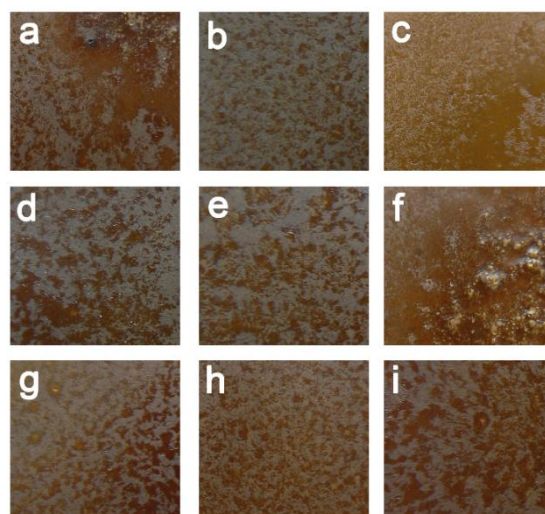
Figure 6.10. Images of glazes fired at 900 °C with different pigments.
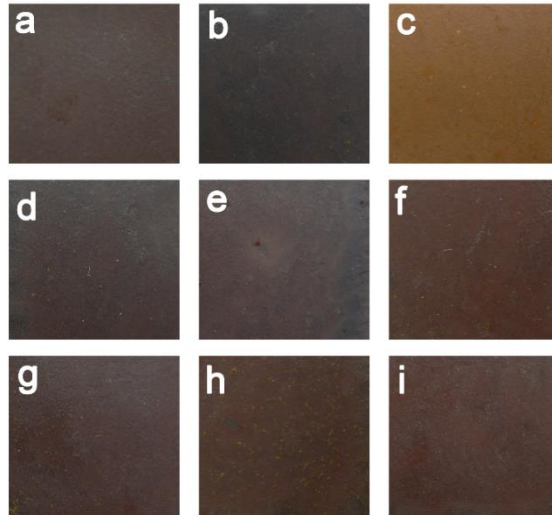
Figure 6.11. Images of glazes fired at 1000 °C with different pigments.
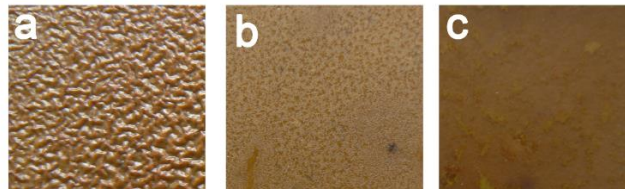
Figure 6.12. Images of glazes fired at 800 °C (a), 900 °C (b) and 1000 °C (c) without pigment.

Finally, the colour coordinates for the best quality glazes fired at 1000 °C were determined as well. Table 6.4 shows the CIE L^*, a^*, b^* values of these glazes.

Table 6.4. CIE L^*, a^* and b^* values of glazes fired at 1000 °C.

Pigment used for glaze	L^*	a^*	b^*
Light red iron(III) oxide	35.13	7.85	4.53
Dark red iron(III) oxide	35.44	7.16	3.89
Burnt iron(III) oxide	45.16	13.87	17.82
Red ochre annealed at 500 °C	35.56	7.73	4.10
Red ochre annealed at 600 °C	36.38	8.94	4.99
Red ochre annealed at 700 °C	35.40	8.46	4.93
Red ochre annealed at 800 °C	35.02	8.30	4.78
Red ochre annealed at 900 °C	33.37	7.50	4.78
Red ochre annealed at 1000 °C	34.22	8.35	4.91
Without pigment	45.60	13.42	22.08

It could be seen that all the samples except prepared with burnt iron(III) oxide and sample without pigment have higher parameter a^* values than b^*. Besides, independent on pigment all samples have similar L^*, a^* and b^* values. These results confirm that all used pigments show similar colour when used for ceramic glaze. Contrary, glazes with burnt iron(III) oxide and glaze without pigment have higher b^* value, which shows yellow colour of glazes.

Chapter 7. Sol-Gel Synthesis and Characterization of $Ln_3Fe_5O_{12}$ and $LnFeO_3$ (Ln = Ce, Pr, Nd, Tb) and Glazes

In this chapter, the results of sol-gel synthesis of $Ln_3Fe_5O_{12}$ and $LnFeO_3$ (Ln = Ce, Pr, Nd, Tb) are presented. To the best of our knowledge, lanthanide iron garnets have not been used as ceramic pigments.

7.1. Sol-Gel Synthesis and Characterization of $Ln_3Fe_5O_{12}$ and $LnFeO_3$ (Ln = Ce, Pr, Nd, Tb)

Powder X-ray diffraction patterns of Nd–Fe–O (P1), 3Nd–5Fe–O (P2), Tb–Fe–O (P3), 3Tb–5Fe–O (P4), Pr–Fe–O (P5), 3Pr–5Fe–O (P6), Ce–Fe–O (P7) and 3Ce–5Fe–O (P8) gels sintered at 1000 °C for 10 h in air are given in Figure 7.1.

Phase composition analysis reveals that most samples are not single phase compounds. Samples P1 and P2 are composed of mixture of $NdFeO_3$ and Fe_2O_3 crystalline phases. Obviously, the higher amount of undesirable Fe_2O_3 phase has formed during the attempted synthesis of $Nd_3Fe_5O_{12}$ garnet.

Since, $Nd_3Fe_5O_{12}$ phase has not formed at 1000 °C, different annealing temperatures of 3Nd–5Fe–O gel were used to access the desired garnet phase. Figure 7.2 shows the XRD patterns of 3Nd–5Fe–O gels sintered at various temperatures. The XRD patterns presented in Figure 7.2 reveals that the synthesis products are obtained as biphasic systems at all chosen sintering temperatures. The phase composition of all products consists of $NdFeO_3$ and Fe_2O_3 oxides.
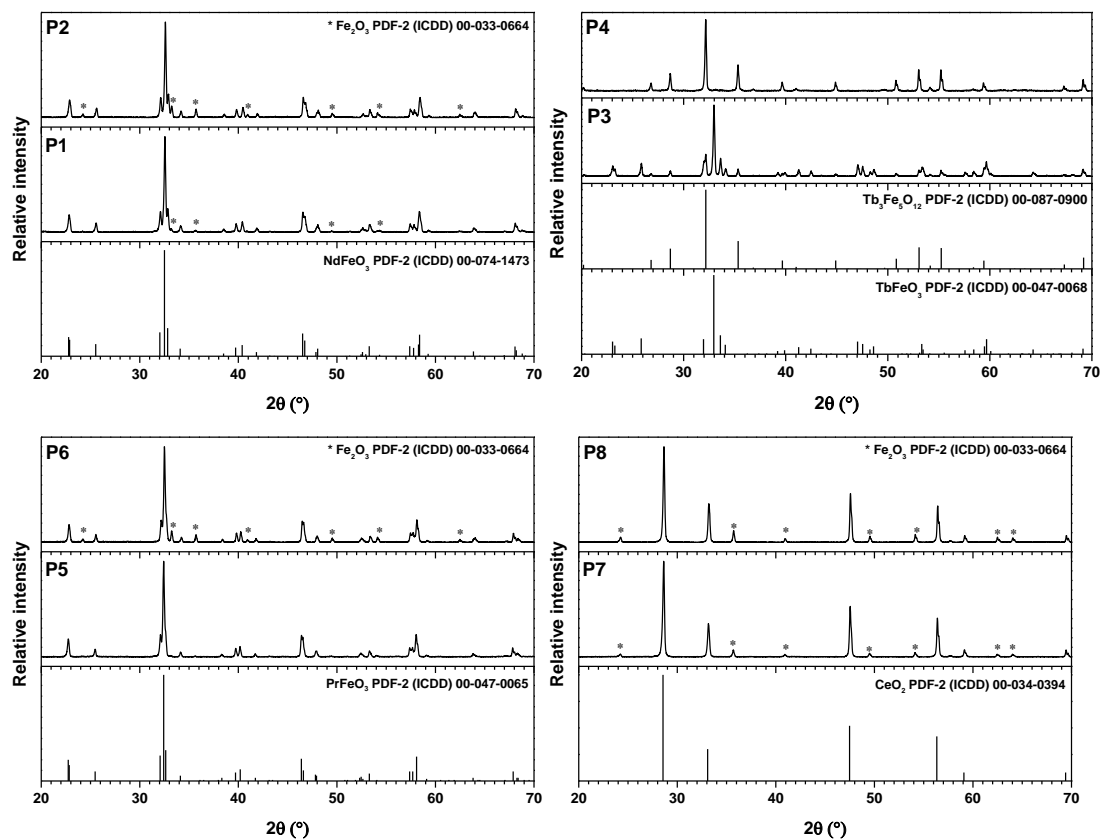
Figure 7.1. Powder XRD patterns of Nd–Fe–O (P1), 3Nd–5Fe–O (P2), Tb–Fe–O (P3), 3Tb–5Fe–O (P4), Pr–Fe–O (P5), 3Pr–5Fe–O (P6), Ce–Fe–O (P7) and 3Ce–5Fe–O (P8) gels annealed at 1000 °C. Vertical lines represent standard XRD patterns.
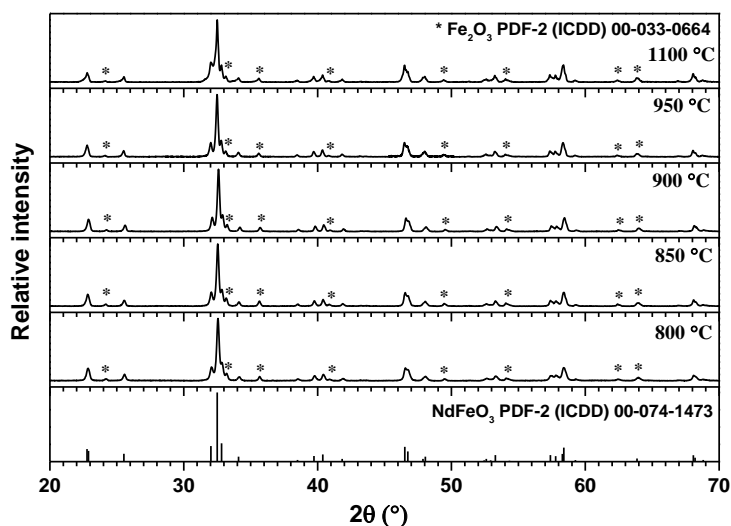

Figure 7.2. Powder XRD patterns of 3Nd–5Fe–O gels annealed at various temperatures. Vertical lines represent standard XRD pattern of NdFeO₃.

48

According to the XRD pattern of Tb–Fe–O gel sintered at 1000 °C (Figure 7.1, sample P3), the formation of $TbFeO_3$ and $Tb_3Fe_5O_{12}$ crystalline phase proceeds instead of the desirable perovskite $TbFeO_3$ ferrite. As seen from Figure 7.1 of sample P4, the single phase $Tb_3Fe_5O_{12}$ garnet has formed under the same synthesis conditions.

The powder XRD analysis revealed that single phase $PrFeO_3$ was obtained by annealing Pr–Fe–O gel at 1000 °C (see Figure 7.1, sample P5). All of the diffraction peaks detected in the XRD pattern coincide with reflections from the standard XRD pattern of $PrFeO_3$. However, in the XRD pattern of sample P6 can be seen that perovskite $PrFeO_3$ ferrite as predominant crystalline phase has formed during the synthesis of expected $Pr_3Fe_5O_{12}$ garnet phase. Besides, the peaks attributable to the Fe_2O_3 as side phase could be also detected in the XRD pattern.

It is evident from the X-ray diffraction pattern of samples P7 and P8 presented in Figure 7.1 that the sol-gel synthesis of $CeFeO_3$ and $Ce_3Fe_5O_{12}$ compounds leads to the formation of mixtures of two CeO_2 and Fe_2O_3 oxides.

Thus, X-ray diffraction analysis results demonstrate that most of prepared iron-based lanthanide mixed-metal oxides are not single phase compounds (Table 7.1). In the pigmentary field, however, it is not always necessary to obtain single-phase system, but the conditions of the synthesis have to be appropriate for the industrial utilization [20].

Table 7.1. Phase composition of prepared pigments.

Sample	Expected composition	Identified phases in pigments
P1	$NdFeO_3$	$NdFeO_3$ and Fe_2O_3
P2	$Nd_3Fe_5O_{12}$	$3NdFeO_3$ and Fe_2O_3
P3	$TbFeO_3$	$TbFeO_3$ and $Tb_3Fe_5O_{12}$
P4	$Tb_3Fe_5O_{12}$	$Tb_3Fe_5O_{12}$
P5	$PrFeO_3$	$PrFeO_3$
P6	$Pr_3Fe_5O_{12}$	$3PrFeO_3$ and Fe_2O_3
P7	$CeFeO_3$	CeO_2 and Fe_2O_3
P8	$Ce_3Fe_5O_{12}$	CeO_2 and Fe_2O_3

The morphological features of the obtained pigments are shown in the SEM micrographs presented in Figure 7.3.
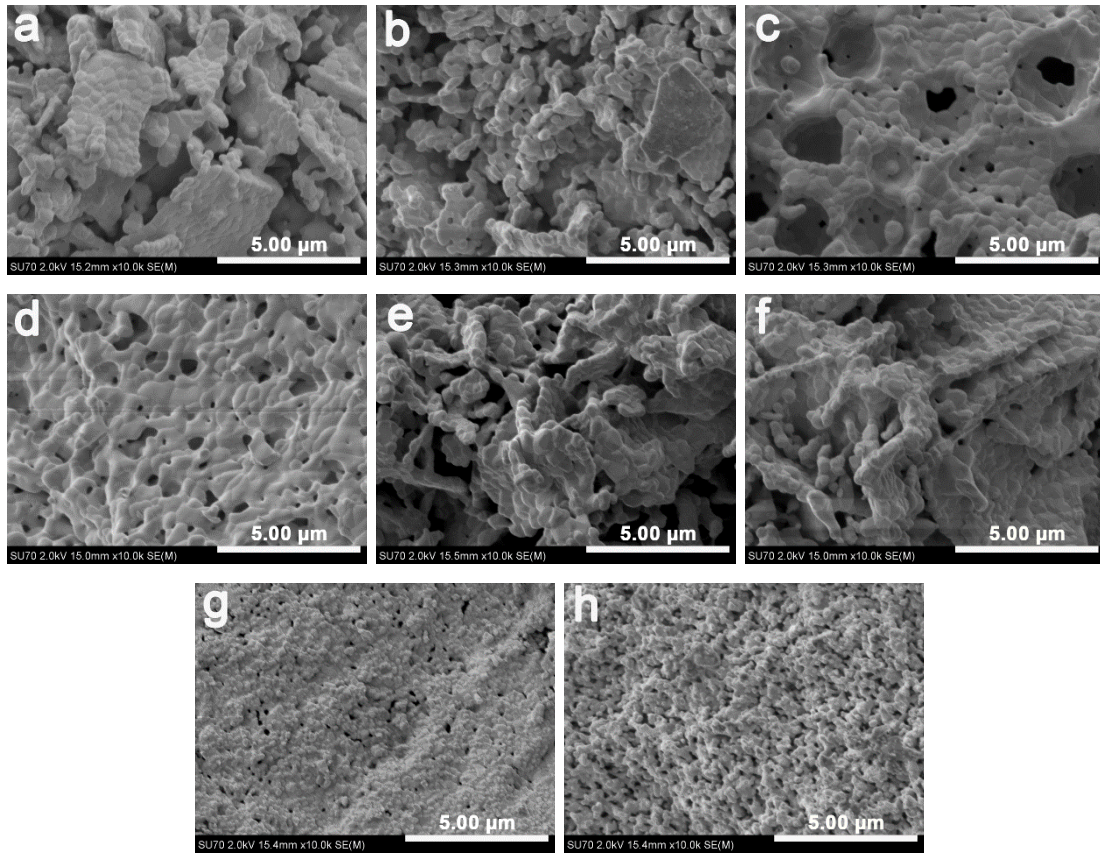
Figure 7.3. SEM micrographs of Nd–Fe–O (a), 3Nd–5Fe–O (b), Tb–Fe–O (c), 3Tb–5Fe–O (d), Pr–Fe–O (e), 3Pr–5Fe–O (f), Ce–Fe–O (g), and 3Ce–5Fe–O (h) gels annealed at 1000 °C.

Figure 7.3a, b demonstrates a very similar surface structure of the pigments, which contain neodymium in their chemical composition. Both Nd–Fe–O and 3Nd–5Fe–O gels annealed at 1000 °C consist of agglomerated spherical sub-microsized particles ~0.5 µm. These spherical particles form plate shaped agglomerates having different size. The SEM micrographs of Tb–Fe–O and 3Tb–5Fe–O gels sintered at 1000 °C are shown in Figure 7.3c, d, respectively. It can be seen that single phase $Tb_3Fe_5O_{12}$ solids are composed of spherical grains 0.5 µm in size. Considerably fewer particles coarsening can be clearly seen in the SEM micrograph of 3Tb–5Fe–O gel sintered at 1000 °C. But the coarsened phase has a tendency to grow into a spherical shape. It is

interesting to note, however, that the particle size does not depend on the phase composition of the end product. The SEM micrographs of different quantitative composition Pr–Fe–O gels annealed at 1000 °C are shown in Figure 7.3e, f. The microstructure of these samples is very similar to the microstructure of neodymium ferrites, whereas plate shape agglomerates of the synthesized products consist of irregular shape particles as well. However, completely different surface morphology was observed for the cerium containing products (see Figure 7.3g, h). The products from both syntheses consist of small about 100–200 nm size particles. The spherically shaped particles coexist with grains slightly bonded to each other, implying that grain growth takes place at this temperature.

7.2. Preparation and Characterization of Glazes with Synthesized $Ln_3Fe_5O_{12}$ and $LnFeO_3$ (Ln = Ce, Pr, Nd, Tb) Pigments

All synthesized lanthanide-ferrite pigments were used for the preparation of ceramic glazes. The CIE L^*, a^*, b^* parameters of prepared pigment samples and appropriate glazes are summarized in Table 7.2.

Table 7.2. CIE L^*, a^* and b^* parameters of pigments and glazes.

Sample	Pigment			Glaze		
	L^*	a^*	b^*	L^*	a^*	b^*
P1	50.12	15.56	12.37	38.35	7.94	6.03
P2	47.57	12.39	9.09	38.80	8.24	4.59
P3	50.90	10.40	11.76	40.90	11.54	8.94
P4	50.92	6.71	11.38	39.89	11.82	8.60
P5	50.85	15.66	14.58	39.77	10.85	9.19
P6	47.14	10.17	6.78	38.92	12.48	11.28
P7	45.90	10.95	3.56	58.35	4.22	17.47
P8	45.32	10.53	2.98	53.37	5.20	15.99
Without pigment	-	-	-	45.60	13.42	22.08

Obviously, all prepared glazes, except those obtained with cerium pigments, are darker than the pigment itself. The highest values of parameters

a* and *b** have pigments P1 and P5, i. e. the Nd–Fe–O and Pr–Fe–O samples heated at 1000 °C. Despite the fact, that pigment P1 has slight impurities of synthetic hematite, both P1 and P5 pigments have a perovskite type structure. Pigment P4 (3Tb–5Fe–O) has the lowest value of the *a** parameter, which is single phase terbium iron garnet. The value of parameter *b** obtained for cerium-containing glazes increased dramatically in comparison with pure pigments, since the surface morphology of glazes is not homogeneous, and separate parts of the glazes have pale yellow areas (see Figure 7.4). Moreover, these glazes have the lowest value of parameter *a**. The values of parameter *a** for other glazes, except for glazes with neodymium, are rather similar independent of the composition of the pigment.

It is evident, that the best quality glaze (P4) was obtained using single phase $Tb_3Fe_5O_{12}$ garnet structure pigment. The surface of this glaze is uniform and reveals a red/brown shade. The worst quality glazes (P7 and P8) were obtained with the pigments containing cerium in their composition. As seen, the separate parts of surface of glazes are covered with pale yellow coloured areas.
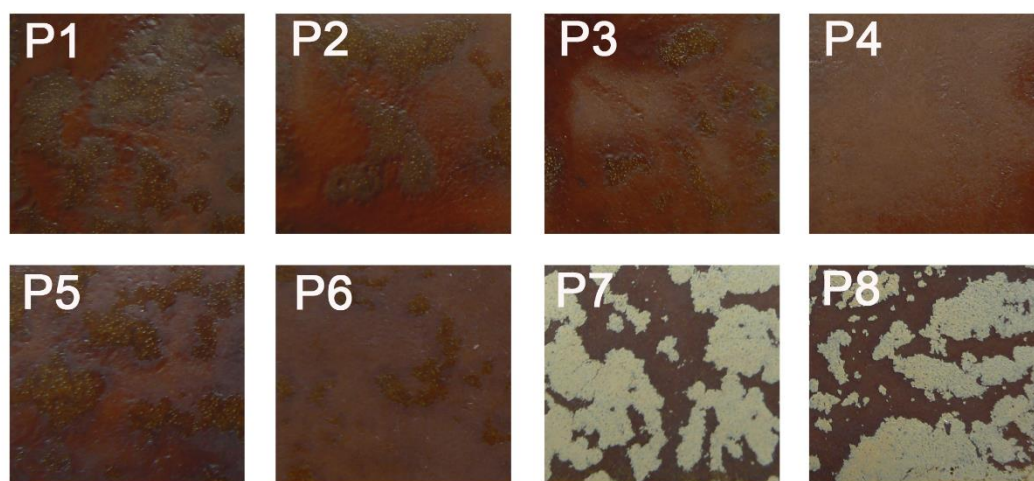
Figure 7.4. Photographs of glazes prepared with iron and lanthanide containing oxide pigments P1–P8.

The SEM micrographs of two representative glazes having opposite quality are shown in Figure 7.5. The microstructural differences could be easily detected for these two glazes as well. The SEM micrograph of glaze P4 shows that small

needle-like particles are evenly distributed over the whole surface of the glaze. However, the huge part of the surface of glaze obtained with cerium pigment is composed of different size irregularly shaped particles.
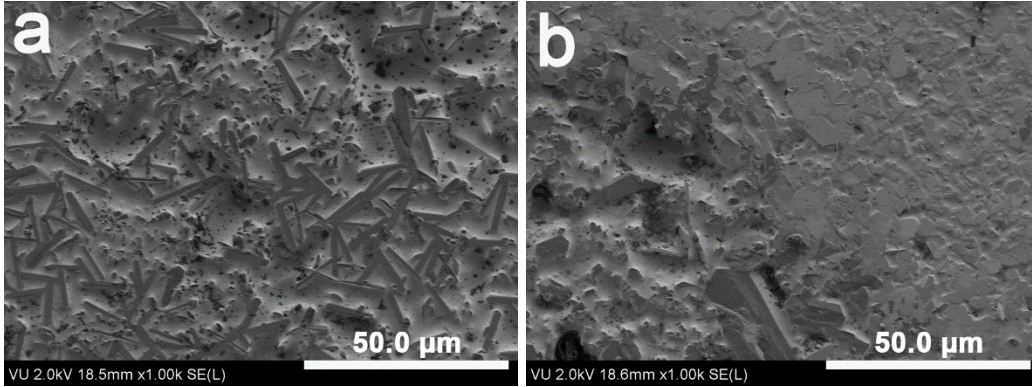
Figure 7.5. SEM micrographs of glazes prepared with $Tb_3Fe_5O_{12}$ (a) and CeO_2 and Fe_2O_3 (b) pigments.

Chapter 8. Optimization of Synthesis Parameters of Lanthanide Iron Garnets

8.1. Preparation and Characterization of $Tb_3Fe_5O_{12}$

Previously prepared terbium iron garnet was chosen for the optimization of synthesis parameters for other lanthanide iron garnets. Samples were prepared by the aqueous sol-gel processing using two different complexing agents. Moreover, different molar ratio of complexing agent to the total metal ions as additional parameter of processing has been evaluated. TG, DTG and DSC curves of Tb–Fe–O precursor gels are depicted in Figures 8.1 and 8.2.
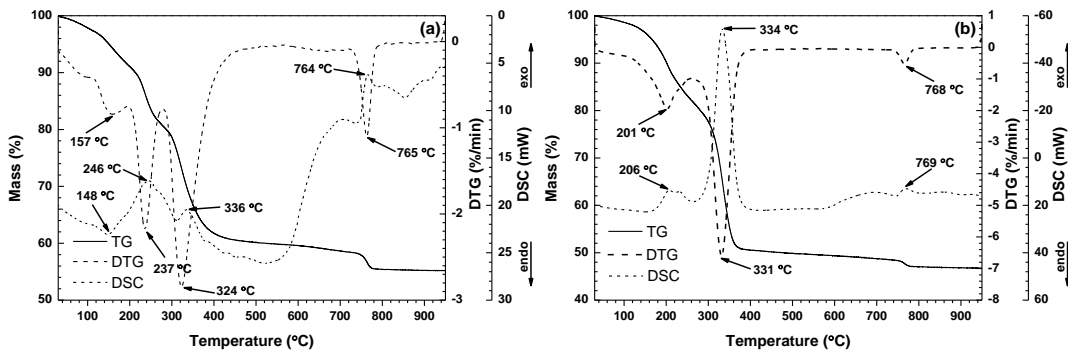
Figure 8.1. TG/DTG/DSC curves of the Tb–Fe–O precursor gels synthesized with 1,2-ethanediol (EG) as a complexing agent in the molar ratios of 1:1 (a) and 3:1 (b) to the total metal ions.
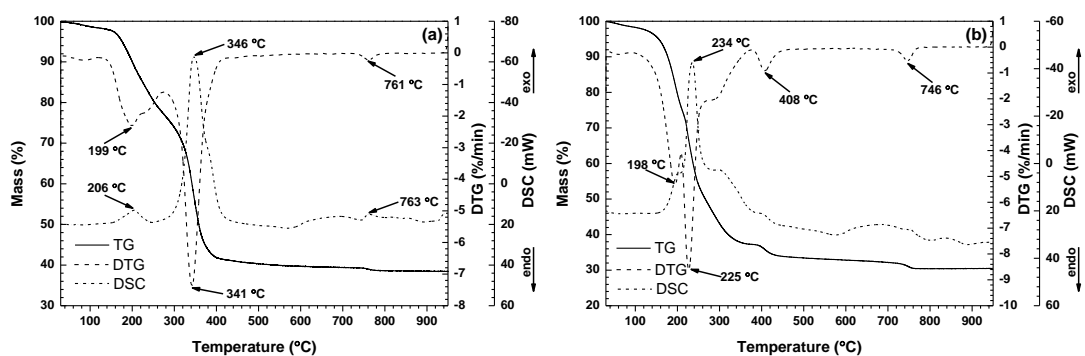
Figure 8.2. TG/DTG/DSC curves of the Tb–Fe–O precursor gel synthesized with glycerol (GL) as a complexing agent in the molar ratios of 1:1 (a) and 3:1 (b) to the total metal ions.

Thermal analysis of both complexing agents and iron(III) nitrate nonahydrate have been also performed (Figure 8.3) in order to see if some starting materials remain in the final gels.
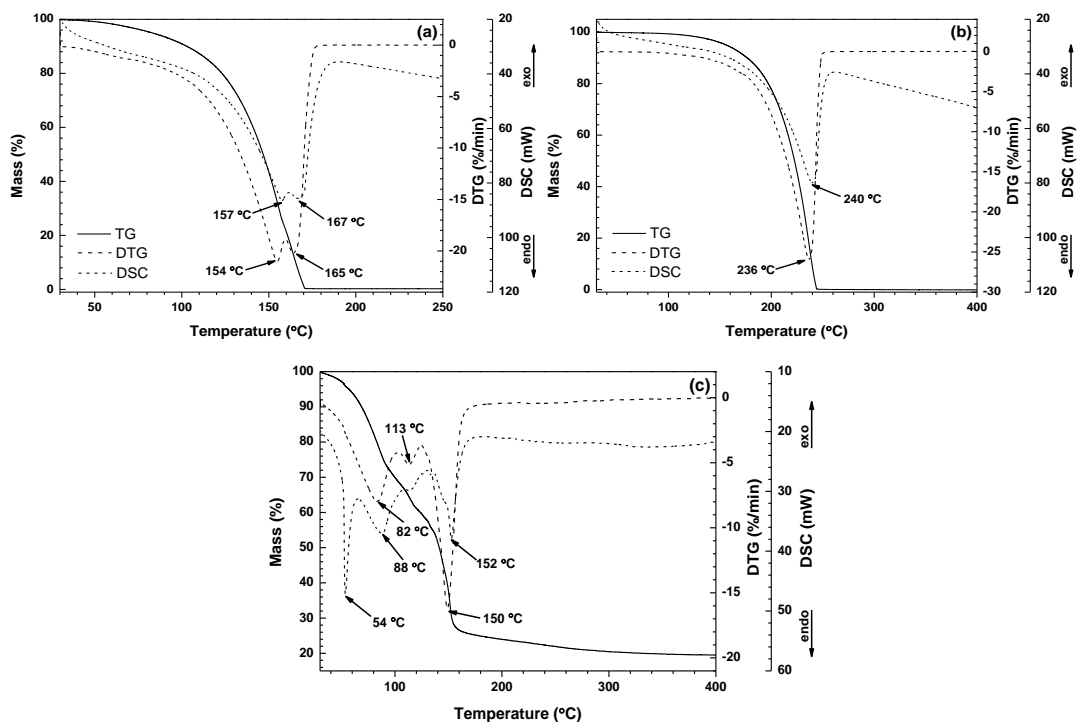
Figure 8.3. TG/DTG/DSC curves of the 1,2-ethanediol (a), glycerol (b) and iron(III) nitrate nonahydrate (c).

As seen from Figure 8.1, the amount of complexing agent used in the sol-gel processing influenced thermal decomposition mechanism of Tb–Fe–O

precursor gel. In both cases two exotherms observed in DSC curves in the temperature range from 200 °C to 450 °C can be related to the main thermal decomposition step of formed complexes during gelation, as weight loss around 325 °C is considered as loss of coordinated ethylene glycol [157]. However, when molar ratio of complexing agent and metals was 3:1, the mass loss range of main decomposition is significantly narrower evidencing less homogeneity of gel [158]. In both cases the last mass loss step could be associated with final decarbonation process and formation of mixed-metal oxide phases [159]. In Figure 8.2 TG, DTG and DSC curves of Tb–Fe–O precursor gels synthesized with glycerol are presented. As can be seen, smaller amount of glycerol (see Figure 8.2a) leads to higher decomposition temperature, showing the formation of more stable complex. On the other hand, the main mass loss step at 225 °C seen in Figure 8.2b could be related to the residual of some unreacted glycerol, which shows very close decomposition and evaporation temperature (Figure 8.3b). Again, thermal decomposition mechanism of glycerate Tb–Fe–O gel is clearly dependent on the amount of complexing agent used during preparation of gels.

XRD patterns of TbIG compounds are shown in Figures 8.4 and 8.5.

Figure 8.4. XRD patterns of Tb–Fe–O gels synthesized with glycerol and 1,2-ethanediol in the molar ratios of 1:1 and 3:1, and heated at 1000 °C (a) and 900 °C (b) for 10 h. Vertical lines represent standard XRD pattern of $Tb_3Fe_5O_{12}$.

Obviously, XRD patterns of the Tb–Fe–O precursor gels heat-treated at 1000 °C (Figure 8.4a) show that only single phase TbIG garnet has formed independently on the nature and amount of complexing agent.

The XRD patterns of Tb–Fe–O gels synthesized with glycerol and 1,2-ethanediol in the molar ratios of 1:1 and 3:1, and heated at 900 °C for 10 h are presented in Figure 8.4b. From these results it is clearly seen that by changing synthesis temperature to 900 °C the amount of complexing agent influences the formation of final product significantly. Higher amount of ethylene glycol or glycerol does not promote the formation of main $Tb_3Fe_5O_{12}$ garnet phase. The additional reflections corresponding to the side Fe_2O_3 phase are seen in these XRD patterns. While during the sol-gel synthesis with lower amount of complexing agent the monophasic $Tb_3Fe_5O_{12}$ garnet has formed. In conformity with the results obtained from XRD measurements of products annealed at 1000 °C and 900 °C, only Tb–Fe–O gels prepared with the molar ratio of metal and complexing agents = 1:1 have been sintered at 800 °C temperature. The XRD patterns of Tb–Fe–O gels synthesized with glycerol and 1,2-ethanediol in the molar ratios of 1:1 and heated at 800 °C for 10 h are presented in Figure 8.5.
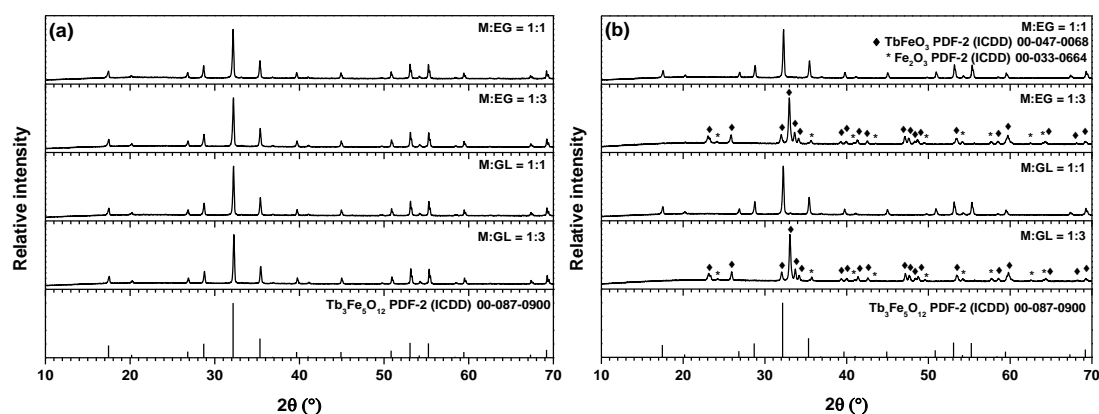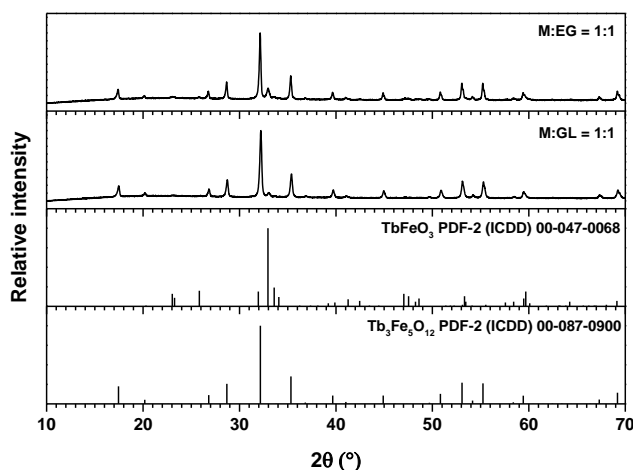

Figure 8.5. XRD patterns of Tb–Fe–O gels synthesized with glycerol and 1,2-ethanediol in the molar ratio of 1:1 and heated at 800 °C for 10 h. Vertical lines represent standard XRD patterns of $TbFeO_3$ and $Tb_3Fe_5O_{12}$.

As seen, in both synthesis routes the formed dominant phase remains $Tb_3Fe_5O_{12}$, however, the small amount of side $TbFeO_3$ phase also formed. On

the other hand, the glycolate sol-gel synthesis route is preferable, since only traces of perovskite phase could be determined in the end product. Developed glycolate sol-gel synthesis route allows us to prepare TbIG at 800 °C.

The microstructure of prepared TbIG compounds is depicted in SEM micrographs shown in Figures 8.6–8.8. Figure 8.6 shows the surface features of the Tb–Fe–O gel powders calcined at 1000 °C. As can be seen, the microstructure of $Tb_3Fe_5O_{12}$ prepared with molar ratio of metal cation to complexing agent 1:3 is very similar using both 1,2-ethanediol and glycerol in the sol-gel synthesis. The solids are composed of elongated particles with less than 500 nm in size. The surface morphology of TbIG samples obtained using molar ratio of 1:1 is slightly different. Apparently, the particles were formed with more pronounced agglomeration, indicating good connectivity between the grains.

Figure 8.6. SEM micrographs of TbIG prepared with 1,2-ethanediol (M:EG = 1:3 (a), 1:1 (b)) and glycerol (M:GL = 1:3 (c), 1:1 (d)) and annealed at 1000 °C.

Obviously, the particle size of terbium iron garnets fabricated using lower sintering temperature is significantly smaller; however, independently on the annealing temperature particles are highly agglomerated. The samples synthesized from the gels with molar ratio of metal cation to complexing agent 1:3 at 900 °C are composed of spherical particles less than 350 nm in size (Figure 8.7). However, the XRD measurements revealed that from the Tb–Fe–O gels, annealed at 900 °C with M:EG and M:GL = 1:3 perovskite type terbium ferrite has formed. The microstructure of TbIG oxide ceramic samples, which were obtained using molar ratio of 1:1 at 900 °C, consisted of a large-grained matrix with clusters of small grains. The phenomena of clustering and texture in the similar samples were addressed in another publication [160, 161].
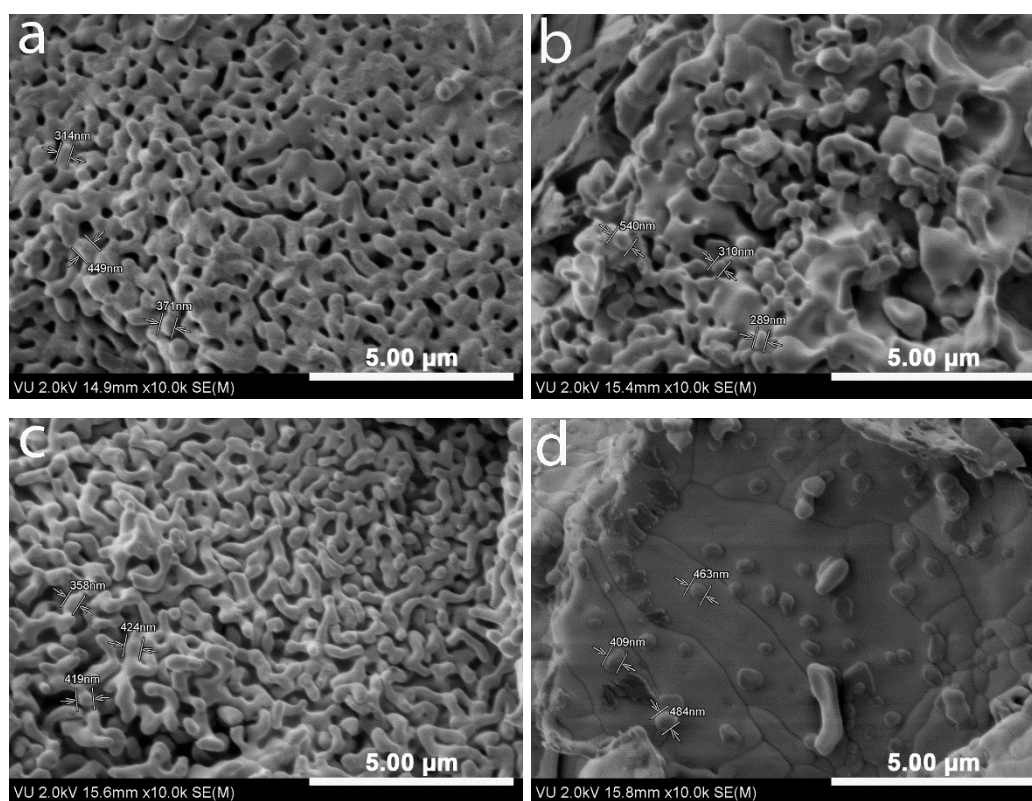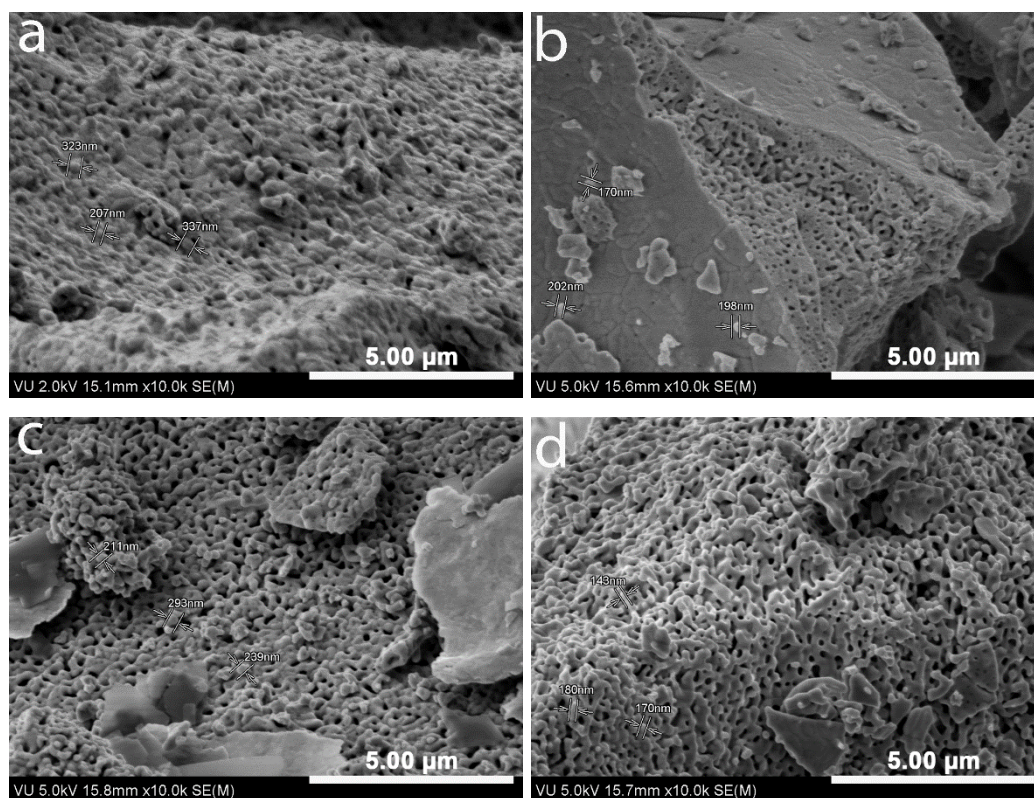

Figure 8.7. SEM micrographs of TbIG prepared with 1,2-ethanediol (M:EG = 1:3 (a), 1:1 (b)) and glycerol (M:GL = 1:3 (c), 1:1 (d)) and annealed at 900 °C.

Figure 8.8 shows the surface features of the TbIG powdered samples synthesized at 800 °C. The decrease in sintering temperature resulted in the change of microstructure. It is interesting to note that almost identical

58

microstructure was observed for the garnet specimens prepared in both of the cases. As seen, the aggregates of nano-sized particles with the size of less than 150 nm have formed. Moreover, the SEM pictures show the formation of very homogeneous mixed-metal oxides, and the formation of a continuous network of particles is evident.
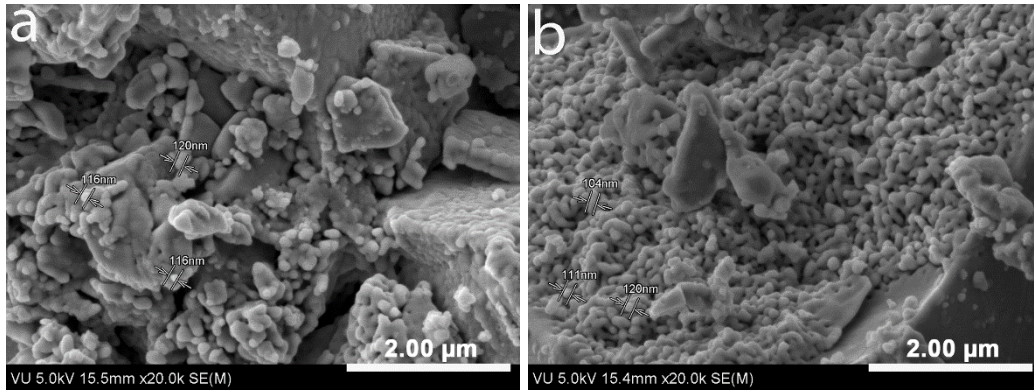
Figure 8.8. SEM micrographs of TbIG prepared with 1,2-ethanediol (M:EG = 1:1 (a)) and glycerol (M:GL = 1:1 (b)) and annealed at 800 °C.

8.2. Preparation and Characterization of $Y_3Fe_5O_{12}$

TG, DTG and DSC curves of Y–Fe–O precursor gels, prepared with 1,2-ethanediol and glycerol are shown in Figure 8.9.
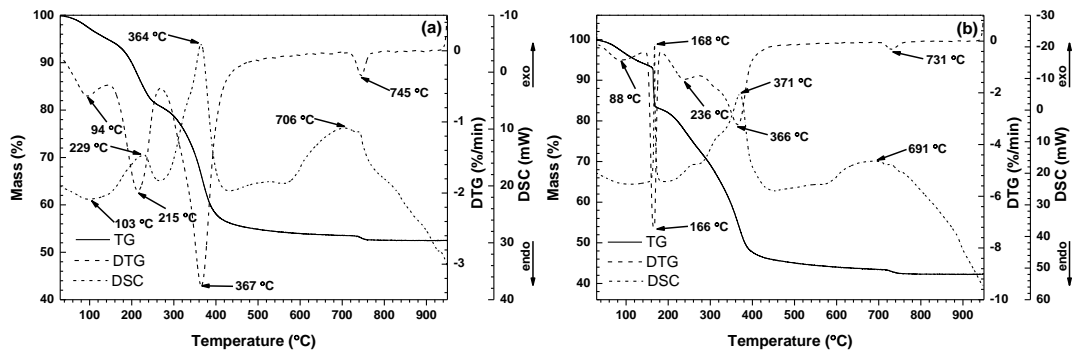
Figure 8.9. TG/DTG/DSC curves of the Y–Fe–O precursor gel synthesized with 1,2-ethanediol (a) and glycerol (b) as a complexing agent.

Thermal behaviour of Y–Fe–O gel presented in Figure 8.9a is associated with four main steps of mass loss, which are clearly seen in DTG curve. While thermal behaviour of Y–Fe–O gel prepared with glycerol shown in Figure 8.9b revealed five main mass loss steps. In both samples first step is related to the

59

evaporation of adsorbed water with the main peaks of 94 °C and 88 °C in the DTG curves, respectively. This is also evident from the endothermic signals in the DSC curves. The second step of mass loss observed in the range of ~200–250 °C by heating the Y–Fe–O precursor gel prepared with 1,2-ethanediol can be related to the beginning of decomposition of gel with formation of the intermediate species. Whereas, the second step of mass loss of Y–Fe–O precursor gel prepared with glycerol has the maximum at lower temperature (166 °C) in the DTG curve accompanied with DSC exothermic signal with the maximum at 168 °C. This signal can be attributed to the reaction of nitrates with glycerol during partial combustion, as typical sharp exothermic peak at around 170 °C occurs for the nitrate-citrate gel in the YIG synthesis by auto-combustion method [162]. On the other hand, this could be associated with decomposition of precursor, which contains iron nitrate (see Figure 8.3c), indicating the presence of starting material in the Y–Fe–O glycerate gel. Thus, these results let us to predict that the gel prepared with glycerol is inhomogeneous. In Figure 8.9b there is a slight mass loss at around 236 °C, which is in a good agreement with the primary glycerol decomposition and evaporation temperature shown in Figure 8.3b.

Obviously, the prepared Y–Fe–O glycerate gel is not homogeneous and this can influence the formation and phase purity of the final product [163, 164]. The mass losses with maxima in DTG curves at 364 °C (Figure 8.9a) and at 366 °C (Figure 8.9b) can be attributed to the decomposition of intermediate products. Yttrium acetate decomposition process itself is initiated by the breaking of the bond between the metallic cation and the acetate ligand at about 372 °C [165]. When the bond is broken, large organic fragments are volatilized, and the observed mass loss is related to the volatilization of these organic fragments. In the presence of oxygen, the combustion of organic fragments present in the gas phase results in a highly exothermic process that masks the endothermic signal related to yttrium acetate decomposition [165, 166]. Some authors claim, that mass loss at around 764 °C indicates the transformation of the complex to the oxide and the two exothermic peaks indicate the

crystallization of the YIG phase in two stages. Double peak may be due to the crystallization of orthoferrite followed by the formation of YIG phase at higher temperature [167]. In our case, the last mass loss step in both cases can be attributed to the formation of mixed-metal oxides. It is obvious from TG/DSC measurements, that different sol-gel synthesis conditions influence on the mechanism of thermal decomposition of gels and consequently on the formation of final product.

Powder XRD patterns of gels prepared with 1,2-ethanediol and glycerol and sintered at various temperatures are shown in Figure 8.10. The reference XRD pattern of $Y_3Fe_5O_{12}$ is also added.
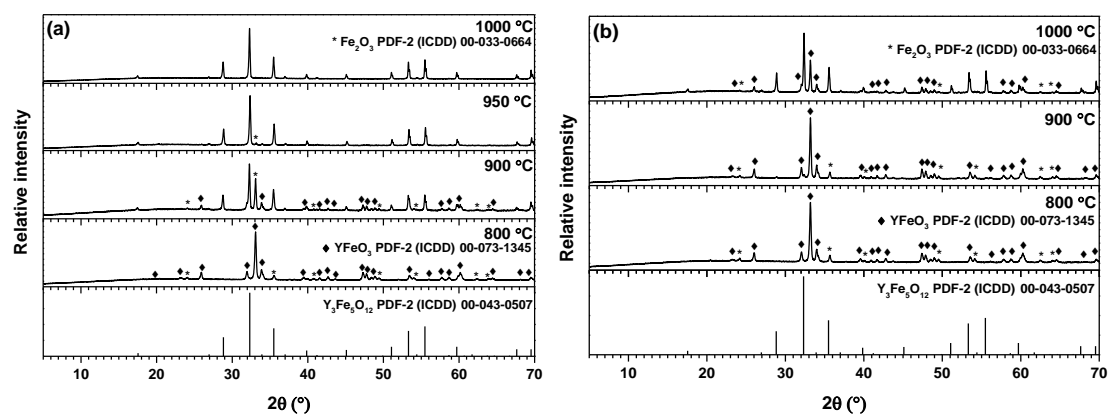
Figure 8.10. XRD patterns of Y–Fe–O gels synthesized with 1,2-ethanediol (a) and glycerol (b), and heated at various temperatures for 10 h. Vertical lines represent standard XRD pattern of $Y_3Fe_5O_{12}$.

It is evident, that usage of different complexing agent in sol-gel processing gave different final synthesis products. From Figure 8.10a we can see, that in the sol-gel processing with 1,2-ethanediol a single phase YIG is formed at 1000 °C, while at 950 °C small diffraction peak of Fe_2O_3 is visible. The synthesis at lower temperature (900 °C) leads to the formation of $Y_3Fe_5O_{12}$ with the side phases of $YFeO_3$ and Fe_2O_3. Meanwhile, annealing Y–Fe–O glycolate gel at 800 °C resulted in formation of perovskite $YFeO_3$ with impurities of Fe_2O_3. On the other hand, the sol-gel preparation of YIG with glycerol was not successful, since no monophasic garnet was obtained. Even at high temperature (1000 °C) the formation of mixture of YIG with $YFeO_3$ and Fe_2O_3 occurs. Moreover, the main

diffraction peaks of products obtained at 800 and 900 °C correspond to yttrium iron orthoferrite and iron(III) oxide. Thus, the XRD measurements revealed that high-purity YIG was obtained only using 1,2-ethanediol as complexing agent at 1000 °C.

The SEM micrographs of two YIG samples prepared using 1,2-ethanediol in the sol-gel processing are shown in Figure 8.11. Both samples can be characterized with similar surface morphology.

Individual particles seem to be submicro-sized (~500 nm) spherical crystallites and they partially fused to form hard agglomerates. The YIG sample, prepared at lower temperature has slightly smaller particles all over with more porous structure.
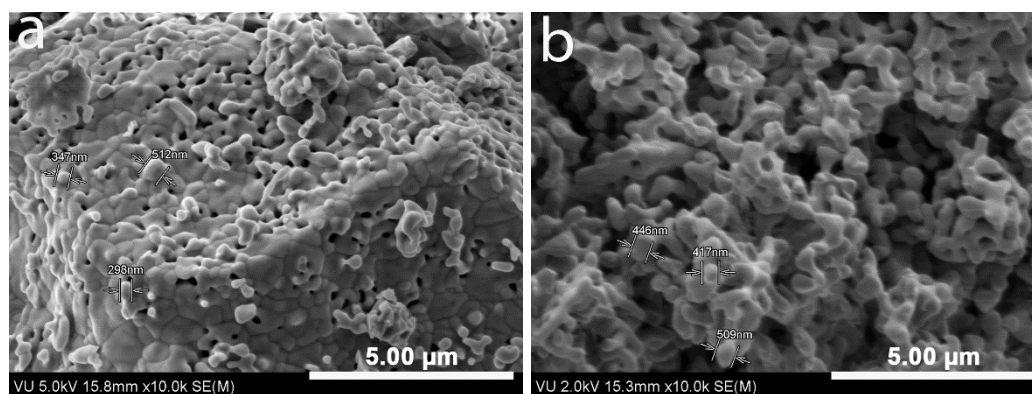
Figure 8.11. SEM micrographs of YIG prepared with 1,2-ethanediol and annealed at 950 °C (a) and 1000 °C (b).

Chapter 9. Sol-Gel Synthesis and Characterization of $Ln_3Fe_5O_{12}$ (Ln = Sm–Lu)

9.1. Characterization by Thermal Analysis, XRD and SEM

The thermal decomposition mechanism of the precursor gels of marginal lanthanides (Sm and Lu) in the series was studied by TG/DSC measurements. The representative TG/DTG/DSC curves of Sm–Fe–O and Lu–Fe–O precursor gels are shown in Figure 9.1.
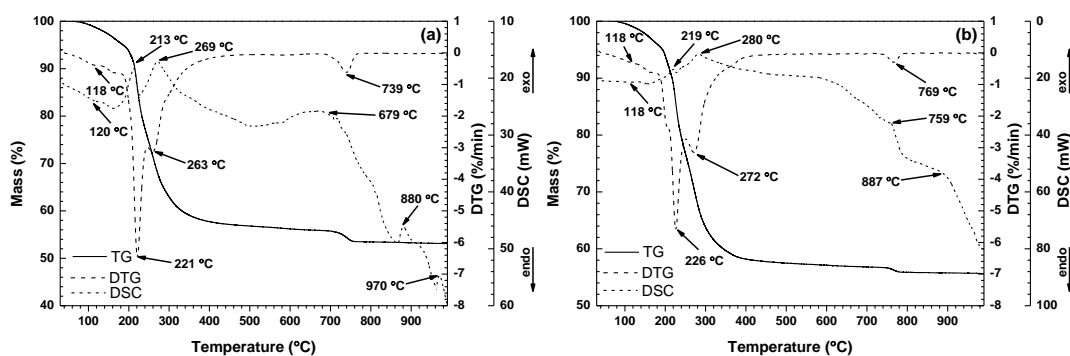
Figure 9.1. TG/DTG/DSC curves of the Sm–Fe–O (a) and Lu–Fe–O (b) precursor gel synthesized with 1,2-ethanediol as a complexing agent.

The DTG curves reveal that thermal behaviour of both samples is associated with four main steps of mass loss. First mass loss step is related to the release of residual water in the gel and can be seen at around 118 °C for both samples. Other two mass loss steps in both gels appear at very similar temperatures (221 °C and 263 °C for Sm–Fe–O gel and 226 °C and 272 °C for Lu–Fe–O gel). These results let us conclude that similar mechanism of initial and main decomposition of precursor gels occurs due to the similarity of chemical composition of complexes formed during the synthesis of the gels. The last mass loss step is seen at 739 °C for Sm–Fe–O and at 769 °C for Lu–Fe–O precursors. The DSC curve of Sm–Fe–O gel shows the existence of two exothermic peaks at 880 °C and 970 °C. The first one could be attributed to the beginning of crystallization of mixture composed of perovskite and garnet phases. The second exothermic peak could be related to the beginning of final re-crystallization of the garnet structure material from perovskite, as similar crystallization temperature was observed for $Sm_3Fe_5O_{12}$ fabricated by co-precipitation method [126]. Contrary, these two peaks are not visible in the DSC curve of Lu–Fe–O gel, indicating that the final temperature required for the formation of this garnet is lower. We can also predict that a negligible exothermic peak located at around 887 °C can be attributed to the initial decomposition of lutetium iron garnet to perovskite.

For the better understanding of the formation of the end product by sol-gel process, thermal behaviour of Ho–Fe–O gel was investigated. TG, DTG and

63

DSC curves of Ho–Fe–O precursor gel carried out in the flowing air are shown in Figure 9.2a.
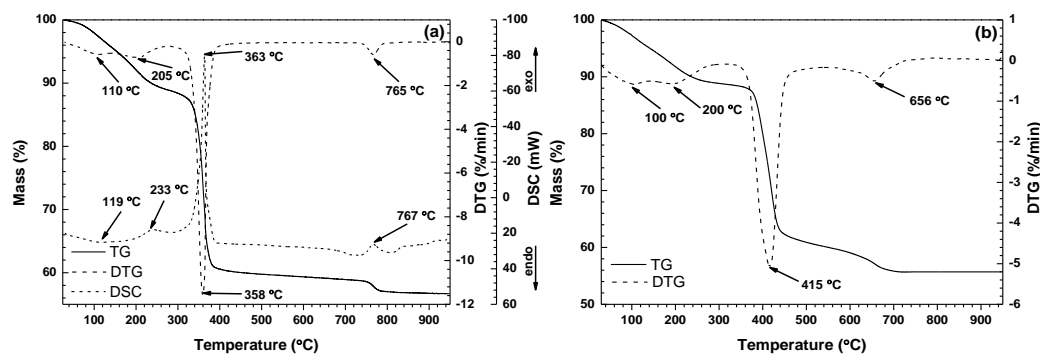
Figure 9.2. Thermal behaviour of Ho–Fe–O precursor gel under flowing air (a) and nitrogen (b).

As can be seen from the DTG curve, thermal behaviour of the gel under flowing air is related to the four different mass loss steps centred at 110, 205, 358 and 765 °C. First mass loss step at 110 °C is mainly related to the release of water, which is probably trapped inside the porous gel network. This is also evident from the broad endothermic signal in the DSC curve. The second mass loss step observed in the range of around 160–260 °C is accompanied by an exothermic peak with the maxima at 233 °C. This can be assigned to the beginning of the decomposition of the organic part with the formation of intermediate species [168]. Mass loss and sharp exothermic peak at 363 °C in the DSC curve can be attributed to the decomposition of formed complexes during the gelation process, burning of weakly bound organic groups [169], and loss of coordinated ethylene glycol [157]. For similar garnet structure compounds, mass loss at around 765 °C indicates complete transformation from the complex type compound to the mixed-metal oxide [167].

The pyrolysis of Ho–Fe–O precursor gel was also investigated by TG–GC–MS analysis. Figure 9.2b shows TG and DTG curves of the Ho–Fe–O precursor gel under flowing nitrogen. As compared to the TG curve obtained in the air, the first two steps of mass loss occur almost in the same temperature, while third step has the maxima at higher temperature (415 °C). On the other hand, the last mass loss step occurs at lower temperature (656 °C).

64

Sampling of the evolved gas phase for TG–GC–MS analysis was performed at 415 and 656 °C in order to better identify compounds released during thermal decomposition process. Gas chromatographic elutions carried out at 415 and 656 °C are reported in Figure 9.3.

Figure 9.3. Gas chromatographic elutions of the gas phase evolved at 415 °C (top) and 656 °C (bottom) of Ho–Fe–O gel under flowing nitrogen. Mass spectra recorded corresponding to selected chromatographic peaks (TG–GC–MS analysis).

As shown in Figure 9.3, the release of CO_2 (m/z signal at 44) and acetone CH_3COCH_3 (m/z signals at 43 for CH_3CO^+ ion and at 58 for $CH_3COCH_3^+$) is detected at 415 °C. Evolution of these species is related to the decomposition

of organic part of intermediate complex gel network. On the contrary, only CO_2 signal (m/z at 44) is detected at higher thermal decomposition temperature (656 °C). As was mentioned before, the formation of mixed-metal oxide occurs at the temperature related to the final mass loss (656 °C). The release of CO_2 can be attributed to the decomposition of intermediates species such as oxycarbonates.

Figure 9.4 demonstrates the decomposition products at the main DTG peak of Ho–Fe–O precursor gel under flowing air. The main signal is assigned to the release of CO_2. In the presence of oxygen only CO_2 signal is seen, since the combustion of organic part occurs in the TG chamber. Only negligible amount of acetone CH_3COCH_3 (m/z signals at 43 for CH_3CO^+ ion and at 58 for $CH_3COCH_3^+$) is detected. The gel also contains nitrates, but decomposition of nitrates has to take place at lower temperatures. TG–GC–MS experiments of the lower temperature gases were not performed.

Figure 9.4. Gas chromatographic elutions of the gas phase evolved at 358 °C of Ho–Fe–O gel under flowing air. Mass spectra recorded corresponding to selected chromatographic peaks (TG–GC–MS analysis).

In order to better understand the decomposition of binary Ho–Fe–O precursor gel, the individual Fe–O and Ho–O gels were synthesized and

investigated by TG–GC–MS. TG/DTG curves of Fe–O gel and Ho–O gel are shown in Figure 9.5.
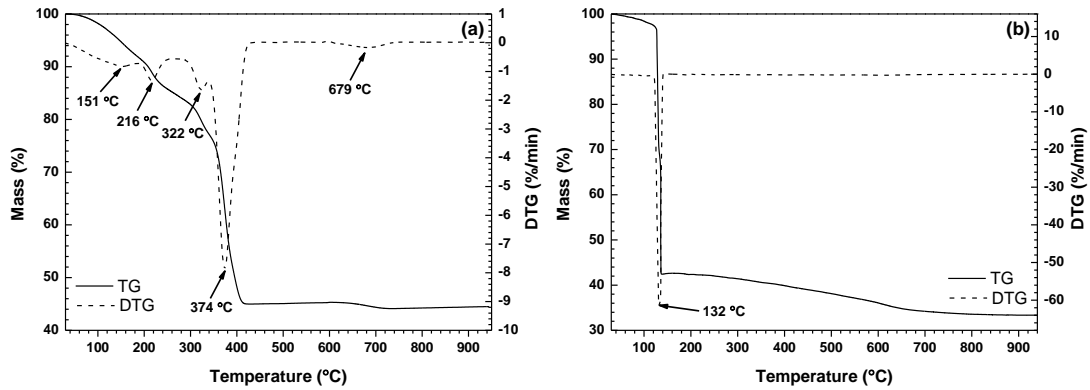
Figure 9.5. TG/DTG curves of the Fe–O (a) and Ho–O (b) precursor gels under flowing nitrogen.

Clearly, the main decomposition process of Fe–O gel occurs at 374 °C (Figure 9.5a). Gas chromatographic elution was performed at this temperature, and the results are presented in Figure 9.6.
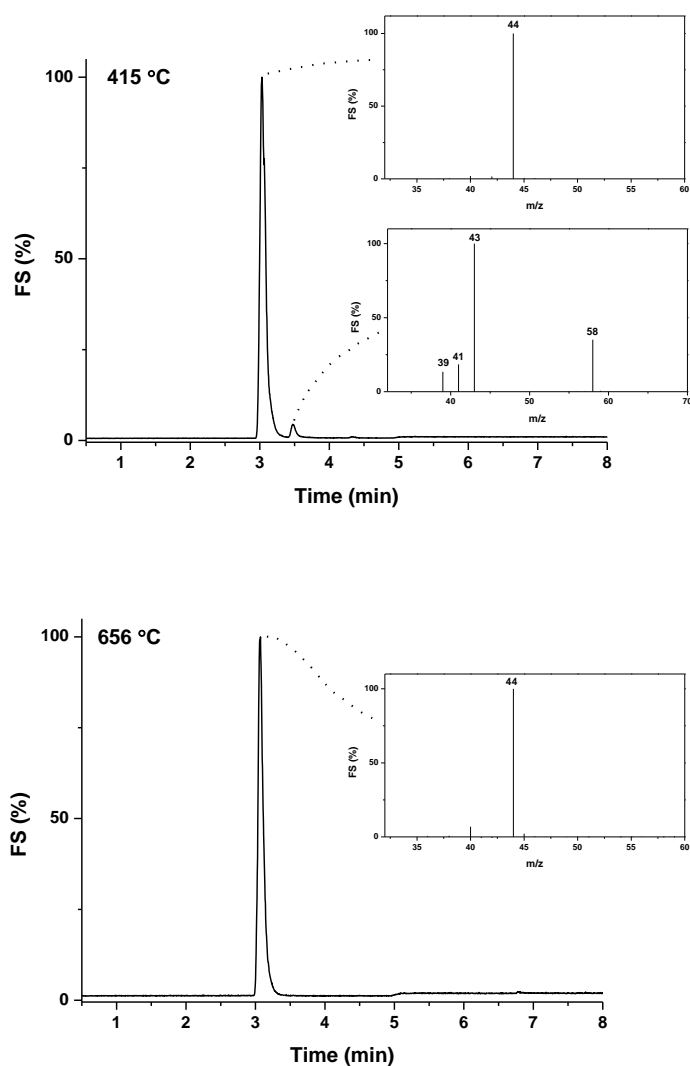

Figure 9.6. Gas chromatographic elutions of the gas phase evolved at 374 °C of Fe–O gel under flowing nitrogen. Mass spectra recorded corresponding to selected chromatographic peaks (TG–GC–MS analysis).

Obviously, the main released decomposition product is CO_2 (m/z signal at 44), whereas the compounds detected in the lower content are CH_3COCH_3 (m/z signals at 43 for CH_3CO^+ ion and 58 for $CH_3COCH_3^+$ ion) and $C_2H_5COCH_3$ (m/z signals at 43 for CH_3CO^+ ion and 72 for $C_2H_5COCH_3^+$ ion). Thermal decomposition of Ho–O gel also occurs via one mass loss step at 132 °C (Figure 9.5b). At this temperature obtained the gas chromatogram (Figure 9.7) presents few signals. The main release belongs to CO_2 (m/z signal at 44). In summary, evolved gases from Fe–O and Ho–O gels are the same as were determined during the decomposition of the Ho–Fe–O gel, except the small amount of $C_2H_5COCH_3$ (m/z signals at 43 for CH_3CO^+ ion and 72 for $C_2H_5COCH_3^+$ ion). TG–GC–MS measurements of Fe–O and Ho–O gels under flowing air showed release of CO_2 (m/z signal at 44) and confirmed burning of weakly bound organic groups as in the case of the Ho–Fe–O gel.
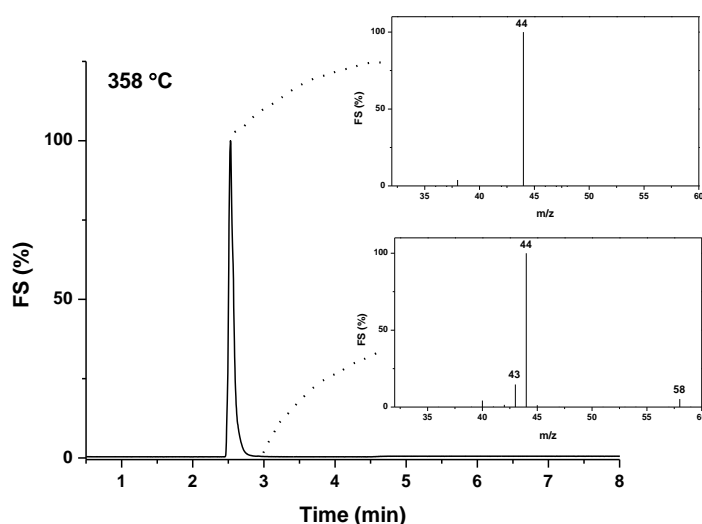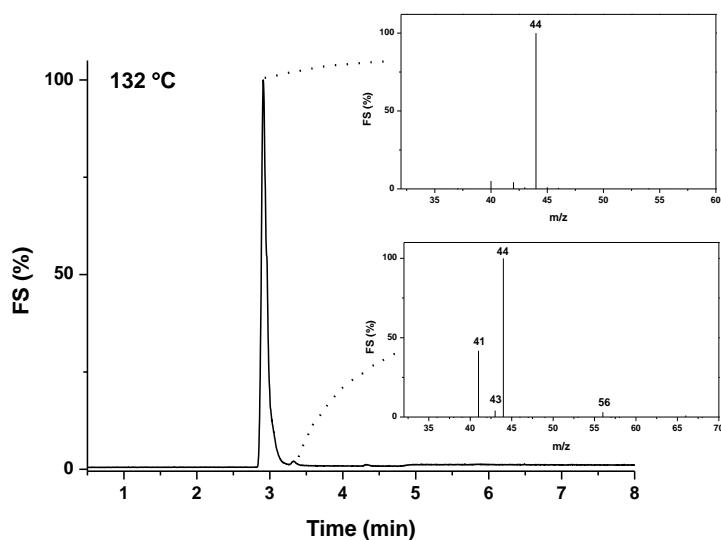

Figure 9.7. Gas chromatographic elutions of the gas phase evolved at 132 °C of Ho–O gel under flowing nitrogen. Mass spectra recorded corresponding to selected chromatographic peaks (TG–GC–MS analysis).

In the sol-gel processing, the 1,2-ethanediol was used as the complexing agent. In order to understand better the formation of the complexes, the TG–

68

GC–MS analysis of the 1,2-ethanediol was also performed (see Figures 9.8 and 9.9).
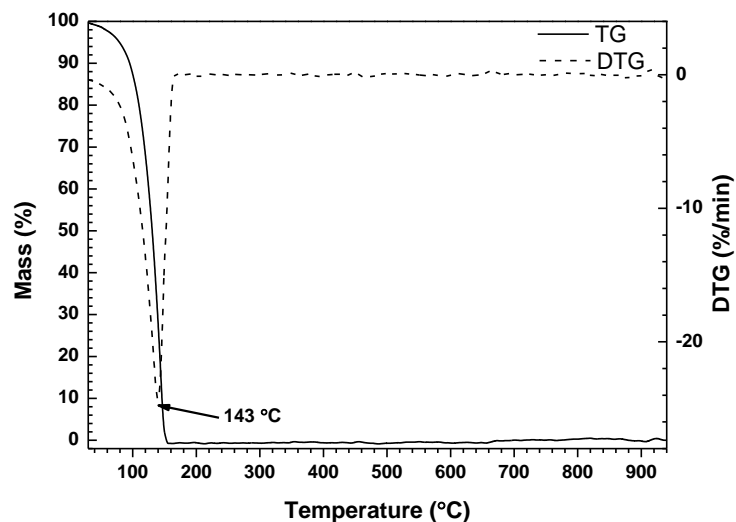
Figure 9.8. TG/DTG curves of the 1,2-ethanediol under flowing nitrogen.
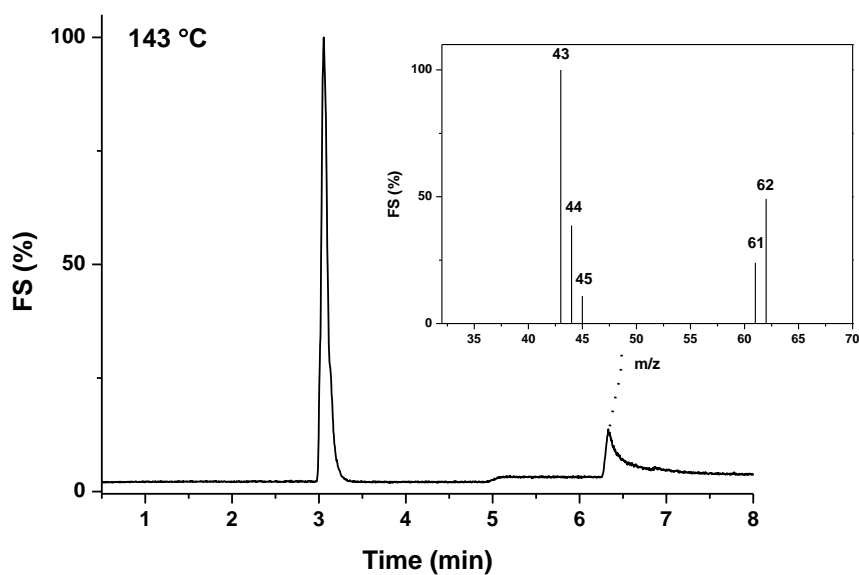
Figure 9.9. Gas chromatographic elutions of the gas phase evolved at 143 °C of 1,2-ethanediol under flowing nitrogen. Mass spectra recorded corresponding to selected chromatographic peaks (TG–GC–MS analysis).

Apparently, thermal decomposition and evaporation of the complexing agent occurs through one mass loss step at 143 °C. Main m/z signals are detected at 43 and 62. Figure 9.10 presents decomposition products of 1,2-

ethanediol under flowing air. It is clearly seen that the released products are slightly different. Besides CO_2 (m/z signal at 44) and 1,2-ethanediol (m/z signals at 43 and 62), 2-methyl-1,3-dioxolane is released (m/z signals at 73, 43, 45, 58 and 62). In comparison with all previously analysed gels, these signals were not detected before, showing that 1,2-ethanediol obviously forms coordination compounds with the metal ions during the formation of the gel network. Interestingly, the individual Fe–O and Ho–O gels as well as 1,2-ethanediol decomposed at lower temperatures in comparison with the bimetallic Ho–Fe–O gel. This observation let us to conclude that the binary Ho–Fe–O gel is more thermally stable.
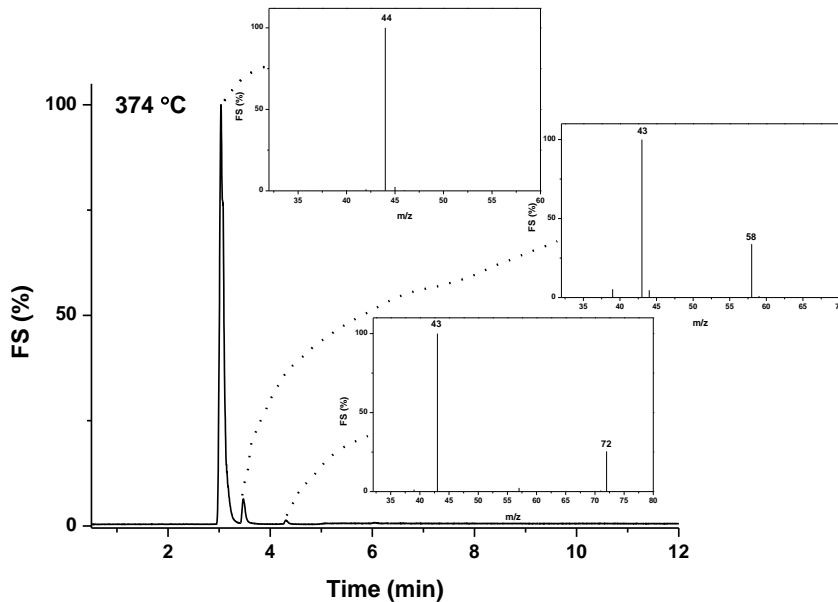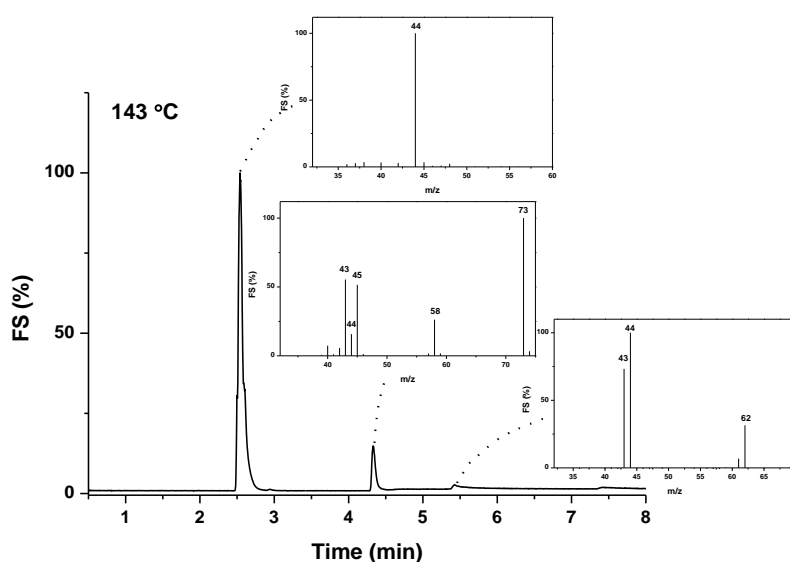

Figure 9.10. Gas chromatographic elutions of the gas phase evolved at 143 °C of 1,2-ethanediol under flowing air. Mass spectra recorded corresponding to selected chromatographic peaks (TG–GC–MS analysis).

The XRD patterns of all synthesized samples at different temperatures are presented in Figure 9.11. Obviously, the garnet as dominant crystalline phase could be determined in all cases. However, the phase purity of different lanthanide iron garnets depends on the final annealing temperature.

(a) 1000 °C
* Fe_2O_3 PDF-2 (ICDD) 00-033-0664
♦ $SmFeO_3$ PDF-2 (ICDD) 00-074-1474
900 °C
800 °C
$Sm_3Fe_5O_{12}$ PDF-2 (ICDD) 00-023-0526

(b) 1000 °C
* Fe_2O_3 PDF-2 (ICDD) 00-033-0664
♦ $EuFeO_3$ PDF-2 (ICDD) 00-074-1475
900 °C
800 °C
$Eu_3Fe_5O_{12}$ PDF-2 (ICDD) 00-071-0696

(c) 1000 °C
* Fe_2O_3 PDF-2 (ICDD) 00-033-0664
♦ $GdFeO_3$ PDF-2 (ICDD) 00-047-0067
900 °C
800 °C
$Gd_3Fe_5O_{12}$ PDF-2 (ICDD) 00-072-0141

(d) 1000 °C
* Fe_2O_3 PDF-2 (ICDD) 00-033-0664
♦ $DyFeO_3$ PDF-2 (ICDD) 00-047-0069
900 °C
800 °C
$Dy_3Fe_5O_{12}$ PDF-2 (ICDD) 00-023-0237

(e) 1000 °C
* Fe_2O_3 PDF-2 (ICDD) 00-033-0664
♦ $HoFeO_3$ PDF-2 (ICDD) 00-046-0115
900 °C
800 °C
$Ho_3Fe_5O_{12}$ PDF-2 (ICDD) 00-023-0282

(f) 1000 °C
* Fe_2O_3 PDF-2 (ICDD) 00-033-0664
♦ $ErFeO_3$ PDF-2 (ICDD) 00-047-0072
900 °C
800 °C
$Er_3Fe_5O_{12}$ PDF-2 (ICDD) 00-023-0240

(g) 1000 °C
* Fe_2O_3 PDF-2 (ICDD) 00-033-0664
♦ $TmFeO_3$ PDF-2 (ICDD) 00-046-0114
900 °C
800 °C
$Tm_3Fe_5O_{12}$ PDF-2 (ICDD) 00-023-0591

(h) 1000 °C
* Fe_2O_3 PDF-2 (ICDD) 00-033-0664
♦ $YbFeO_3$ PDF-2 (ICDD) 00-047-0070
900 °C
800 °C
$Fe_5Yb_3O_{12}$ PDF-2 (ICDD) 00-073-1376

Relative intensity

2θ (°)

71

Figure 9.11. XRD patterns of Sm–Fe–O (a), Eu–Fe–O (b), Gd–Fe–O (c), Dy–Fe–O (d), Ho–Fe–O (e), Er–Fe–O (f), Tm–Fe–O (g), Yb–Fe–O (h) and Lu–Fe–O (i) gels annealed at 800, 900 and 1000 °C. The vertical lines represent the standard XRD pattern of appropriate rare earth iron garnet.

It was determined, that samarium, europium and gadolinium orthoferrites ($LnFeO_3$) were dominant after heat-treatment of precursor gels at 800 °C (see Figure 9.11a, b and c, respectively). By increasing the temperature to 900 °C, $SmFeO_3$ still remained the main crystalline phase in the end product. However, in the europium and gadolinium cases almost monophasic garnets $Eu_3Fe_5O_{12}$ and $Gd_3Fe_5O_{12}$ have formed. Finally, the pure $Sm_3Fe_5O_{12}$ phase was obtained only after annealing the precursor gel at 1000 °C.

The terbium iron garnet $Tb_3Fe_5O_{12}$ was already predominant crystalline phase in the synthesis product obtained at 800 °C (see Figure 8.5). Only minor amount of $TbFeO_3$ could be detected in the XRD pattern. The reflections, attributable to perovskite phase, almost disappeared with the increasing temperature up to 900–1000 °C (see Figure 8.4). The phase purity of $Dy_3Fe_5O_{12}$ garnet was almost independent on the synthesis temperature in the range of 800–1000 °C (Figure 9.11 d). In the case of holmium and erbium, the opposite effect was observed. The most pure $Ho_3Fe_5O_{12}$, $Er_3Fe_5O_{12}$ and $Tm_3Fe_5O_{12}$ garnet phases were obtained already at the lower used synthesis temperatures 800, 900 and 800 °C, respectively. With the increasing synthesis temperature the amount of side perovskite $HoFeO_3$, $ErFeO_3$ and $TmFeO_3$ phases also increased (Figure 9.11e, f and g, respectively).

72

Interestingly, the monophasic ytterbium and lutetium iron garnets ($Yb_3Fe_5O_{12}$ and $Lu_3Fe_5O_{12}$) were successfully synthesized only at 800 °C. Further increase of temperature facilitates formation of lanthanide metal orthoferrites (Figure 9.11h and i). It is evident, that crystallization of rare earth iron garnet phase in the series of Sm–Lu elements depends on the final annealing temperature significantly. As it is seen from XRD results, the formation of iron garnets with the marginal lanthanides in the series ($Sm_3Fe_5O_{12}$ and $Lu_3Fe_5O_{12}$) occurs at quite different temperatures.

Representative images of SEM of some rare earth iron garnets are presented in Figure 9.12. Images revealed that surface morphology of prepared samples is dependent on the final annealing temperature. It is evident from SEM images, that independently from the phase composition the larger particles have formed at higher temperatures. Table 9.1 presents the results of particle size calculated from SEM images using *ImageJ* program.
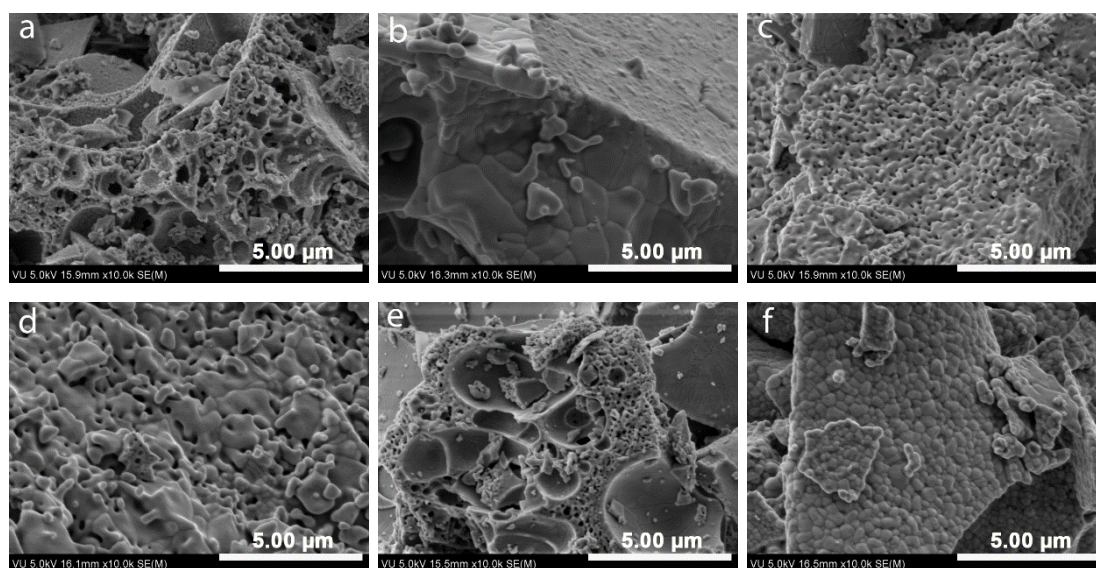
Figure 9.12. SEM micrographs of Sm–Fe–O gels annealed at 800 °C (a) and 1000 °C (b), Ho–Fe–O gels annealed at 900 °C (c) and 1000 °C (d), and Lu–Fe–O gels annealed at 800 °C (e) and 1000 °C (f).

73

Table 9.1. Average particle size calculated from SEM images.

Gel	Particle size (nm) at different annealing temperatures		
	800 °C	900 °C	1000 °C
Sm–Fe–O	100	161	779
Eu–Fe–O	88	142	359
Gd–Fe–O	101	398	657
Tb–Fe–O	76	353	409
Dy–Fe–O	122	279	431
Ho–Fe–O	113	142	391
Er–Fe–O	121	299	484
Tm–Fe–O	121	290	517
Yb–Fe–O	129	190	305
Lu–Fe–O	115	125	267

The garnets prepared at 1000 °C are composed of particles 250–800 nm in size. The particle size does not exceed 400 nm for the synthesis products obtained at 900 °C. The smallest particles with the narrow particle size distribution (75–130 nm) were obtained at 800 °C. Moreover, the particles are highly agglomerated independently on the annealing temperature. The formation of agglomerates covered by smaller particles is typical for different sol-gel derived compounds [170, 171]. Compounds, sintered at lower temperatures show also open porous surface microstructure.

9.2. Magnetic Properties

9.2.1. Mössbauer Spectroscopy Data Analysis

Sol-gel derived $Ln_3Fe_5O_{12}$ garnets were investigated using Mössbauer spectroscopy. For garnet structure materials Mössbauer spectroscopy is an important tool to estimate structural changes, hyperfine interaction, and magnetic behaviour and to determine the distribution of Fe^{3+} ions among sublattices of garnet structure [172]. The room temperature Mössbauer spectra of Sm–Fe–O gel sample annealed at 1000 °C and Lu–Fe–O gel sample annealed at 800 °C are shown in Figure 9.13.
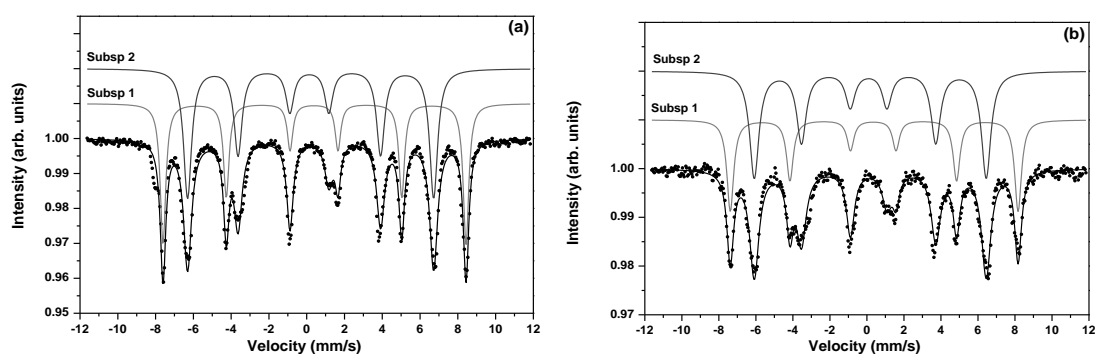
Figure 9.13. Mössbauer spectra of Sm–Fe–O gel sample annealed at 1000 °C (a) and Lu–Fe–O gel sample annealed at 800 °C (b).

The Mössbauer spectra for the iron garnets were found to consist of two magnetic subspectra (sextets). One corresponds to the octahedral sublattice and the other to the tetrahedral sublattice [173, 174]. It is obvious that overall shapes of Sm–Fe–O gel sample annealed at 1000 °C and Lu–Fe–O gel sample annealed at 800 °C spectra (Figure 9.13a and b) are essentially independent on the nature of the rare earth ion. Table 9.2 summarizes the hyperfine parameter values obtained for the purest studied garnet systems.

Relative area of the subspectrum S shows relative amount of the phase in the sample considering the Mössbauer effect probabilities for the phases. The difference in isomer shift and hyperfine magnetic field for different sites is due to nonequivalent octahedral and tetrahedral positions in the garnet structure. Trivalent iron ions with octahedral coordination have a less quadrupole splitting and larger isomeric shift than with tetrahedral coordination (Table 9.2).

Mössbauer spectra of rare earth iron garnets showed hyperfine magnetic splitting. For studied garnets, the magnetic hyperfine fields are found to be around 49 T for a sites and 39 T for d sites and are in a good agreement with reported elsewhere [172, 175]. Variation of hyperfine magnetic field (B) with lanthanide ion in the garnet is shown in Figure 9.14.

Table 9.2. Data from Mössbauer spectra measured at room temperature: S is relative area of subspectrum, Γ, δ, 2ε, B are line width, isomer shift, quadrupole splitting and hyperfine field, respectively.

Sample	T_{ann}, °C	S, %	Γ, mm/s	δ, mm/s	2ε, mm/s	B, T	Phase
Sm–Fe–O	1000	42.98	0.35	0.40	0.03	49.83	SmIG a sites
		57.02	0.51	0.17	0.07	40.47	SmIG d sites
Eu–Fe–O	1000	41.56	0.35	0.39	0.04	49.65	EuIG a sites
		58.44	0.52	0.17	0.07	40.32	EuIG d sites
Gd–Fe–O	1000	39.37	0.34	0.39	0.05	49.40	GdIG a sites
		60.63	0.44	0.16	0.02	40.26	GdIG d sites
Tb–Fe–O	1000	39.05	0.37	0.39	0.05	49.25	TbIG a sites
		60.95	0.49	0.16	0.03	39.99	TbIG d sites
Dy–Fe–O	800	38.85	0.40	0.38	0.02	48.92	DyIG a sites
		61.15	0.62	0.15	0.11	39.64	DyIG d sites
Ho–Fe–O	800	36.28	0.41	0.38	0.04	48.64	HoIG a sites
		63.72	0.62	0.15	0.08	39.38	HoIG d sites
Er–Fe–O	900	37.27	0.40	0.37	0.04	48.53	ErIG a sites
		62.73	0.56	0.14	0.07	39.30	ErIG d sites
Tm–Fe–O	800	38.18	0.42	0.37	0.05	48.48	TmIG a sites
		61.82	0.58	0.15	0.07	39.10	TmIG d sites
Yb–Fe–O	800	37.37	0.42	0.37	0.06	48.40	YbIG a sites
		62.63	0.59	0.14	0.09	39.03	YbIG d sites
Lu–Fe–O	800	38.31	0.44	0.37	0.05	48.31	LuIG a sites
		61.69	0.61	0.14	0.09	38.93	LuIG d sites
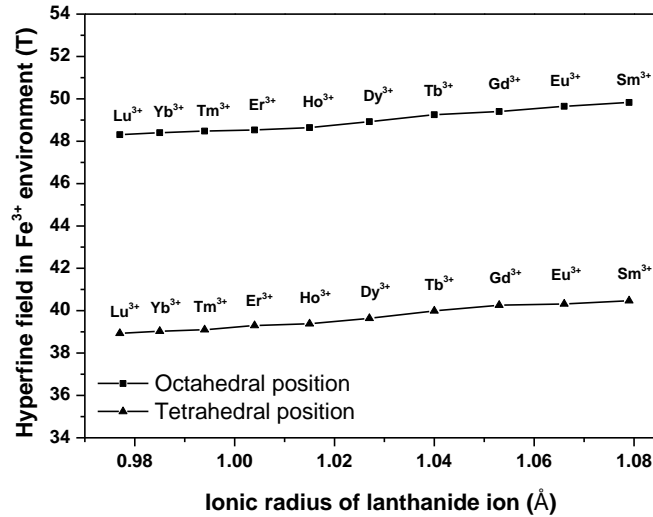
Figure 9.14. Hyperfine magnetic field dependence of ionic radius of lanthanide ion in the garnet.

The hyperfine field B at the iron nucleus may be expressed as the sum of few parts: B_{orb}, B_{latt}, B_{dip} and B_c. B_{orb} is a field on the nucleus of a free Fe^{3+} ion, B_{latt} is a crystal environment contribution, which arises from the covalency of the Fe^{3+}–O^{2-} bond and from a supertransferred hyperfine field related to the magnetic interaction in the cation–ligand–cation chain. B_{dip} is a dipolar field contribution caused by the surrounding magnetic moments, and B_c is the Fermi contact term [176, 177]. Changes in the B_{latt} and B_{dip} appear due to the replacement of the ion in the c site [178]. Fe^{3+}–O^{2-} bond lengths for those Fe^{3+} ions which are near rare earth ion changes, when one ion in the c site is substituted by the other one. This change causes the change in hyperfine field as the covalency is modified. What is more, rare earth ions have different electronic structures and mutual transfer of electrons which also leads to the change of hyperfine field [179]. As can be seen from Figure 9.14, hyperfine magnetic field decreases with an increase of atomic number of rare earth ion in both sublattices. As was shown before, substitution of lanthanide ion with bigger ionic radius to smaller one reduces the hyperfine magnetic field [180]. Effect of the substitution on hyperfine field at neighbouring iron nuclei was said to be dependent on the ionic radius of the substituent when measured with the nuclear magnetic resonance (NMR) technique [181].

9.2.2. Magnetic Hysteresis Data Analysis

In order to find correlation between the particle size, composition and magnetic properties the magnetization measurements of the prepared garnet samples were investigated. The hysteresis loops of the purest samples are shown in Figures 9.15.
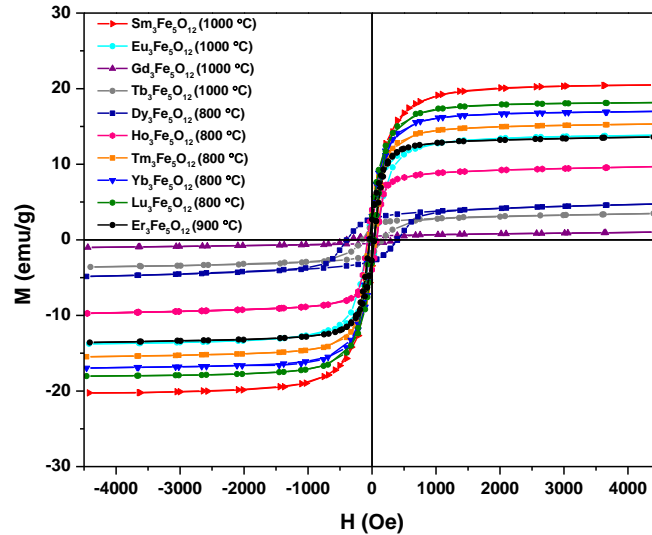
Figure 9.15. M versus H curves for rare earth iron garnets (at 25 °C).

The hysteresis of the samples varies with different rare earth ions in the composition. In most of the cases, the magnetization of the samples apparently do not saturate at applied magnetic field. Possibly, this is due to the contribution of magnetic moments of rare earth atoms, which paramagnetic behaviour gives a linear dependence of magnetization on the strength of the magnetic field [115]. Such contribution is mostly apparent for Gd, Tb and Dy iron garnets (Figures 9.15) for which the magnetization compensation temperature is closest to the measurement (room) temperature. At compensation temperature sublattice spontaneous magnetization cancel each other. In the sequence Gd, Tb and Dy compensation temperature decreases [182] showing the increase in spontaneous magnetization. However, for nanomaterials saturation of magnetization can also be affected by surface spin canting and other size-related effects [24, 183].

Magnetic characterization data of purest samples and those, with a very slight amount of the side phase are given in Table 9.3. Particle size of around

190 nm is small enough for single domain particles to exist in iron garnets [130]. In our case, garnets obtained at 800 °C could be single domain particles. In the case of bigger particles, multi domain structure exists, where regions of uniform magnetization are separated by domain walls, contrary to single domain structure. Because there are no domain walls to move, large coercivity appears for the particles that are small enough [105]. This can be explained, as the magnetization process in single domain materials involves the rotation of magnetization while in multi domain materials it takes place via movement of domain walls [184]. It can be seen, that coercivity decreases with the increasing particle size for the same garnet annealed at different temperature. These results are in a good agreement with the ones reported earlier [125]. However, these results could also be influenced by the phase purity. The coercivity is dramatically increased in $Gd_3Fe_5O_{12}$, $Tb_3Fe_5O_{12}$ and $Dy_3Fe_5O_{12}$, while remanence magnetization is lowest for $Gd_3Fe_5O_{12}$ and $Tb_3Fe_5O_{12}$. These results are consistent with other reports with similar compounds involving lanthanide ions [185]. Obtained saturation magnetization values correlate well with magnetization presented in the literature [186]; in the series Gd, Tb, Dy, Ho, Eu, Er, Tm, Yb, Lu, Sm saturation magnetization increases. Magnetic properties are claimed to be influenced essentially by magnetic moments [22], while some authors claimed, that in compounds with some lanthanide ions in the composition, different magnetic properties did not convincingly correlated with the total number of unpaired electrons of lanthanide ion or experimentally obtained magnetic moments. On the other hand, the strength of spin-orbit coupling alone could not explain different magnetic properties as well [185].

Such magnetic properties as coercivity are important for the practical application of the material. According to *Coey*, hard magnets have H_c>400 kA/m (~5 kOe), soft magnets – H_c<10 kA/m (~125 Oe) and magnetic recording media have intermediate values of coercivity [22]. Magnetic characterization data obtained from *M* versus *H* curves is presented in Table 9.3.

Table 9.3. Magnetic characterization data obtained M versus H curves at room temperature. H_c is coercivity, M_r is remanence, M_s is magnetization at H=4.4 kOe.

Sample	Annealing temperature, °C	Particle size, nm	H_c, Oe	M_r, emu/g	M_s, emu/g
$Sm_3Fe_5O_{12}$	1000	779	43.25	3.51	20.4
$Eu_3Fe_5O_{12}$	900	88	97.13	4.75	12.1
	1000	359	67.39	3.98	13.8
$Gd_3Fe_5O_{12}$	900	398	401.38	0.32	0.7
	1000	657	350.08	0.47	1.0
$Tb_3Fe_5O_{12}$	900	353	363.37	1.19	3.5
	1000	409	162.16	1.77	3.6
$Dy_3Fe_5O_{12}$	800	122	401.37	2.79	4.8
	900	279	274.65	2.33	4.4
	1000	431	235.62	2.59	5.0
$Ho_3Fe_5O_{12}$	800	113	72.23	3.92	9.8
	1000	391	58.35	2.85	9.6
$Er_3Fe_5O_{12}$	800	121	40.00	3.70	13.5
	900	299	34.00	2.40	13.7
	1000	484	35.00	2.40	14.2
$Tm_3Fe_5O_{12}$	800	121	41.56	3.19	15.4
	1000	517	22.93	1.64	14.9
$Yb_3Fe_5O_{12}$	800	129	33.25	2.99	17.0
$Lu_3Fe_5O_{12}$	800	115	32.86	3.03	18.1

It can be observed from Table 9.3, that $Gd_3Fe_5O_{12}$, $Tb_3Fe_5O_{12}$ and $Dy_3Fe_5O_{12}$, can act as magnetic recording media while the rest of the presented garnets have properties of soft magnetic material.

Depending on the field of application, various magnetic properties are required. Microwave switchers and other devices using the remanence or latching principle require high remanent magnetization and low coercive force, which are achieved with large grain size. While in some cases, a small grain size is necessary [187]. Thus, in order to use the materials for devices, the microstructure and particle size must be controlled during the processing.

9.2.3. Curie temperature

Curie temperature is important for the practical applications of magnetic materials and can be determined by thermal analysis technique [188, 189]. Thermogravimetry with adapted small magnet was used to determine Curie temperature of holmium iron garnet samples annealed at 800, 900 and 1000 °C and other rare earth iron garnets. From the obtained thermomagnetic curves, the transition temperature from ferrimagnetic to paramagnetic state was observed. Figure 9.16a shows determined Curie temperature for $Ho_3Fe_5O_{12}$ obtained at different temperatures. Onset calculation was made at the end of the Curie point transition (Figure 9.16a $Ho_3Fe_5O_{12}$ annealed at 800 °C). Obviously, Curie temperature of holmium iron garnet samples prepared at various temperatures is almost the same; even the determined phase composition is slightly different. $Ho_3Fe_5O_{12}$ garnet annealed at 1000 °C has small impurities of perovskite-type $HoFeO_3$, while garnet phase is dominant for the sample annealed at 900 °C, but amount of $HoFeO_3$ is even higher (see Figure 9.11e). For the $Ho_3Fe_5O_{12}$ garnet annealed at 800 °C Curie temperature is 281.0 °C, for synthesized at 900 is 280.6 °C, and for synthesized at 1000 is 281.1 °C. The lowest Curie point was determined for the $Ho_3Fe_5O_{12}$ sample prepared at 900 °C, which has the highest amount of side phase. In conclusion, we can say that small amount of impurity phase does not affect the value of Curie point significantly.

Further, Curie temperatures of other rare earth iron garnets were determined by the same way. Curie temperatures of rare earth iron garnets are shown in Figure 9.16b. As seen, in the series of lanthanide ions from Sm^{3+} to Lu^{3+} Curie temperature monotonically decreases. These results are in the good agreement with the ones obtained for rare earth iron garnets measured from heat capacity data (see Figure 9.16, Literature value) [190]. Clearly, the nature of rare earth ion in the iron garnet affects the value of Curie temperature allowing to choose desirable Curie temperature by selecting the particular lanthanide iron garnet.
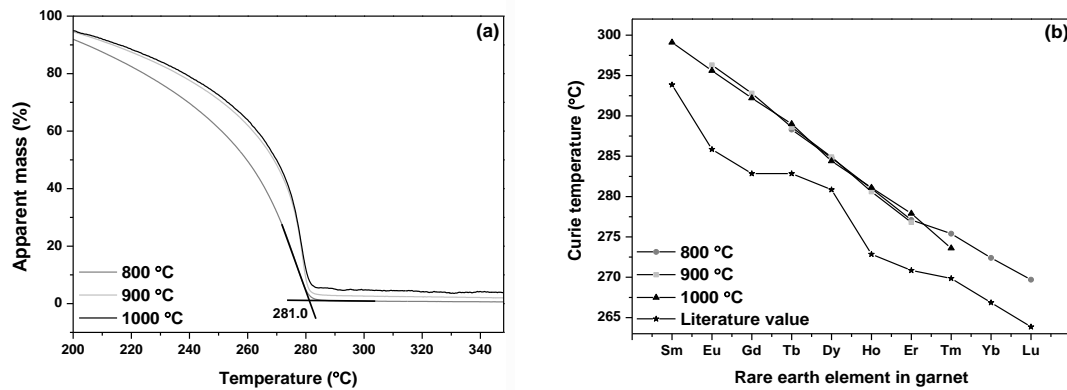
Figure 9.16. Mass changes of $Ho_3Fe_5O_{12}$ samples synthesized at 800, 900 and 1000 °C under external magnetic field (a) and Curie temperature of rare earth iron garnet (b).

Chapter 10. Sol-Gel Synthesis and Characterization of $Y_3Al_{5-x}Fe_xO_{12}$

10.1. Sol-Gel Synthesis and Characterization of bulk $Y_3Al_{5-x}Fe_xO_{12}$

Thermal analysis measurements were performed in order to find out the formation mechanism of mixed-metal garnets prepared by the sol-gel method. TG curves of various composition Y–Al–Fe–O precursor gels are shown in Figure 10.1. According to [191, 192], the main mass loss for aluminium nitrate octahydrate and $Al(NO_3)_3 \cdot 9H_2O$ was observed in the temperature range of 100–200 °C. Full decomposition of iron(III) nitrate nonahydrate is finished at around 150 °C (see Figure 8.3c). Obviously, the decomposition of the prepared Y–Al–Fe–O gels proceeds at higher temperatures. The main mass loss is slightly dependent on the starting composition of gels and could be observed in the temperature range of 250–450 °C. These results let us assume that formed Y–Al–Fe–O gels are characterized having a rather complex composition with more pronounced thermal stability in comparison with the used starting materials. Moreover, according to the TG analysis data, it is evident that no starting materials remain in the final precursor gels. As can be seen from Figure 10.1, the decomposition mechanisms of nonsubstituted precursor gels used for the formation of $Y_3Al_5O_{12}$ and $Y_3Fe_5O_{12}$ are slightly different. On the other hand,

82

thermal decomposition of mixed-metal Y–Al–Fe–O precursor gels is very similar.
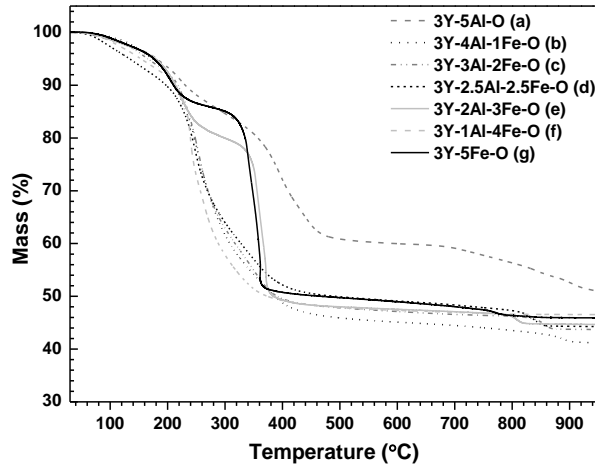
Figure 10.1. TG curves of Y–Al–Fe–O precursor gels having various starting compositions.

It is evident from the XRD pattern presented in Figure 10.2a that amorphous material is formed by heating the Y–Al–O precursor gel for 2 h at 800 °C. While rapid crystallization took place at 1000 °C and single-phase $Y_3Al_5O_{12}$ was formed. The XRD patterns of the Y–Fe–O gel annealed at 800 °C for 2 h and 1000 °C for 10 h are shown in Figure 10.2g. Apparently, in the synthesis product obtained at 800 °C the dominant phase is perovskite ($YFeO_3$). The garnet structure $Y_3Fe_5O_{12}$ phase has formed after annealing precursor gel at 1000 °C.

The XRD analysis of mixed-metal Y–Al–Fe–O gels sintered at 800 °C for 2 h and at 1000 °C for 10 h results are shown in Figure 10.2b–f. The obtained results are interesting indeed. Contrary to nonsubstituted $Y_3Al_5O_{12}$ and $Y_3Fe_5O_{12}$, the mixed-metal garnets $Y_3Al_{5-x}Fe_xO_{12}$ have already formed after the first stage of annealing of Y–Al–Fe–O precursor gels at 800 °C for 2 h. In the case of $Y_3Al_4FeO_{12}$, $Y_3Al_3Fe_2O_{12}$, $Y_3Al_{2.5}Fe_{2.5}O_{12}$, and $Y_3Al_2Fe_3O_{12}$, however, small impurities of iron(III) oxide phase have formed at both 800 °C and 1000 °C annealing temperatures. Finally, the monophasic mixed-metal garnet $Y_3Al_1Fe_4O_{12}$ has formed already at 800 °C (see Figure 10.2f).
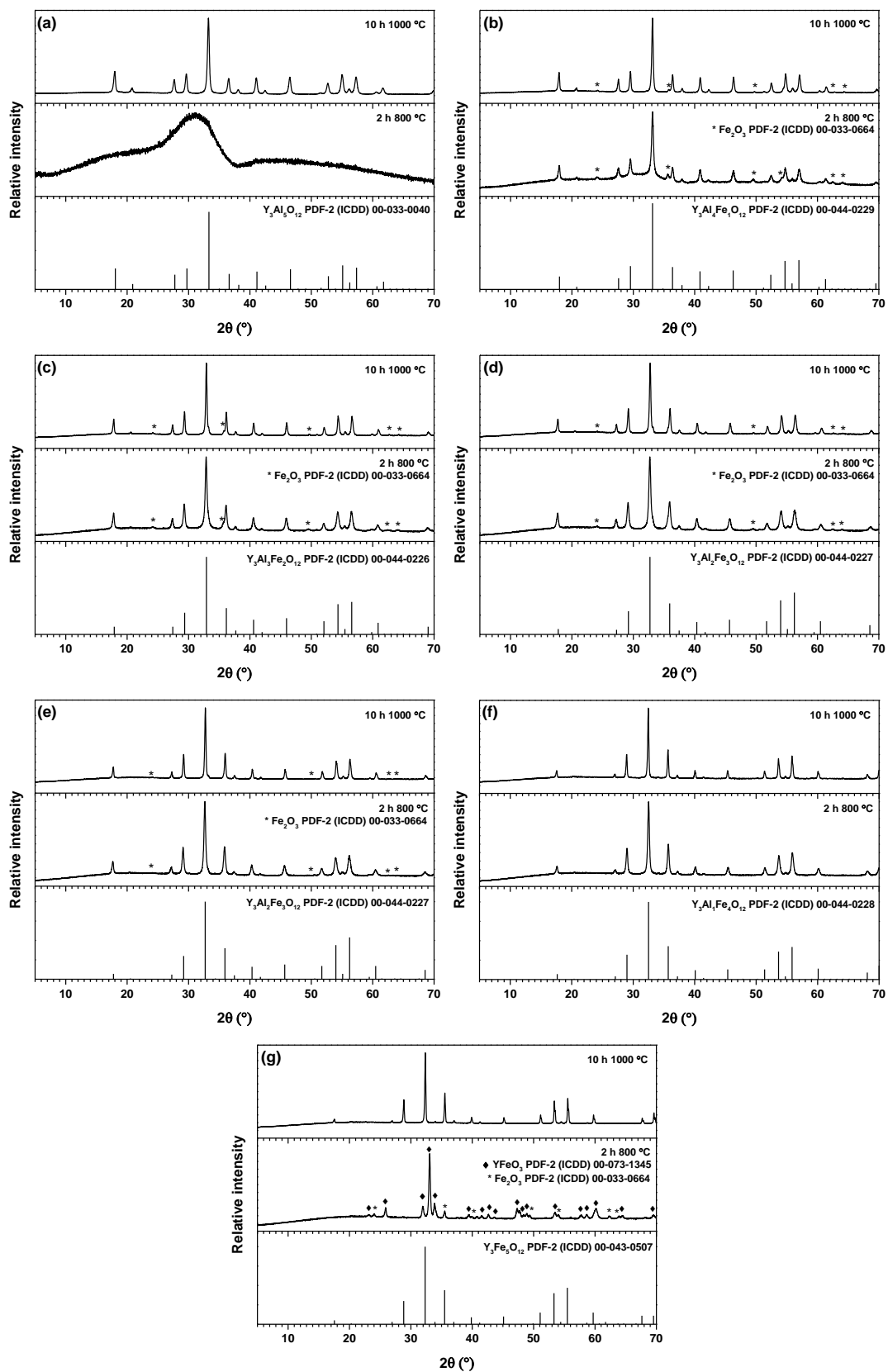
Figure 10.2. XRD patterns of 3Y–5Al–O (a), 3Y–4Al–1Fe–O (b), 3Y–3Al–2Fe–O (c), 3Y–2.5Al–2.5Fe–O (d), 3Y–2Al–3Fe–O (e), 3Y–1Al–4Fe–O (f), and 3Y–5Fe–O (g) precursor gels annealed at different temperatures.

All samples were investigated by IR spectroscopy. IR spectra of precursor gel samples and final samples are shown in Figure 10.3. Broad absorption band located at around $3400\,cm^{-1}$ and the band at $\sim 1630\,cm^{-1}$ could be assigned to the hydroxyl group of physically adsorbed or crystal water molecules [129, 193] in the precursor gel sample (Figure 10.3a). These results are in good agreement with thermal analysis results, where slight mass loss till 150°C was observed and assigned to the dehydration process. On the other hand, the band at $\sim 1630\,cm^{-1}$ can overlap with the C–O vibrations originated from the glycolate complex [194]. Absorption bands in the range of around $1700–800\,cm^{-1}$ could be attributed to the different vibrations within nitrate, which is present in the composition of gels. The absorption band observed in the IR spectra of the most samples at $2340\,cm^{-1}$ belongs to the adsorbed carbon dioxide from the atmosphere [195, 196].
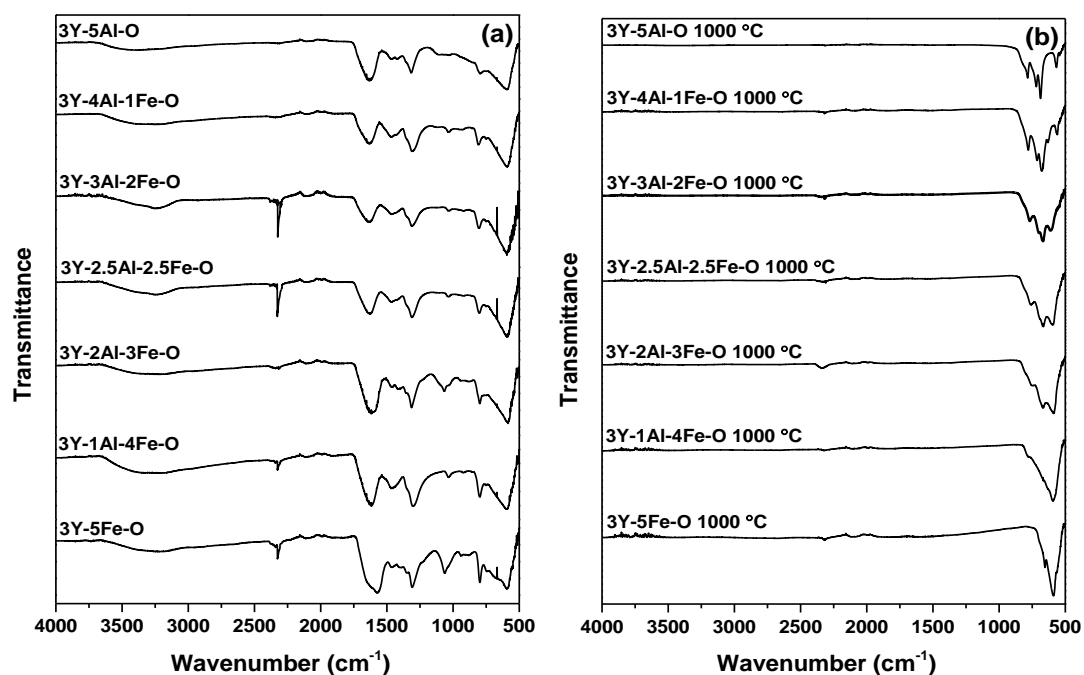

Figure 10.3. IR spectra of 3Y–5Al–O, 3Y–4Al–1Fe–O, 3Y–3Al–2Fe–O, 3Y–2.5Al–2.5Fe–O, 3Y–2Al–3Fe–O, 3Y–1Al–4Fe–O, and 3Y–5Fe–O precursor gels (a) and samples annealed at 1000 °C for 10 h.

IR spectroscopy was also used for the characterization of final synthesis products. Obviously, IR spectra of annealed samples are very different from the

gel ones. The IR spectra of samples annealed at 1000 °C for 10 h are shown in Figure 10.3b. Broad bands at $3400\,cm^{-1}$, $1700–800\,cm^{-1}$, and $1630\,cm^{-1}$ observed in the IR spectra of gel samples disappeared after sintering. The absorption bands located in the range of $400–800\,cm^{-1}$ correspond to the vibrations of metal–oxygen (M–O) bonds in metal oxides. For the YIG, absorption bands located at $594\,cm^{-1}$ and $653\,cm^{-1}$ belong to the asymmetric stretching of the tetrahedron Fe–O bond of the garnet system [197]. While, for yttrium aluminium garnet (YAG), this broad band is split to several peaks (784, 721, 687, and $567\,cm^{-1}$) [198, 199]. The results of IR spectroscopy evidently confirm the formation of solid solutions in the system $Y_3Al_{5-x}Fe_xO_{12}$ when aluminium is monotonically replaced by iron since less vibration occur in the IR spectra with increasing concentration of iron.

The surface microstructure of $Y_3Al_{5-x}Fe_xO_{12}$ samples was investigated by SEM. It was observed that obtained particles are highly agglomerated independent of the nominal composition. The representative SEM micrographs of $Y_3Al_{5-x}Fe_xO_{12}$ (x =0.0, 3.0, 4.0, 5.0) specimens are shown in Figure 10.4a–d.
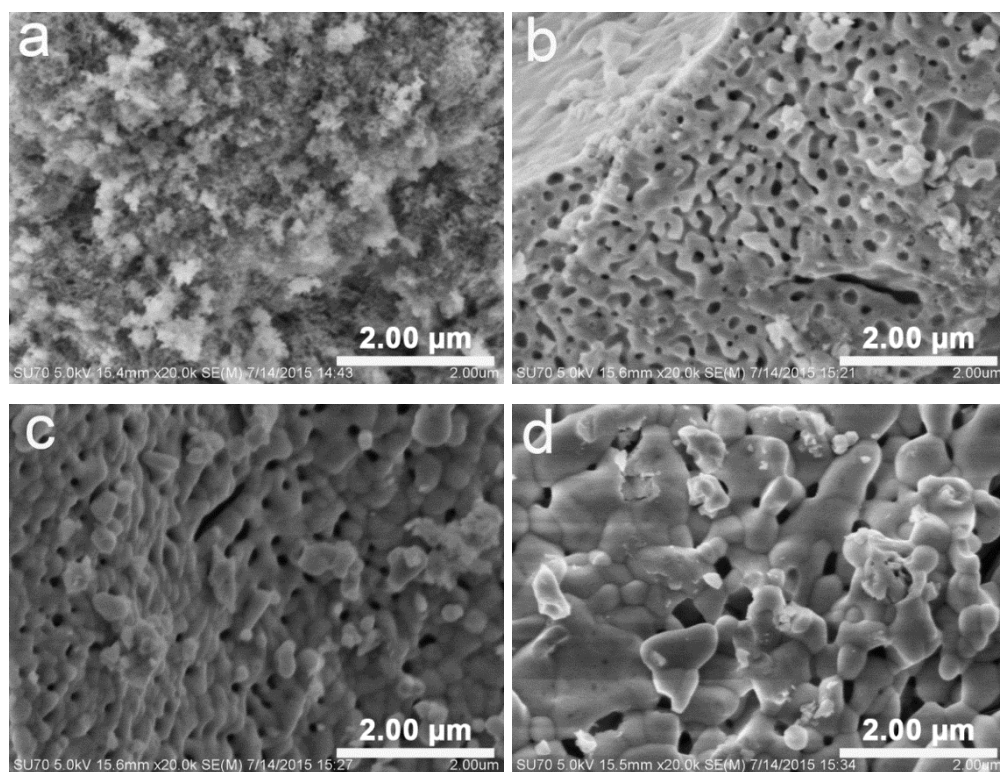
Figure 10.4. SEM micrographs of $Y_3Al_5O_{12}$ (a), $Y_3Al_2Fe_3O_{12}$ (b), $Y_3Al_1Fe_4O_{12}$ (c), and $Y_3Fe_5O_{12}$ (d) garnets obtained at 1000 °C.

It is clearly seen that the particle size of solids monotonically increases with increasing amounts of iron in the garnet structure. For instance, $Y_3Al_5O_{12}$ is composed of very small fine nanosized particles (Figure 10.4a); however, in the case of $Y_3Fe_5O_{12}$, the particles even larger than $1\,\mu m$ have formed (Figure 10.4d). While $Y_3Al_2Fe_3O_{12}$, and $Y_3Al_1Fe_4O_{12}$ are composed of elongated particles with around 100–200 nm in size.

The room temperature Mössbauer spectra for garnet samples synthesized at 1000 °C are shown in Figure 10.5. Pure $Y_3Al_5O_{12}$ was not characterized by Mössbauer spectroscopy, as it has no iron in the composition.
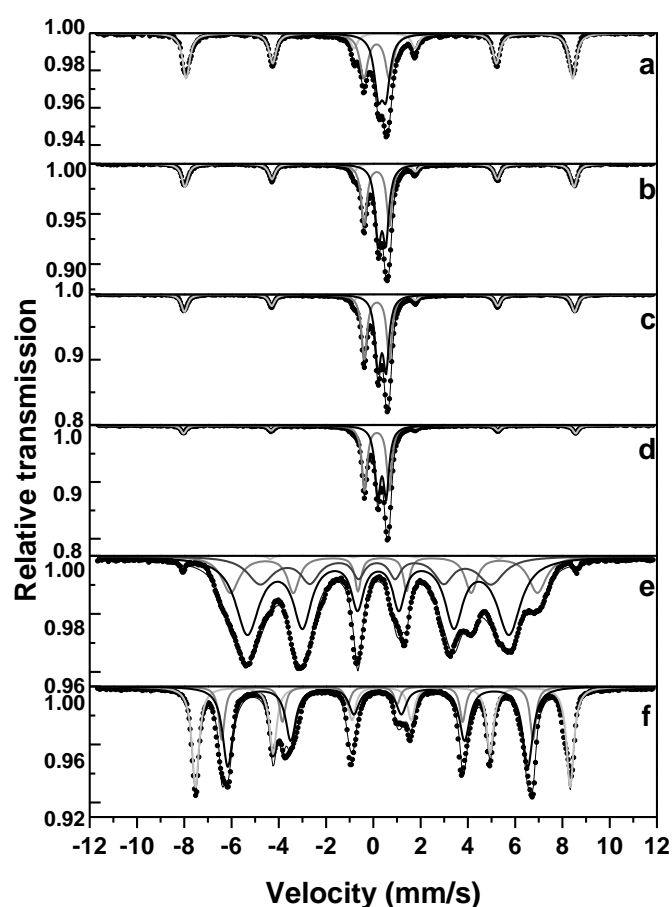
Figure 10.5. Mössbauer spectra of samples 3Y–4Al–1Fe–O (a), 3Y–3Al–2Fe–O (b), 3Y–2.5Al–2.5Fe–O (c), 3Y–2Al–3Fe–O (d), 3Y–1Al–4Fe–O (e), and 3Y–5Fe–O (f) precursor gels annealed at 1000 °C for 10 h.

According to Mössbauer spectroscopy data, first four samples with the composition of $Y_3Al_{5-x}Fe_xO_{12}$, ($x = 1.0$, 2.0, 2.5, 3.0) are almost identical and

their spectra are composed of three subspectra. Two doublets correspond to the nonordered (paramagnetic) iron phase, but from Mössbauer spectra it is not possible to say which one. These two doublets could be associated with iron ions at both sublattice of garnet structure [200], as the XRD patterns of these samples revealed garnet phase as dominant. While sextet belongs to a hematite (α-Fe_2O_3) in these samples, α is the phase of hematite, for the other samples, fitted magnetic sextets correspond to Fe^{3+} ions in octahedral sites (16a) and another corresponds to Fe^{3+} ions in the tetrahedral (24d) sites. Table 10.1 summarizes the fitting parameters.

The relative area of subspectra S shows the relative amount of the phase in the sample considering the Mössbauer effect probabilities for the phases. Obviously, the highest amount of side phase hematite (α-Fe_2O_3) could be seen in the sample $Y_3Al_4Fe_1O_{12}$, while in the other samples less side phase is formed or pure $Y_3Fe_5O_{12}$ was obtained. These results are in agreement with the results obtained from XRD measurements. As for other lanthanide iron garnets discussed before, the difference in isomer shift and hyperfine magnetic field is also due to nonequivalent octahedral and tetrahedral positions in the garnet structure. Trivalent iron ions with octahedral coordination have a less quadrupole splitting and larger isomeric shift than with tetrahedral coordination (Table 10.1). For YIG, the magnetic hyperfine fields are found to be around 49 T for a sites and 39 T for d sites and correspond to those reported before [172, 174].

Curie temperature with adapted thermogravimeter was determined only for $Y_3Fe_5O_{12}$ and $Y_3Al_1Fe_4O_{12}$ garnets obtained at 1000 °C. Measured Curie temperature for $Y_3Fe_5O_{12}$ was 282.1 °C and for $Y_3Al_1Fe_4O_{12}$ was 137.1 °C, showing the tendency to decrease with increasing amount of aluminium. These results coincide with the ones obtained from Mössbauer spectroscopy data and confirm paramagnetic behaviour of other samples.

Table 10.1. Data from Mössbauer spectra measured at room temperature: S is the relative area of subspectrum, Γ, δ, 2ε, B are line width, isomer shift, quadrupole splitting, and hyperfine field, respectively.

Sample	S, %	Γ, mm/s	δ, mm/s	2ε, mm/s	B, T	
3Y–4Al–1Fe–O	45	0.37	0.37	-0.22	50.8	α-Fe_2O_3
	30	0.41	0.37	0.32	N/A	Fe^{3+} in paramagnetic compound (possible a site in garnet)
	25	0.41	0.14	1.08	N/A	Fe^{3+} in paramagnetic compound (possible d site in garnet)
3Y–3Al–2Fe–O	27	0.32	0.37	-0.22	51.1	α-Fe_2O_3
	40	0.31	0.37	0.32	N/A	Fe^{3+} in paramagnetic compound (possible a site in garnet)
	33	0.29	0.15	1.07	N/A	Fe^{3+} in paramagnetic compound (possible d site in garnet)
3Y–2.5Al–2.5Fe–O	22	0.31	0.37	-0.22	51.3	α-Fe_2O_3
	41	0.29	0.37	0.34	N/A	Fe^{3+} in paramagnetic compound (possible a site in garnet)
	37	0.28	0.15	1.07	N/A	Fe^{3+} in paramagnetic compound (possible d site in garnet)
3Y–2Al–3Fe–O	11	0.27	0.37	-0.21	51.5	α-Fe_2O_3
	47	0.28	0.37	0.36	N/A	Fe^{3+} in paramagnetic compound (possible a site in garnet)
	42	0.27	0.15	1.05	N/A	Fe^{3+} in paramagnetic compound (possible d site in garnet)
3Y–1Al–4Fe–O	1	0.28	0.37	-0.20	51.8	α-Fe_2O_3
	18	Dist (B_{Hf})= 4.3 T	0.41	0.07	40.4	Fe^{3+} in a site in garnet
	50	Dist (B_{Hf})= 4.3 T	0.21	0.00	34.4	Fe^{3+} in d site in garnet
	31	Dist (B_{Hf})= 4.3 T	0.12	0.05	30.3	Fe^{3+} in d site in garnet
3Y–5Fe–O	39	0.37	0.38	0.05	49.2	Fe^{3+} in a site in garnet
	17	0.29	0.07	0.20	40.9	Fe^{3+} in d site in garnet
	44	0.52	0.19	0.01	39.4	Fe^{3+} in d site in garnet

10.2. Sol-Gel Synthesis and Characterization of $Y_3Al_{5-x}Fe_xO_{12}$ thin films

XRD and Mössbauer spectroscopy measurements of mixed-metal YAIG powders revealed that the lowest amount of side phases was obtained in the samples 3Y–2Al–3Fe–O, 3Y–1Al–4Fe–O, 3Y–5Fe–O, and 3Y–5Al–O. Therefore, the sols of these compositions were used for the preparation of thin films. Figure 10.6 presents XRD patterns of sol-gel derived coatings obtained from 3Y–5Al–O, 3Y–2Al–3Fe–O, 3Y–1Al–4Fe–O, and 3Y–5Fe–O solutions on Si substrate by dip-coating technique.
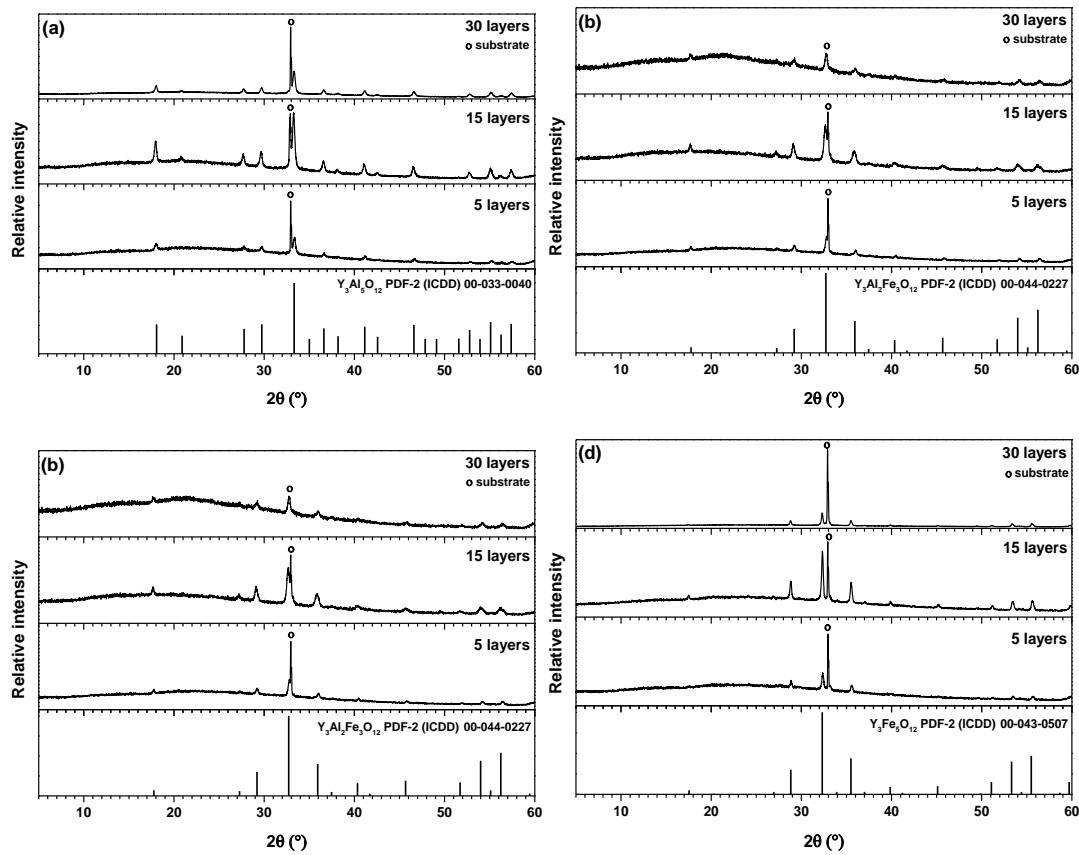
Figure 10.6. XRD patterns of sol-gel derived $Y_3Al_5O_{12}$ (a), $Y_3Al_2Fe_3O_{12}$ (b), $Y_3Al_1Fe_4O_{12}$ (c), and $Y_3Fe_5O_{12}$ (d) films on Si substrate.

Evidently, all the obtained XRD patterns reveal the formation of the desirable garnet phase on the Si substrate. In most cases, the XRD patterns of coatings gained after 15 dip-coating procedures contain reflections with a higher intensity than, in comparison, after 30 times of immersing. The peak of preferable phase after five layers is much lower compared to the 15-layer films.

It can be concluded that the optimal number of layers to fabricate high-quality mixed-metal YAIG films on Si substrate is between 15 and 30.

Figure 10.7a–d presents the SEM micrographs of $Y_3Al_{5-x}Fe_xO_{12}$, ($x = 0$, 3.0, 4.0, 5.0) films obtained on Si substrate after 30 dipping procedures.
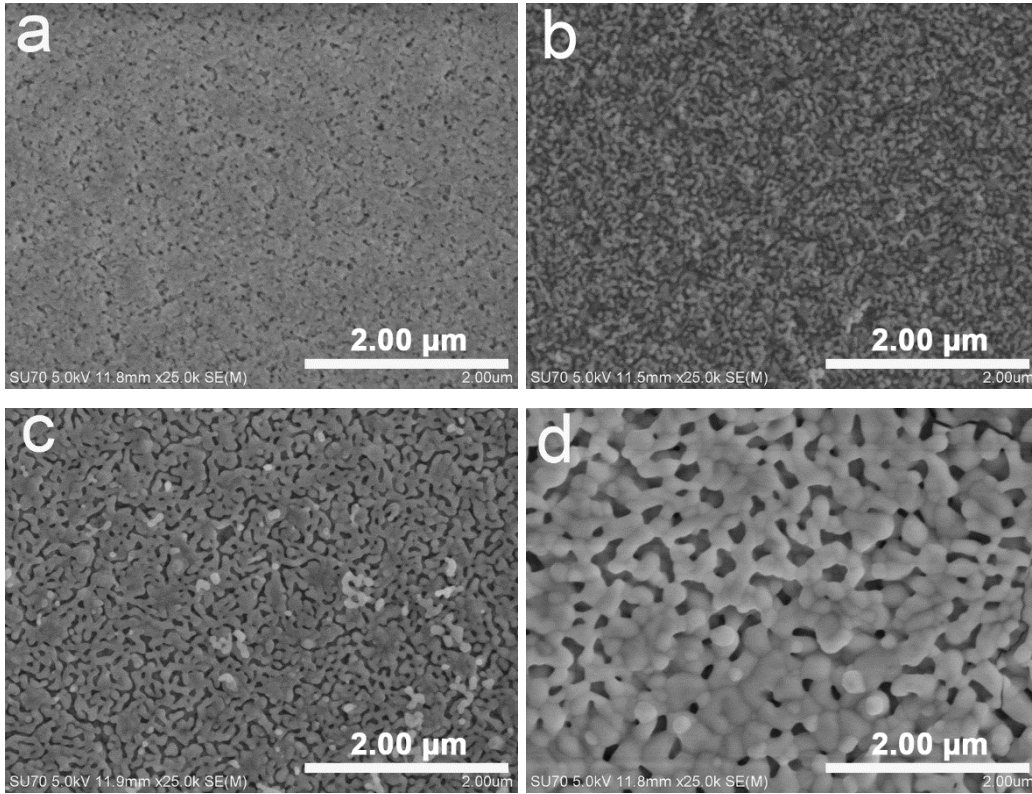
Figure 10.7. SEM micrographs of thin films on Si substrate containing 30 layers of $Y_3Al_5O_{12}$ (a), $Y_3Al_2Fe_3O_{12}$ (b), $Y_3Al_1Fe_4O_{12}$ (c), and $Y_3Fe_5O_{12}$ (d).

Again, the pronounced morphological features of $Y_3Al_{5-x}Fe_xO_{12}$ are very dependent on the chemical composition of mixed-metal garnet. Clearly, the surfaces of $Y_3Al_5O_{12}$ and $Y_3Al_2Fe_3O_{12}$ are highly dense (Figure 10.7a, b), while samples containing more iron in the composition revealed higher porosity of the surface (Figure 10.7c, d). Moreover, the coatings of $Y_3Al_1Fe_4O_{12}$ and $Y_3Fe_5O_{12}$ are composed of larger particles. The surface of the coatings is very homogeneous with evenly distributed particle size. The $Y_3Fe_{3.8}Al_{1.2}O_{12}$ coatings prepared by atmospheric plasma-spraying method demonstrated a dense structure with scattered microvoids. What is more, in some places, the surface was smoother while in some rougher, showing that some preparation parameters

have to be improved [143]. Interestingly, the particles of $Y_3Fe_5O_{12}$ films are found to be approximately 200 nm in size or even less, while for the bulk sample the particles less than 1 μm in size have formed. The $Y_3Al_1Fe_4O_{12}$ thin film is composed of elongated particles with less than 100 nm in size, whereas powder sample contains bigger particles. The surfaces of $Y_3Al_5O_{12}$ and $Y_3Al_2Fe_3O_{12}$ are composed of even particles around 50 nm or even smaller.

Chapter 11. Conclusions

1. The single-phase iron(III) oxide (Fe_2O_3) pigments were synthesized using an aqueous sol-gel method in the temperature range of 500–1000 °C. It was demonstrated, that the desirable colour of pigment could be obtained by changing annealing temperature of sol-gel derived precursor. High quality glazes having red/violet shades were obtained at 1000 °C using sol-gel derived Fe_2O_3 pigments.

2. New lanthanide iron-based oxide $Ln_3Fe_5O_{12}$ and $LnFeO_3$ (Ln = Ce, Pr, Nd, Tb) pigments have been synthesized using an aqueous sol-gel processing route. However, only two single-phase compounds $Tb_3Fe_5O_{12}$ and $PrFeO_3$ were prepared by this synthetic approach. High quality glaze was obtained at 1000 °C using sol-gel derived $Tb_3Fe_5O_{12}$ as the ceramic pigment. This pigment had the lowest value of parameter a^*, however, the prepared glaze showed the highest redness.

3. It was demonstrated for the first time, that the nature and amount of complexing agents (glycerol and 1,2-ethanediol) used in the sol-gel process influenced the formation and microstructural properties of the $Tb_3Fe_5O_{12}$ and $Y_3Fe_5O_{12}$ garnets. Monophasic $Y_3Fe_5O_{12}$ was synthesized using ethylene glycol at 1000 °C, while almost single-phase $Tb_3Fe_5O_{12}$ can be produced using both complexing agents with the molar ratio 1:1 to the total metal ions in the temperature range of 800–1000 °C.

4. The formation of monophasic holmium iron garnet during an aqueous sol-gel processing was investigated by combined TG–GC–MS analysis. It was shown that Ho–Fe–O precursor gel has been formed through intermediate coordination compounds.

5. It was demonstrated that the final sintering temperature to obtain monophasic lanthanide garnets is slightly different for different lanthanides. In the group of these compounds it was clearly seen, that the temperature of crystallization of $Ln_3Fe_5O_{12}$ is changing from 1000 °C to 800 °C in the sequence of lanthanides from Sm^{3+} to Lu^{3+}.

6. Magnetization measurements revealed, that magnetic properties of synthesized rare earth iron garnet samples depend on the composition and particle size, and could be successfully controlled by changing the synthesis parameters. Curie temperature for the series of sol-gel chemistry derived rare earth iron garnets was also determined. It was shown that Curie temperature monotonically decreased in the series from Sm^{3+} to Lu^{3+}.

7. Mixed-metal $Y_3Al_{5-x}Fe_xO_{12}$ (YAIG) garnets have been prepared by an aqueous sol-gel method in the whole substitution range. The monophasic $Y_3Al_5O_{12}$ and $Y_3Fe_5O_{12}$ garnets were obtained at 1000 °C. Interestingly, contrary to nonsubstituted $Y_3Al_5O_{12}$ and $Y_3Fe_5O_{12}$, the mixed-metal garnets $Y_3Al_{5-x}Fe_xO_{12}$ have already formed after the first stage of annealing of Y−Al−Fe−O precursor gels at 800 °C.

8. SEM micrographs showed that the particle size of $Y_3Al_{5-x}Fe_xO_{12}$ solids monotonically increased with increasing amount of iron in the garnet structure. Mössbauer spectroscopy showed more pronounced paramagnetic properties of materials with less iron content in the composition.

9. An aqueous sol-gel processing using dip-coating technique was successfully developed to fabricate $Y_3Al_{5-x}Fe_xO_{12}$ thin films on the Si substrate. The optimal number of layers to fabricate high quality mixed-metal YAIG films on Si substrate is between 15 and 30.

Chapter 12. List of Publications and Conference Participation

12.1. Publications Included in the Thesis

12.1.1. Articles in Journals

1. O. Opuchovic, D. Niznansky, A. Kareiva. Thermoanalytical (TG/DSC/EVG–GC–MS) characterization of the lanthanide (Ho) iron garnet formation in sol-gel. *Journal of Thermal Analysis and Calorimetry*, 130 (2017) 1085–1094.

2. O. Opuchovic, S. Culunlu, A. U. Morkan, I. A. Morkan, D. Niznansky, E. Garskaite, A. Beganskiene, A. Kareiva. Structural, morphological and magnetic characterization of bulk and thin films $Y_3Al_{5-x}Fe_xO_{12}$ (YAIG): From the Perspective of Aqueous Sol-Gel Processing. *Chemical Engineering Communications*, 204 (2017) 1037–1048.

3. O. Opuchovic, A. Kareiva, K. Mazeika, D. Baltrunas. Magnetic nanosized rare earth iron garnets $R_3Fe_5O_{12}$: Sol-gel fabrication, characterization and reinspection. *Journal of Magnetism and Magnetic Materials*, 422 (2017) 425–433.

4. O. Opuchovic, A. Beganskiene, A. Kareiva. Sol-gel derived $Tb_3Fe_5O_{12}$ and $Y_3Fe_5O_{12}$ garnets: synthesis, phase purity, micro-structure and improved design of morphology. *Journal of Alloys and Compounds*, 647 (2015) 189–197.

5. O. Opuchovic, G. Kreiza, J. Senvaitiene, K. Kazlauskas, A. Beganskiene, A. Kareiva. Sol-gel synthesis, characterization and application of selected sub-microsized lanthanide (Ce, Pr, Nd, Tb) ferrites. *Dyes and Pigments*, 118 (2015) 176–182.

6. O. Opuchovic, A. Kareiva. Historical hematite pigment: Synthesis by an aqueous sol-gel method, characterization and application for the colouration of ceramic glazes. *Ceramics International*, 41 (2015) 4504–4513.

12.1.2. Attended Conferences

1. O. Opuchovic, A. Beganskiene, A. Kareiva. Curie temperature determination of rare earth iron garnets. *There is no Future without the Past*, 28–30 July, 2017, Vilnius, Lithuania.

2. O. Opuchovic, D. Niznansky, A. Kareiva. Investigation of holmium iron garnet formation process by TG–GC–MS. *1st Journal of Thermal Analysis and Calorimetry Conference and 6th V4 (Joint Czech-Hungarian-Polish-Slovakian) Thermoanalytical Conference*, 6–9 June 2017, Budapest, Hungary.

3. O. Opuchovic, S. Culunlu, A. U. Morkan, I. A. Morkan, D. Niznansky, A. Kareiva. Mössbauer Spectroscopy for Mixed-Metal Yttrium Aluminium-Iron Garnets. *Chemistry and Chemical Technology 2016*, 28–29 April, 2016, Vilnius, Lithuania.

4. O. Opuchovic, A. Kareiva, K. Mazeika, D. Baltrunas. Formation, Characterization and Application of Lanthanide Mixed-Metal Ferrites. *COST Action MP1202. Nanostructured materials: Protective and Functional coatings, surface treatment, bioceramics biocomposites and membranes*, 14–16 March, 2016, Vilnius, Lithuania.

5. O. Opuchovič, A. Kareiva, K. Mažeika, D. Baltrūnas. Daugiafunkcinės neorganinės medžiagos: retųjų žemių elementų feratų formavimas, savybių valdymas ir taikymai. *Šeštoji jaunųjų mokslininkų konferencija „Fizinių ir technologijos mokslų tarpdalykiniai tyrimai"*, 10 February, 2016, Vilnius, Lithuania.

6. S. Culunlu, O. Opuchovic, A. U. Morkan, I. A. Morkan, A. Beganskiene, A. Kareiva. Magnetic Properties of Mixed-Metal Yttrium Aluminium-Iron Garnets. *Nanochemistry and Nanomaterials 2015*, 22–24 October, 2015, Vilnius, Lithuania.

7. O. Opuchovic. Sol-gel synthesis and characterization of garnet structure compounds $R_3Fe_5O_{12}$ (R = Sm, Eu, Gd, Tb, Dy, Ho, Er, Tm, Yb, Lu). *Nanochemistry and Nanomaterials 2015*, 22–24 October, 2015, Vilnius, Lithuania.

8. O. Opuchovic, A. Kareiva. Impact of complexing agent for the sol-gel synthesis of yttrium and terbium iron garnets. *XVIII International Sol-Gel Conference: Sol-Gel 2015*, 6–11 September, 2015, Kyoto, Japan.

9. O. Opuchovic, G. Kreiza, K. Kazlauskas, A. Kareiva. Neodymium, Terbium, Prazeodymium and Cerium Iron Garnets and Orthoferrites: A New Class of Pigments? *Chemistry and Chemical Technology 2015*, 23 January, 2015, Vilnius, Lithuania.

10. O. Opuchovic, D. J. Jasaitis, A. Kareiva. Peculiarity of the usage of red ochre for the preparation of ceramic glazes. *EcoBalt 2013: 18th international scientific conference*, 25–27 October, 2013, Vilnius, Lithuania.

11. O. Opuchovic, A. Beganskiene, A. Kareiva. Sol-gel synthesis of neodymium, terbium, praseodymium and cerium iron garnets and orthoferrites. *NANOAPP: International Scientific Conference on Nanomaterials and Application*, 22–26 September, 2013, Portorož, Slovenia.

12.2. Publications Not Included in the Thesis

12.2.1. Articles in Journals

1. T. Petrenas, O. Opuchovic, J. Senvaitiene, A. Beganskiene, A. Kareiva. A novel polymeric conservation method of historical outdoor ceramics. *Materials Science (Medžiagotyra),* 21 (2015) 293–297.

2. T. Petrenas, O. Opuchovic, A. Beganskiene, A. Kareiva. Possible conservation routes to the historical outdoor ceramics. *REHAB 2014: Proceedings of the international conference on preservation, maintenance and rehabilitation of historical buildings and structures, Tomar, Portugal 19–21 March / Edited by Rogério Am.*, (2014) 1099–1105.

3. E. Raudonyte, H. Bettentrup, D. Uhlich, S. Sakirzanovas, O. Opuchovic, S. Tautkus, A. Katelnikovas. On the $Ce^{3+} \rightarrow Cr^{3+}$ energy transfer in $Lu_3Al_5O_{12}$ garnets. *Optical materials*, 37 (2014) 204–210.

4. T. Petrenas, J. Kiuberis, O. Opuchovic, S. Tautkus, A. Kareiva. A closer look at the ancient bricks of historical monuments: Essential step for the conservation of pottery. *Chemija*, 23 (2012) 194–202.

12.2.2. Attended Conferences

1. O. Opuchovic. Combinatorial synthesis for magnetic materials. *Inovatyvioji ir tvarioji chemija*, 9–10 December, 2016, Puvočiai, Varėnos raj., Lithuania.

2. T. Petrenas, O. Opuchovic, A. Beganskiene, A. Kareiva. Possible conservation routes to the historical outdoor ceramics. *REHAB 2014: International conference on preservation, maintenance and rehabilitation of historical buildings and structures*, 19–21 March, 2014, Tomar, Portugal.

3. T. Petrenas, O. Opuchovic, R. Raudonis, A. Beganskiene, A. Kareiva. New methods for the conservation of historical ceramics: investigation of morphology and surface properties. *Chemistry, physics and technology surface: proceedings of Ukrainian conference with international participation*, 15–17 May, 2013, Kyiv, Ukraine.

4. O. Opuchovic, T. Petrenas. The development of new methods for the conservation of historical ceramics. *Nanochemistry and nanomaterials: international conference of young chemists*, 7–9 December, 2012, Palanga, Lithuania.

5. O. Opuchovic, T. Petrenas, A. Kareiva. Naujų keramikos konservavimo metodų kūrimas. *Chemija ir cheminė technologija: studentų mokslinė konferencija*, 15 May, 2012, Klaipėda, Lithuania.

Acknowledgements

References

[1]   D. Hradil, T. Grygar, J. Hradilová, P. Bezdička, Applied Clay Science, 22 (2003) 223-236.

[2]   J.R. Barnett, S. Miller, E. Pearce, Optics & Laser Technology, 38 (2006) 445-453.

[3]   Ü. Özgür, Y. Alivov, H. Morkoç, Journal of Materials Science: Materials in Electronics, 20 (2009) 911-952.

[4]   M.H. Aly, I.S. Ismael, F. Bondioli, Cerâmica, 56 (2010) 156-161.

[5]   D. Bagdzevičienė, L. Kruopaitė, Pigmentai ir dažikliai restauruojant kultūros vertybes, Savastis, Vilnius, 2005.

[6]   Y. Marinova, J.M. Hohemberger, E. Cordoncillo, P. Escribano, J.B. Carda, Journal of the European Ceramic Society, 23 (2003) 213-220.

[7]   M.G.B. Nunes, L.S. Cavalcante, V. Santos, J.C. Sczancoski, M.R.M.C. Santos, L.S. Santos-Júnior, E. Longo, Journal of Sol-Gel Science and Technology, 47 (2008) 38-43.

[8]   M.F.R. Fouda, M.B. El-Kholy, S.A. Moustafa, A.I. Hussien, M.A. Wahba, M.F. El-Shahat, International Journal of Inorganic Chemistry, 2012 (2012) 1-9.

[9]   S.F. Santos, M.C. de Andrade, J.A. Sampaio, A.B. da Luz, T. Ogasawara, Dyes and Pigments, 75 (2007) 574-579.

[10]   L. Sandhya Kumari, P. Prabhakar Rao, M. Lakshmipathy Reddy, Journal of Alloys and Compounds, 461 (2008) 509-515.

[11]   R.C. Olegário, E.C. Ferreira de Souza, J.F. Marcelino Borges, J.B. Marimon da Cunha, A.V. Chaves de Andrade, S.R. Masetto Antunes, A.C. Antunes, Dyes and Pigments, 97 (2013) 113-117.

[12]   V. James, P. Prabhakar Rao, S. Sameera, S. Divya, Ceramics International, 40 (2014) 2229-2235.

[13]   J.D. Cunha, D.M.A. Melo, A.E. Martinelli, M.A.F. Melo, I. Maia, S.D. Cunha, Dyes and Pigments, 65 (2005) 11-14.

[14]   Ž. Dohnalová, P. Šulcová, M. Trojan, Journal of Thermal Analysis and Calorimetry, 91 (2008) 559-563.

[15]   P.C. Piña, R. Buentello, H. Arriola, E.N. Nava, Hyperfine Interactions, 185 (2008) 173-177.

[16]   C. Piña, H. Arriola, N. Nava, Journal of Physics: Conference Series, 217 (2010) 012036.

[17]   A. Gatelyte, J. Senvaitiene, D. Jasaitis, A. Beganskiene, A. Kareiva, Chemija, 22 (2011) 19-24.

[18]   D. Jonynaitė, PhD Thesis, Vilnius University, Vilnius, Lithuania, 2011.

[19]   J. Zou, P. Zhang, C. Liu, Y. Peng, Dyes and Pigments, 109 (2014) 113-119.

[20]   Ž. Dohnalová, M. Vontorčíková, P. Šulcová, Journal of Thermal Analysis and Calorimetry, 113 (2013) 1223-1229.

[21]   N.C. Pramanik, T.I. Bhuiyan, M. Nakanishi, T. Fujii, J. Takada, S.I. Seok, Materials Letters, 59 (2005) 3783-3787.

[22]   J.M.D. Coey, Magnetism and magnetic materials, Cambridge University Press, New York, 2009.

[23]   M. Sugimoto, Journal of the American Ceramic Society, 82 (1999) 269-280.

[24]   C. Suchomski, C. Reitz, D. Pajic, Z. Jaglicic, I. Djerdj, T. Brezesinski, Chemistry of Materials, 26 (2014) 2337-2343.

[25]   Ü. Özgür, Y. Alivov, H. Morkoç, Journal of Materials Science: Materials in Electronics, 20 (2009) 789-834.

[26]   M.N. Akhtar, M.A. Khan, M. Ahmad, G. Murtaza, R. Raza, S.F. Shaukat, M.H. Asif, N. Nasir, G. Abbas, M.S. Nazir, M.R. Raza, Journal of Magnetism and Magnetic Materials, 368 (2014) 393-400.

[27]   C. Suchomski, C. Reitz, C.T. Sousa, J.P. Araujo, T. Brezesinski, Chemistry of Materials, 25 (2013) 2527-2537.

[28]   M. Elias, C. Chartier, G. Prévot, H. Garay, C. Vignaud, Materials Science and Engineering: B, 127 (2006) 70-80.

[29]   G. Buxbaum, Industrial Inorganic Pigments, Wiley-VCH, New York, 1998.

[30] F.Q. Mariani, K.W. Borth, M. Müller, M. Dalpasquale, F.J. Anaissi, Dyes and Pigments, 137 (2017) 403-409.

[31] Erella Hovers, Shimon Ilani, Ofer Bar-Yosef, Bernard Vandermeersch, Current Anthropology, 44 (2003) 491-522.

[32] J.L. Mortimore, L.-J.R. Marshall, M.J. Almond, P. Hollins, W. Matthews, Spectrochimica Acta Part A: Molecular and Biomolecular Spectroscopy, 60 (2004) 1179-1188.

[33] E. Iriarte, A. Foyo, M.A. Sánchez, C. Tomillo, J. Setién, Archaeometry, 51 (2009) 231-251.

[34] R.J.H. Clark, M.L. Curri, Journal of Molecular Structure, 440 (1998) 105-111.

[35] J. Capel, F. Huertas, A. Pozzuoli, J. Linares, Journal of Archaeological Science, 33 (2006) 1157-1166.

[36] A. Zucchiatti, P. Prati, A. Bouquillon, L. Giuntini, M. Massi, A. Migliori, A. Cagnana, S. Roascio, Nuclear Instruments and Methods in Physics Research Section B: Beam Interactions with Materials and Atoms, 219–220 (2004) 20-25.

[37] L.-J.R. Marshall, J.R. Williams, M.J. Almond, S.D.M. Atkinson, S.R. Cook, W. Matthews, J.L. Mortimore, Spectrochimica Acta Part A: Molecular and Biomolecular Spectroscopy, 61 (2005) 233-241.

[38] A.M. Zipkin, S.H. Ambrose, J.M. Hanchar, P.M. Piccoli, A.S. Brooks, E.Y. Anthony, Quaternary International, 430 (2017) 42-59.

[39] D. Bikiaris, S. Daniilia, S. Sotiropoulou, O. Katsimbiri, E. Pavlidou, A.P. Moutsatsou, Y. Chryssoulakis, Spectrochimica Acta Part A: Molecular and Biomolecular Spectroscopy, 56 (2000) 3-18.

[40] R.M. Cornell, U. Schwertmann, The Iron Oxides, Structure, Properties, Reactions, Occurrence and Uses, Wiley-VCH, Weinheim, 2003.

[41] C. Montagner, D. Sanches, J. Pedroso, M.J. Melo, M. Vilarigues, Spectrochimica Acta Part A: Molecular and Biomolecular Spectroscopy, 103 (2013) 409-416.

[42] E. Cheilakou, M. Troullinos, M. Koui, Journal of Archaeological Science, 41 (2014) 541-555.

[43] K. Helwig, Studies in Conservation, 42 (1997) 181-188.

[44] D. Walter, Thermochimica Acta, 445 (2006) 195-199.

[45] N. Pailhé, A. Wattiaux, M. Gaudon, A. Demourgues, Journal of Solid State Chemistry, 181 (2008) 2697-2704.

[46] N. Pailhé, A. Wattiaux, M. Gaudon, A. Demourgues, Journal of Solid State Chemistry, 181 (2008) 1040-1047.

[47] E. Esmaeili, M. Salavati-Niasari, F. Mohandes, F. Davar, H. Seyghalkar, Chemical Engineering Journal, 170 (2011) 278-285.

[48] L. Hu, A. Percheron, D. Chaumont, C.-H. Brachais, Journal of Sol-Gel Science and Technology, 60 (2011) 198-205.

[49] Y. Wu, X. Wang, Materials Letters, 65 (2011) 2062-2065.

[50] J. Wang, W.B. White, J.H. Adair, Journal of the American Ceramic Society, 88 (2005) 3449-3454.

[51] L. Chen, X. Yang, J. Chen, J. Liu, H. Wu, H. Zhan, C. Liang, M. Wu, Inorganic Chemistry, 49 (2010) 8411-8420.

[52] Y.P. He, Y.M. Miao, C.R. Li, S.Q. Wang, L. Cao, S.S. Xie, G.Z. Yang, B.S. Zou, C. Burda, Physical Review B, 71 (2005) 125411.

[53] D.M. Sherman, T.D. Waite, American Mineralogist, 70 (1985) 1262-1269.

[54] R.L. Blake, R.E. Hessevick, T. Zoltai, L.W. Finger, The American Mineralogist, 51 (1966) 123-129.

[55] J. Torrent, V. Barrón, Encyclopedia of Surface and Colloid Science, Third Edition, CRC Press, 2015.

[56] I.C.O. Illumination, Recommendations on Uniform Color Spaces, Color-difference Equations, Psychometric Color Terms, CIE, 1978.

[57] A. Hunt, P. Thomas, D. James, B. David, J.-M. Geneste, J.-J. Delannoy, B. Stuart, Microchemical Journal, 126 (2016) 524-529.

[58] A. Casanova Municchia, M. Micheli, M.A. Ricci, M. Toledo, F. Bellatreccia, S. Lo Mastro, A. Sodo, Spectrochimica Acta Part A: Molecular and Biomolecular Spectroscopy, 156 (2016) 47-53.

[59] P.C. Gutiérrez-Neira, F. Agulló-Rueda, A. Climent-Font, C. Garrido, Vibrational Spectroscopy, 69 (2013) 13-20.

[60] M. Müller, J.C. Villalba, F.Q. Mariani, M. Dalpasquale, M.Z. Lemos, M.F. Gonzalez Huila, F.J. Anaissi, Dyes and Pigments, 120 (2015) 271-278.

[61] Z. Čermáková, S. Švarcová, J. Hradilová, P. Bezdička, A. Lančok, V. Vašutová, J. Blažek, D. Hradil, Spectrochimica Acta Part A: Molecular and Biomolecular Spectroscopy, 140 (2015) 101-110.

[62] B. Constantinescu, R. Bugoi, E. Pantos, D.N. Popovici, Documenta Praehistorica, 34 (2007) 281-288.

[63] V. Rusanov, K. Chakarova, H. Winkler, A.X. Trautwein, Dyes and Pigments, 81 (2009) 254-258.

[64] D. Hradil, T. Grygar, M. Hrušková, P. Bezdička, K. Lang, O. Schneeweiss, M. Chvátal, Clays and Clay Minerals, 52 (2004) 767-778.

[65] J.L. Perez-Rodriguez, M.d.C.J. de Haro, B. Siguenza, J.M. Martinez-Blanes, Applied Clay Science, 116–117 (2015) 211-219.

[66] I. Aliatis, D. Bersani, E. Campani, A. Casoli, P.P. Lottici, S. Mantovan, I.-G. Marino, F. Ospitali, Spectrochimica Acta Part A: Molecular and Biomolecular Spectroscopy, 73 (2009) 532-538.

[67] C.P. Aby, K.J. Sreeram, B.U. Nair, T. Ramasami, Coloration Technology, 123 (2007) 374-378.

[68] J. Luxová, P. Šulcová, M. Trojan, Thermochimica Acta, 579 (2014) 80-85.

[69] L. Liu, A. Han, M. Ye, M. Zhao, Solar Energy Materials and Solar Cells, 132 (2015) 377-384.

[70] F.G. Maranha, T.E.R. Fiuza, E.C.F.d. Souza, J.F.M. Borges, J.B.M.d. Cunha, A.V.C.d. Andrade, S.R.M. Antunes, A.C. Antunes, Dyes and Pigments, 133 (2016) 304-310.

[71]   Ž. Dohnalová, P. Šulcová, M. Trojan, Dyes and Pigments, 80 (2009) 22-25.

[72]   M. Jovaní, A. Sanz, H. Beltrán-Mir, E. Cordoncillo, Dyes and Pigments, 133 (2016) 33-40.

[73]   L. Samain, F. Grandjean, G.J. Long, P. Martinetto, P. Bordet, J. Sanyova, D. Strivay, Journal of Synchrotron Radiation, 20 (2013) 460-473.

[74]   M. Ware, Journal of Chemical Education, 85 (2008) 612.

[75]   M. Bacci, D. Magrini, M. Picollo, M. Vervat, Journal of Cultural Heritage, 10 (2009) 275-280.

[76]   I. Arrizabalaga, O. Gómez-Laserna, J. Aramendia, G. Arana, J.M. Madariaga, Spectrochimica Acta Part A: Molecular and Biomolecular Spectroscopy, 124 (2014) 308-314.

[77]   G.N. Maslennikova, Glass and Ceramics, 58 (2001) 216-220.

[78]   P.N. Medeiros, Y.F. Gomes, M.R.D. Bomio, I.M.G. Santos, M.R.S. Silva, C.A. Paskocimas, M.S. Li, F.V. Motta, Journal of Advanced Ceramics, 4 (2015) 135-141.

[79]   C.S. Xavier, R.A. Candeia, M.I.B. Bernardi, S.J.G. Lima, E. Longo, C.A. Paskocimas, L.E.B. Soledade, A.G. Souza, I.M.G. Santos, Journal of Thermal Analysis and Calorimetry, 87 (2007) 709-713.

[80]   A. Gatelyte, PhD Thesis, Vilnius University, Vilnius, Lithuania, 2012.

[81]   M. Dondi, C. Zanelli, M. Ardit, G. Cruciani, L. Mantovani, M. Tribaudino, G.B. Andreozzi, Ceramics International, 39 (2013) 9533-9547.

[82]   W. Bao, F. Ma, Y. Zhang, X. Hao, Z. Deng, X. Zou, W. Gao, Powder Technology, 292 (2016) 7-13.

[83]   D.C. Jiles, Acta Materialia, 51 (2003) 5907-5939.

[84]   L.A. Dobrzański, M. Drak, B. Ziębowicz, Journal of Achievements in Materials and Manufacturing Engineering, 17 (2006) 37-40.

[85]   I.R. Harris, A.J. Williams, in: R.D. Rawlings (Ed.), Material Science and Engineering, Eolls Publishers, Oxford, 2009.

[86] G.I. Likhtenshtein, J. Yamauchi, S.i. Nakatsuji, A.I. Smirnov, R. Tamura, Nitroxides, Wiley-VCH Verlag GmbH & Co. KGaA, 2008.

[87] W.D. Callister, D.G. Rethwisch, Materials Science and Engineering: An Introduction, Wiley, 2013.

[88] M.E. McHenry, M.A. Willard, D.E. Laughlin, Progress in Materials Science, 44 (1999) 291-433.

[89] M.E. McHenry, D.E. Laughlin, Acta Materialia, 48 (2000) 223-238.

[90] R. Pauthenet, Journal of Applied Physics, 30 (1959) S290-S292.

[91] B.D. Cullity, C.D. Graham, Introduction to Magnetic Materials, Wiley, 2009.

[92] D.L. Leslie-Pelecky, R.D. Rieke, Chemistry of Materials, 8 (1996) 1770-1783.

[93] N.A. Spaldin, Magnetic Materials: Fundamentals and Applications, Cambridge University Press, Cambridge, 2010.

[94] C.G. Stefanita, From Bulk to Nano: The Many Sides of Magnetism, Springer Berlin Heidelberg, 2008.

[95] K.H.J. Buschow, F.R.D. Boer, Physics of magnetism and magnetic materials, Kluwer Academic/Plenum Publishers, New York, 2003.

[96] R.C. O'Handley, Modern Magnetic Materials: Principles and Applications, Wiley, 1999.

[97] F. Fiorillo, Characterization and Measurement of Magnetic Materials, Academic Press, San Diego, 2004.

[98] S. Watanabe, Y. Kuboki, Y. Hozumi, Fuji Electric Review, 57 (2011) 46-50.

[99] Y. Inaba, H. Nakata, D. Inoue, Fuji Electric Review, 57 (2011) 42-45.

[100] R.V. Ramanujan, in: R. Narayan (Ed.), Biomedical Materials, Springer US, Boston, MA, 2009.

[101] C.B. Catherine, S.G.C. Adam, Journal of Physics D: Applied Physics, 36 (2003) R198.

[102] M. Shinkai, Journal of Bioscience and Bioengineering, 94 (2002) 606-613.

[103] D. Bahadur, J. Giri, Sadhana, 28 (2003) 639-656.

[104] R.A. Revia, M. Zhang, Materials Today, 19 (2016) 157-168.

[105] B. Issa, I.M. Obaidat, B.A. Albiss, Y. Haik, International Journal of Molecular Sciences, 14 (2013) 21266-21305.

[106] P. Presa, Y. Luengo, M. Multigner, R. Costo, M.P. Morales, G. Rivero, A. Hernando, The Journal of Physical Chemistry C, 116 (2012) 25602-25610.

[107] G.F. Dionne, Journal of Applied Physics, 81 (1997) 5064-5069.

[108] T. Ramesh, R.S. Shinde, S.R. Murthy, Journal of Magnetism and Magnetic Materials, 324 (2012) 3668-3673.

[109] F. Bertaut, F. Forrat, Comptes Rendus de l'Academie des Sciences, 242 (1956) 382-384.

[110] S. Geller, M.A. Gilleo, Journal of Physics and Chemistry of Solids, 3 (1957) 30-36.

[111] G. Menzer, Z. Kristallogr., 63 (1926) 157-158.

[112] R. Valenzuela, Magnetic Ceramics, Cambridge University Press, Cambridge, 1994.

[113] M.A. Gilleo, S. Geller, Physical Review, 110 (1958) 73-78.

[114] F. Sayetat, Journal of Magnetism and Magnetic Materials, 58 (1986) 334-346.

[115] C.D.G. Soshin Chikazumi, Physics of Ferromagnetism, Oxford University Press, New York, 1997.

[116] R.L. Comstock, Introduction to Magnetism and Magnetic Recording, Wiley, 1999.

[117] D. Rodic, M. Mitric, R. Tellgren, H. Rundlof, Journal of Magnetism and Magnetic Materials, 232 (2001) 1-8.

[118] Z. Azadi Motlagh, M. Mozaffari, J. Amighian, Journal of Magnetism and Magnetic Materials, 321 (2009) 1980-1984.

[119] E.J.J. Mallmann, A.S.B. Sombra, J.C. Goes, P.B.A. Fechine, Solid State Phenomena, 202 (2013) 65-96.

[120] C.S. Kim, Y.R. Uhm, S.B. Kim, J.-G. Lee, Journal of Magnetism and Magnetic Materials, 215–216 (2000) 551-553.

[121] H. Xu, H. Yang, Physica Status Solidi (a), 204 (2007) 1203-1209.

[122] A. Seidel, L. Häggström, D. Rodić, Hyperfine Interactions, 73 (1992) 265-275.

[123] F. Grasset, S. Mornet, J. Etourneau, H. Haneda, J.L. Bobet, Journal of Alloys and Compounds, 359 (2003) 330-337.

[124] J.S. McCloy, B. Walsh, IEEE Transactions on Magnetics, 49 (2013) 4253-4256.

[125] V.R. Caffarena, T. Ogasawara, Materials Research, 6 (2003) 569-576.

[126] V.R. Caffarena, T. Ogasawara, M.S. Pinho, J.L. Capitaneo, Latin American Applied Research, 36 (2006) 137-140.

[127] D. Aoki, M. Shima, Japanese Journal of Applied Physics, 53 (2014) 113001.

[128] L. Guo, H.M. Yuan, K.K. Huang, L. Yuan, S.K. Liu, S.H. Feng, Chemical Research in Chinese Universities, 27 (2011) 715-719.

[129] P. Vaqueiro, M.A. Arturo López-Quintela, Chemistry of Materials, 9 (1997) 2836-2841.

[130] R.D. Sánchez, J. Rivas, P. Vaqueiro, M.A. López-Quintela, D. Caeiro, Journal of Magnetism and Magnetic Materials, 247 (2002) 92-98.

[131] Z. Cheng, H. Yang, Physica E: Low-dimensional Systems and Nanostructures, 39 (2007) 198-202.

[132] D.T.T. Nguyet, N.P. Duong, T. Satoh, L.N. Anh, T.D. Hien, Journal of Magnetism and Magnetic Materials, 332 (2013) 180-185.

[133] K. Praveena, S. Srinath, Journal of Magnetism and Magnetic Materials, 349 (2014) 45-50.

[134] L.N. Singh, Journal of Magnetism and Magnetic Materials, 272 (2004) 2244-2246.

[135] A.M. Kalashnikova, V.V. Pavlov, A.V. Kimel, A. Kirilyuk, T. Rasing, R.V. Pisarev, Low Temperature Physics, 38 (2012) 863-869.

[136] H. Yamahara, M. Mikami, M. Seki, H. Tabata, Journal of Magnetism and Magnetic Materials, 323 (2011) 3143-3146.

[137] K.J. Khan, F. Saleemi, T. Abbas, I. Sadiq, Journal of Ovonic Research, 11 (2016) 263-270.

[138] A.A. Sattar, H.M. Elsayed, A.M. Faramawy, Journal of Magnetism and Magnetic Materials, 412 (2016) 172-180.

[139] P.B.A. Fechine, E.N. Silva, A.S. de Menezes, J. Derov, J.W. Stewart, A.J. Drehman, I.F. Vasconcelos, A.P. Ayala, L.P. Cardoso, A.S.B. Sombra, Journal of Physics and Chemistry of Solids, 70 (2009) 202-209.

[140] X. Wu, X. Wang, Y. Liu, W. Cai, S. Peng, F. Huang, X. Lu, F. Yan, J. Zhu, Applied Physics Letters, 95 (2009) 182903.

[141] R. Tholkappiyan, K. Vishista, Applied Surface Science, 351 (2015) 1016-1024.

[142] C.S. Kim, B.K. Min, S.J. Kim, S.R. Yoon, Y.R. Uhm, Journal of Magnetism and Magnetic Materials, 254–255 (2003) 553-555.

[143] B.G. Ravi, X.Z. Guo, Q.Y. Yan, R.J. Gambino, S. Sampath, J.B. Parise, Surface and Coatings Technology, 201 (2007) 7597-7605.

[144] P.P.S. Ortega, R. Miguel Angel, F. César Renato, G. Filiberto González, C. Mario, S. Alexandre Zirpoli, Processing and Application of Ceramics, 8 (2014) 211-218.

[145] M. Zeng, Journal of Magnetism and Magnetic Materials, 393 (2015) 370-375.

[146] M. Pardavi-Horvath, Journal of Magnetism and Magnetic Materials, 215–216 (2000) 171-183.

[147] D. Cruickshank, Journal of the European Ceramic Society, 23 (2003) 2721-2726.

[148] R.C. Booth, E.A.D. White, Journal of Physics D: Applied Physics, 17 (1984) 579.

[149] G.-Y. Zhang, X.-W. Xu, T.-C. Chong, Journal of Applied Physics, 95 (2004) 5267-5270.

[150] Z.C. Xu, M. Yan, M. Li, Z.L. Zhang, M. Huang, Journal of Applied Physics, 101 (2007) 053910.

[151] M. Nur-E-Alam, M. Vasiliev, V. Kotov, K. Alameh, Procedia Engineering, 76 (2014) 61-73.

[152] M. Nur-E-Alam, M. Vasiliev, K. Alameh, V. Kotov, V. Demidov, D. Balabanov, Journal of Nanomaterials, 2015 (2015) 1-6.

[153] F. Grasset, S. Mornet, A. Demourgues, J. Portier, J. Bonnet, A. Vekris, E. Duguet, Journal of Magnetism and Magnetic Materials, 234 (2001) 409-418.

[154] A. Stupakiewicz, K. Szerenos, D. Afanasiev, A. Kirilyuk, A.V. Kimel, Nature, 542 (2017) 71-74.

[155] A. Beganskiene, R. Raudonis, A. Kareiva, Chemical Engineering Communications, 200 (2012) 305-315.

[156] E. Garskaite, M. Lindgren, M.-A. Einarsrud, T. Grande, Journal of the European Ceramic Society, 30 (2010) 1707-1715.

[157] Y. Wang, X. Jiang, Y. Xia, Journal of the American Chemical Society, 125 (2003) 16176-16177.

[158] T.P. Braga, D.F. Dias, M.F. de Sousa, J.M. Soares, J.M. Sasaki, Journal of Alloys and Compounds, 622 (2015) 408-417.

[159] J. Habjanič, M. Jurić, J. Popović, K. Molčanov, D. Pajić, Inorganic Chemistry, 53 (2014) 9633-9643.

[160] C. Reitz, C. Suchomski, V.S.K. Chakravadhanula, I. Djerdj, Z. Jagličić, T. Brezesinski, Inorganic Chemistry, 52 (2013) 3744-3754.

[161] B. Fleury, M.-A. Neouze, J.-M. Guigner, N. Menguy, O. Spalla, T. Gacoin, D. Carriere, ACS Nano, 8 (2014) 2602-2608.

[162] S. Hosseini Vajargah, H.R. Madaah Hosseini, Z.A. Nemati, Journal of Alloys and Compounds, 430 (2007) 339-343.

[163] D.T. Phan, A.A.M. Farag, F. Yakuphanoglu, G.S. Chung, Journal of Electroceramics, 29 (2012) 12-22.

[164] M. Milde, S. Dembski, A. Osvet, M. Batentschuk, A. Winnacker, G. Sextl, Materials Chemistry and Physics, 148 (2014) 1055-1063.

[165] J. Farjas, J. Camps, P. Roura, S. Ricart, T. Puig, X. Obradors, Thermochimica Acta, 521 (2011) 84-89.

[166] F. Ribot, P. Toledano, C. Sanchez, Inorganica Chimica Acta, 185 (1991) 239-245.

[167] T. Arun, M. Vairavel, S. G. Raj, R. J. Joseyphus, Ceramics International, 38 (2012) 2369-2373.

[168] S.M. Masoudpanah, S.M. Mirkazemi, S. Shabani, P.T. Dolat Abadi, Ceramics International, 41 (2015) 9642-9646.

[169] J. Pinkas, V. Reichlova, A. Serafimidisova, Z. Moravec, R. Zboril, D. Jancik, P. Bezdicka, Journal of Physical Chemistry C, 114 (2010) 13557-13564.

[170] R. Skaudzius, T. Juestel, A. Kareiva, Materials Chemistry and Physics, 170 (2016) 229-238.

[171] A. Zarkov, A. Stanulis, T. Salkus, A. Kezionis, V. Jasulaitiene, R. Ramanauskas, S. Tautkus, A. Kareiva, Ceramics International, 42 (2016) 3972-3988.

[172] P.U. Sharma, K.B. Modi, V.K. Lakhani, K.B. Zankat, H.H. Joshi, Ceramics International, 33 (2007) 1543-1546.

[173] L. Sung Ho, C. Kwang Pyo, H. Seok Won, L. Young Bae, Solid State Communications, 83 (1992) 97-100.

[174] M. Lataifeh, A.F. Lehlooh, S. Mahmood, Hyperfine Interactions, 122 (1999) 253-258.

[175] D. Vandormael, F. Grandjean, H. Dimitri, J.L. Gary, Journal of Physics: Condensed Matter, 13 (2001) 1759.

[176] P. Novák, J. Kuneš, W.E. Pickett, W. Ku, F.R. Wagner, Physical Review B, 67 (2003) 140403.

[177] B. Fultz, Characterization of Materials, John Wiley & Sons, Inc., 2002.

[178] P. Novák, V.A. Borodin, V.D. Doroshev, M.M. Savosta, T.N. Tarasenko, Hyperfine Interactions, 59 (1990) 427-430.

[179] M. Brabenec, J. Englich, P. Novak, H. Lütgemeier, Hyperfine Interactions, 34 (1987) 459-461.

[180] Q.I. Mohaidat, M. Lataifeh, S.H. Mahmood, I. Bsoul, M. Awawdeh, Journal of Superconductivity and Novel Magnetism, 30 (2017) 2135-2141.

[181] O. Gamaliy, PhD Thesis, Charles University, Prague, Czech Republic, 2006.

[182] M. Uemura, T. Yamagishi, S. Ebisu, S. Chikazawa, S. Nagata, Philosophical Magazine, 88 (2008) 209-228.

[183] A.L. Tiano, G.C. Papaefthymiou, C.S. Lewis, J. Han, C. Zhang, Q. Li, C. Shi, A.M.M. Abeykoon, S.J.L. Billinge, E. Stach, J. Thomas, K. Guerrero, P. Munayco, J. Munayco, R.B. Scorzelli, P. Burnham, A.J. Viescas, S.S. Wong, Chemistry of Materials, 27 (2015) 3572-3592.

[184] D.T.T. Nguyet, N.P. Duong, T. Satoh, L.N. Anh, T.T. Loan, T.D. Hien, Journal of Science: Advanced Materials and Devices, 1 (2016) 193-199.

[185] M.L. Kahn, Z.J. Zhang, Applied Physics Letters, 78 (2001) 3651-3653.

[186] M.A. Gilleo, Handbook of Ferromagnetic Materials, Elsevier, 1980.

[187] A.E. Paladino, E.A. Maguire, Journal of the American Ceramic Society, 53 (1970) 98-102.

[188] D.M. Lin, M.L. Lin, M.H. Lin, Y.C. Wu, H.S. Wang, Y.J. Chen, Journal of Thermal Analysis and Calorimetry, 58 (1999) 355-362.

[189] J.J. Suñol, A. González, L. Escoda, A. Vilaró, Journal of Thermal Analysis and Calorimetry, 80 (2005) 257-261.

[190] S.C. Parida, S.K. Rakshit, Z. Singh, Journal of Solid State Chemistry, 181 (2008) 101-121.

[191] P. Melnikov, V.A. Nascimento, I.V. Arkhangelsky, L.Z. Zanoni Consolo, Journal of Thermal Analysis and Calorimetry, 111 (2013) 543-548.

[192] M. Misevicius, M. Kilmanas, S. Culunlu, S. Sakirzanovas, A.U. Morkan, A. Beganskiene, A. Kareiva, Journal of Alloys and Compounds, 614 (2014) 44-48.

[193] H. Soleimani, Z. Abbas, N. Yahya, K. Shameli, H. Soleimani, P. Shabanzadeh, International Journal of Molecular Sciences, 13 (2012) 8540-8548.

[194] N. Tangboriboon, A. Jamieson, A. Sirivat, S. Wongkasemjit, Applied Organometallic Chemistry, 22 (2008) 104-113.

[195] P. Vaqueiro, M. Arturo Lopez-Quintela, Journal of Materials Chemistry, 8 (1998) 161-163.

[196] N. Dubnikova, E. Garskaite, A. Beganskiene, A. Kareiva, Optical Materials, 33 (2011) 1179-1184.

[197] H. Lee, Y. Yoon, S. Kim, H.K. Yoo, H. Melikyan, E. Danielyan, A. Babajanyan, T. Ishibashi, B. Friedman, K. Lee, Journal of Crystal Growth, 329 (2011) 27-32.

[198] D. Boyer, G. Bertrand-Chadeyron, R. Mahiou, Optical Materials, 26 (2004) 101-105.

[199] X.-X. Ge, Y.-H. Sun, C. Liu, W.-K. Qi, Journal of Sol-Gel Science and Technology, 52 (2009) 179-187.

[200] K. Nomura, Z. Nemeth, Mössbauer Spectroscopy, John Wiley & Sons, Inc., New Jersey, 2013.